Phase evolution studies in Al-Cu-Fe quasicrystals to tailor the mechanical properties of quasicrystal-polymer composites prepared by spark plasma sintering

Dissertation

zur Erlangung des akademischen Grades

Doctor rerum naturalium (Dr. rer. nat.)

vorgelegt dem Rat der Mathematisch-Naturwissenschaftlichen Fakultät

der Universität Rostock

von

M.Sc. Carmen Gabriela Mihoc

Rostock, November 2014

urn:nbn:de:gbv:28-diss2018-0099-5

Ester Gutachter: Prof. Dr. Eberhard Burkel

Zweiter Gutachter: Prof. Dr. Zhijian James Shen

Tag der Disputation: 6. Mai 2015

Abstract

Quasicrystals (QC) are intermetallic alloys long-range atomic ordered who exhibit intriguing structural characteristics and unusual physical properties contrary to those of their metallic constituents. Since their discovery, many scientists were focused on studying the mechanical alloying (MA) process for preparation of pure quasicrystalline samples suitable for further applications. Main contributions of this thesis are findings on the formation of the QC phase from equilibrium phases through a peritectic reaction directly by MA in order to eliminate the costly process of melting and rapid solidification. Different Al-Cu-Fe alloy compositions are analyzed to determine the ideal stoichiometric composition where φ-phase remains stable and has sharp diffraction peaks down to room temperature. In addition, after finding the most suitable composition stoichiometry in the $Al_{67}Cu_{23}Fe_{10}$ alloy the influence of the milling time on the formation of pure icosahedral (φ) phase is presented. Possible mechanisms which could explain the growth of the single icosahedral phase during milling are discussed. The solid-state transformations are investigated by in-situ high temperature X-ray diffraction (HTXRD) and DSC. The transition temperatures are close to those expected for structural bulk phase transitions. Mechanical properties of sintered pellets by hot pressure (HP), microwave heating (MW) and spark plasma sintering (SPS) are compared.

An important part of the thesis is focused on the preparation and characterization of quasicrystalline-polymer composites for the use in biomedical applications. For this purpose, MA is employed to study the possibility of using this novel technique for the formation of Al-Cu-Fe/polymer composites. The MA method proved to be ideally suited for the production of homogeneously dispersed Al-Cu-Fe particles in the polymer matrix, necessary for tailoring the final mechanical properties of these composites. Further, a series of investigations are dedicated to the synthesis and crystallinity behavior of the composites. The crystallization behavior of the polymer is studied by XRD in combination with DSC to explain the phase transformation and the crystal growth during heating and, therefore, to establish the optimal conditions for the compacting. Whether the interphase between the QC particles and the polymer plays a role in the overall crystallinity is discussed. Finally, the possibility of using SPS technique to process the powders into bulk form suitable for applications testing is investigated.

These field is still in very early stages and it can be noted that the synthesis of quasicrystalline-polymer composites by MA and further SPS processing represent the first of their type. The crystallinity studies on the Al-Cu-Fe/polymer composites constitute preliminary investigations providing information which was, to our knowledge, not reported before.

Content

Chapter 1

Introduction

The discovery of conventionally forbidden crystallographic point symmetries in solids in 1984 was the starting point of intense research focusing on many different aspects of these new materials which were given the name ‘quasicrystals’ [1]. Their intriguing symmetries in connection with long-range order exposed significant limitations of the well accepted rules of crystallography, such that eventually in 1992 the definition of a crystal was changed to a solid possessing an ‘essentially discrete’ diffraction pattern [2] in order to also include quasicrystals.

Quasicrystals of eight- and twelvefold point groups have been observed in metastable alloys only, while five- and tenfold rotationally symmetric quasicrystals have been successfully grown in sufficient size for structural analysis [3–6]. One known example of a fivefold quasicrystal is icosahedral Al-Cu-Fe in different compositional ranges, some of which were investigated in this thesis. Subject to various studies regarding their structural and physical properties, they have yielded many surprising results. These aluminum-rich alloys reveal properties not at all typical for their components, such as an extremely high electrical resistivity decreasing with temperature and rising with the degree of order, brittleness and hardness at low temperatures in contrast to a high ductility at high temperatures, a high corrosion resistance, and a low coefficient of friction [7–10]. The most important question, i.e., whether these properties are related to a complex alloy composition or exclusively to the quasicrystalline structure, has not been resolved, yet.

High quality quasicrystal synthesis has been one of the basic topics in the quasicrystalline investigation for providing samples suitable for the study of the structural and physical

properties of quasicrystals on one hand and for various applications on the other hand. However, there are a number of factors that have retarded a wide application of quasicrystalline materials. In particular, these factors are associated with the problems regarding the preparation of quasicrystalline phases. For the majority of stable systems with thermodynamically stable quasicrystals, the composition region of their formation are very narrow and do not exceed 3 at % in the widest high-temperature region of their existence [11]. On the other hand, metastable quasicrystals can be formed over wider composition regions. However, the rather strict requirements for an accurate chemical composition dictate the requirements for the synthesis technology and possible operation media. In the Al-Cu-Fe system in particular, the high-temperature peritectic transformation complicates the preparation of the quasicrystalline phase. As a consequence of these impediments, it is necessary to use special technologies even in the case of preparation of stable quasicrystals due to the necessity of suppressing zonal segregation. The methods used to produce quasicrystals involve different variants of quenching from the liquid state and mechanical alloying.

The use of mechanical alloying for producing alloys in a non-equilibrium state offers a number of advantages especially important during preparation of quascriystalline materials. Mechanical alloying makes it possible to increase considerably the concentration regions of existence of quasicrystalline phases [12,13] which is particularly important for producing phases with a narrow concentration region of existence. Furthermore, since all reactions during the mechanical alloying occur in the solid phase, the problems arising in the melting technology due to the concentration fluctuations in the liquid phase are not present in this case.

There are a number of publications dealing with the preparation of quasicrystalline phases by mechanical activation [11–22] and they all report a high temperature annealing being needed in order to obtain a single icosahedral phase. In particular, Kaloshkin et al. [11], Eckert et al. [18], Srivinas et al. [19] and Tsai et al. [20] used mechanical alloying to prepare quasicrystals in the Al-Cu-Fe system, in which the icosahedral phase is thermodynamically stable. We chose this system in order to develop the technique for preparing a single-phase quasicrystalline structure by mechanical activation and to investigate the possibility of using quasicrystals as fillers in an ultra-high molecular weight polyethylene (UHMWPE) matrix. Such composites can be used as a material for the preparation of medical implants [23–27].

1.1 Icosahedral Modifications in the Phase Diagram of Al-Cu-Fe System

The methods used for preparation, the region of existence, the structure and the properties of icosahedral quasicrystalline phase (QC) formed in the Al-Cu-Fe system have been intensively studied [28]. The bulk phase diagram of Al-Cu-Fe has been mapped in great detail and a variety of icosahedral modifications has been identified [29]. However, the mechanisms of solid-state reactions involved in this process and the conditions promoting the formation of single-phase QC powders are not clearly described. Some authors explain the formation of the quasicrystalline phase from disordered metastable phases that can be ordered by the effect of heating during the annealing of the milled powder. Other authors state that annealing at high temperatures can lead to liquid formation and the ψ-phase could be formed from equilibrium phases through a peritectic reaction [30]. These aspects of the process are of significant interest, since establishing a direct route for the manufacture of stable quasicrystalline powders by mechanical alloying would replace the costly process of melting and rapid solidification of quasicrystals required for the production of composite materials.

The first stable icosahedral Al-Cu-Fe phase was first reported by Tsai et al. in the compositional range of $Al_{65}Cu_{25}Fe_{10}$ in 1987 [31] leading to a reinvestigation of the Al-Cu-Fe phase diagram. Several authors have determined the ternary phase diagram around this composition [32,33]. The diffraction peaks of the icosahedral (i) phase had however already been found in 1939 by Bradley and Goldschmidt, but was left undetermined as a complex structure denoted ψ [34]. The identification of the i-phase was of great importance since it was the first quasicrystal with an fci lattice and also the first quasicrystal that showed sharp diffraction peaks which unambiguously were associated with a quasicrystalline structure unlike the previously found metastable simple icosahedral quasicrystals [35]. Later it was found that $Al_{62}Cu_{25.5}Fe_{12.5}$ was the ideal composition [32] where the phase remained stable and had sharp unchanged diffraction peaks down to room temperature. The i-phase has been found to be able to form around 450 °C [36] and transforms at 882 °C into a combination of liquid with β-phase (cubic) and/or λ-phase (monoclinic) [37]. The peaks are however relatively broad for annealing at temperatures below 700 °C.

In our attempt to find a stable and pure quasicrystalline phase we followed the same conditions indicated in the literature. But in this mentioned compositional ranges we always obtained a secondary tetragonal phase.

Figure 1. 1 shows the phase diagram proposed by these authors (grey area), as well as the compositional range we investigated with our best samples marked by the red area. Our experiments showed the $Al_{67}Cu_{23}Fe_{10}$ as being the best composition [38], which forms around 360°C, becomes pure at 650° showing sharp diffraction peaks and is stable on a large temperature range (between 650° - 750°C).

Several crystalline and approximant phase designations that are surrounding the i-phase at elevated temperatures are given in Table 1. 1. Other relevant phases and crystallographic data are listed as well in the table.

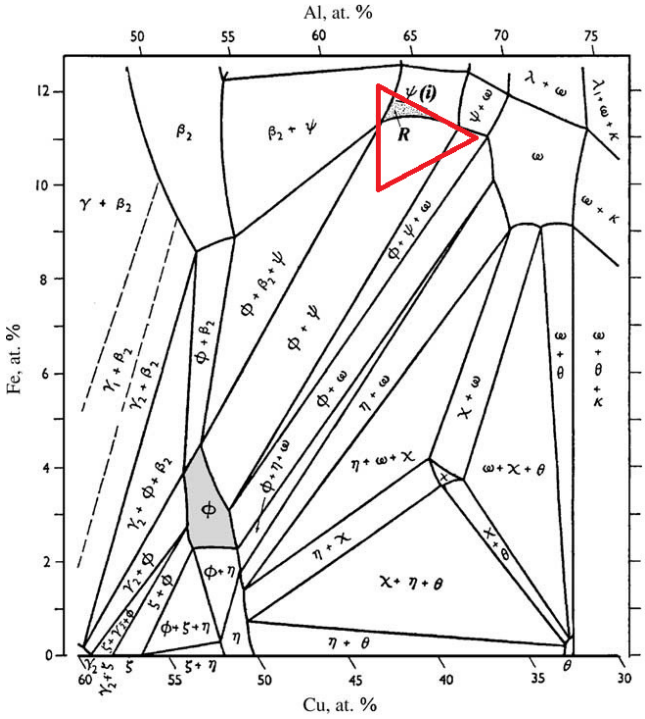

Figure 1. 1 The Al–Cu–Fe equilibrium phase diagram in the vicinity of the ϕ-Al10Cu10Fe phase region (grey area), (after [34,39]). Some of the phase designations and the phase stabilities are listed in Table 1.1. The ψ-phase is the icosahedral i-phase [29], and the rhombohedral R-phase field (dotted region ϕ) is in accordance with Ref. [40]. The compositions investigated in this thesis are located inside the red triangle.

It should be noted that the approximants P1(pentagonal), R (rhomboedric) and O (orthorhombic) form a line of electron/atom ratio e/a ~1.92 in their single phase areas, compared to e/a ~ 1.86 for the i-phase, where the electron valences are 3, 1 and -2 [41] for Al, Cu and Fe, respectively.

On the Al-rich side of ideal i-phase it is possible to obtain all of the i-phase, one of the P1- or the O-phase, and the R-phase from the same sample at different temperatures, independent of which of these states is initially present, since they are all thermodynamically reversible.

Below 680 °C the R-phase is formed and above 715-740 °C imperfect i-phase is formed. P1- and O-phases are formed at temperatures in between. The transitions are rapid to the i-phase, but slow from i-phase to the approximants [40].

Table 1. 1 Overview of the different phases identified in the Al-Cu-Fe system, with their structural characteristics for the regions where the icosahedral phases exists.

Phases	Approximate stoeichiometry (% at.)	Crystallographic system	Cell parameter (Å)	Stability (°C)	References
i-Al-Cu-Fe	$Al_{62}Cu_{25.5}Fe_{12.5}$	Icosahedral	$a_{6d} \approx 6.3346$ Å	< 882	[42,43]
β–Al(Cu-Fe)	$Al_{50}Cu_{50-x}Fe_x$	Cubic	a≈2.9 (for AlFe)		[43]
λ-$Al_{13}Fe_4$	$Al_{76.5}Fe_{23.5}$	Monoclinic	$a = 15.489$ Å $b = 8.0831$ Å $c = 12.476$ Å $\beta = 107.72°$		[43]
ω–Al_7Cu_2Fe	$Al_{70}Cu_{20}Fe_{10}$	Tetragonal	a = 6.336 Å c = 14.78 Å	< 740	[43]
R	$Al_{62.2}Cu_{27}Fe_{10.8}$	Rhomboedric	$a = 32.14$ Å $\alpha = 36°$		[33,40,44]
P1	$Al_{63.6}Cu_{24.5}Fe_{11.9}$	Pentagonal	Periodicity 52.31 Å		[40,45,46]
O	$Al_{60.3}Cu_{30}Fe_{9.7}$	Orthorombic	$a = 32.16$ Å $b = 116.34$ Å $c = 19.85$ Å		[40]

1.2 Quasicrystal – Polymer Composites

A large number of methods for producing polymer composite materials, such as sol-gel reaction [47], intercalative polymerization [48], and melt processing [49] have been developed to date. These composites are dispersed, usually by conventional methods of polymer processing, in the melt [50] for example, by casting [51–54], injection molding [55–57] or extrusion [58–62]. It is however, extremely difficult to disperse the nanoparticles homogeneously in the polymer matrix because of the easy agglomeration of nanoparticles and the high viscosity of the polymer. On the other hand, the production of blends by solution processing often generates environmental concerns regarding solvent removal and disposal. The possibility of blending polymers in the solid state by e.g. mechanical milling (MM) or

mechanical alloying (MA) [63,64] is thus an attractive alternative since many of the problems presently encountered could be avoided altogether [65]. The essence of the method consists in mixing a soft polymer matrix with hard particles of a reinforcing phase on the microscopic structural level in order to ensure a uniform distribution of particles. High energy ball milling (HEBM) [66,67] a low-cost technique for the manufacture of polymer/metal composite powders [68,69], is followed by high-velocity cold compaction [70].

A large number of papers have dealt with the preparation of different composite materials through mechanical alloying [71–77]. Even so, to homogeneously disperse quasicrystalline particles in a polymer matrix can be a challenge.

UHMWPE (-CH2-ln monomer) is an interesting polymer useful in different fields such as medicine, engineering, microelectronics and biology. A special application of this polymer in medicine concerns the interface of mobile joints, such as hip and knee prostheses. The current technology for the acetabular prosthetic cup is dominated by usage of UHMWPE, which is both strong and bioinert. However, after prolonged shear stress from a metallic surface, for example titanium femoral head prosthesis can result in wear debris inducing osteolysis, which is the major cause of premature failure of total joint replacement [78,79].

One recent literature data reports the improvement of the mechanical properties of UHMWPE by adding Al-Cu-Fe quasicrystalline particles [24]. The authors (Bloom et al.) have prepared the Al-Cu-Fe/UHMWPE composites by mixing polyethylene with Al-Cu-Fe quasicrystal powders in a sealed container for 10 minutes. The Al-Cu-Fe quasicrystalline powders consisting of 60% i-phase and 40% β-cubic phase were prepared by gas atomization. The resulting powder mixture was fully compressed under a pressure of 7 MPa at 180°C. The bulk samples were mechanically tested for wear, mechanical strength and cytotoxic response. It was found that the wear on the Al-Cu-Fe/UHMWPE composites is lower than neat UHMWPE and the mechanical strength can be improved by the addition of the Al-Cu-Fe. The composites showed the same cytotoxic response as pure UHMWPE that is routinely used for acetabular cup prosthetics.

It is known that, the mechanical properties of the UHMWPE can be affected by topological variations on the crystal surface and the occurrence of an interphase between the crystalline and amorphous domains. Especially in the samples crystallized from the melt, this interphase plays a significant role [80]. Normally for linear polymers such as polyethylene, it is shown that folded chain crystals are most favorable to form from the melt. Nevertheless, no research was done to ascertain whether this condition will be realized upon crystallization from the

melt when adding Al-Cu-Fe quasicrystalline fillers. The differences in the melting behavior revealed during different heating rates, have consequences on the chain dynamics and indirect on the end properties of the composite. Also, no comparative study was reported if the amount of the quasicrystalline filler can influence the morphology, the overall crystallinity and the nature of the crystalline phases in the polyethylene.

In this work we tried to answer these questions by analyzing the possibility of preparing Al-Cu-Fe/UHMWPE composites by mechanical alloying and spark plasma sintering and studying the influence of the synthesis procedure and the quasicrystalline weight fraction on the crystallinity, polymer chain morphology and mechanical properties.

Dissertation Organization

The fundamental motivation of this work is based on the challenge of finding a direct route for synthesis of high quality Al-Cu-Fe quasicrystals directly during mechanical alloying in order to further use them to produce quasicrystalline/polymer composites for functional biomedical applications. Therefore, in the first part it was particularly important to study the ideal compositional range and the stability region for the single i-phase, but also to optimize the synthesis process. The best composition was chosen and further used on the preparation of quasicrystalline/polymer composites powders. In the second part, a well-controlled synthesis of the composites was established. Mechanical alloying followed by spark plasma sintering was implemented to produce bulk samples. The morphological and mechanical properties of the bulk samples were analyzed and the in-vitro biocompatibility of these composites was studied.

The dissertation is organized into six chapters including this one. Chapter 2 introduces the basic theories about the quasiperiodic structure and the quasicrystalline-polymer composites. In chapter 3 the synthesis methods for the quasicrystalline alloys and their polymer-based composites are introduced. The basic principles of the techniques and analyzing methods used to characterize the morphology, structure and the mechanical properties are described here, as well. The following three chapters include experimental results and discussion. The phase transformation and morphology in various Al-based alloys prepared by ball milling are presented in chapter 4. Chapter 5 describes the most important obtained results in morphology and mechanical properties of quasicrystalline-polymer composites, respectively. The last chapter 6 concludes the dissertation with a summary of the principal results and a brief discussion of the experiments.

Chapter 2

Theoretical background

2.1 Quasicrystals

Solids are classified according to the order and rotational symmetry of their atomic arrangements. Glasses and amorphous solids have disordered arrangements with no exact rotational symmetry. Crystals are constructed by a periodic repetition of a single unit-cell. This periodic long-range order is only compatible with two-, three-, four- and sixfold rotational symmetries. Long range order in crystals without periodicity seemed impossible [81].

In 1984, however, Shechtman discovered a fivefold rotational symmetry in a sharp diffraction pattern from Al-Mn alloys, which meant the discovery of quasicrystals [1]. In order to explain the diffraction pattern, another type of long-range order had to be introduced. In 1992, the International Union of Crystallography finally redefined a crystal as "a solid having an essentially discrete diffraction pattern" [2] and in 2011 Shechtman was awarded with the Nobel Prize for his discovery.

This chapter introduces a general description of the quasiperiodic structure. First, in order to illustrate the existence of long-range order without periodicity, the prominent one-dimensional example of the Fibonacci sequence will be discussed. The Penrose tilling, featuring quasiperiodicity in two and three dimensions, will be subsequently introduced. Both can be derived from a periodic lattice in higher dimensional space as it will be explained. Then the term of crystalline approximants will be introduced and the indexation of the

icosahedral quasicrystals will be explained before presenting structural properties and applications of the Al-Cu-Fe quasicrystals used in the experimental work in this thesis.

2.1.1 Mathematical description of quasiperiodic systems

The aim of this section is to describe the mathematical formalism for the interpretation and analysis of the diffraction data obtained from quasicrystals. Since they do not exhibit any periodicity in at least one dimension, it is not possible to describe them in 3-D space as easily as normal crystal structures. For normal crystals three integer values (Miller indices) can be assigned to label the observable reflections. This is due to the 3-D translational periodicity of the structure. In order to apply integer indices to the diffraction patterns of quasicrystals, however, at least five linearly independent vectors are necessary. Five indices are thus needed for polygonal quasicrystals and six indices for icosahedral quasicrystals. They are called *generalized Miller indices*. The necessary n vectors span an n-dimensional (n-D) reciprocal space. Therefore, there is also an n-D direct space in which a periodic structure can be built and which gives rise to a diffraction pattern as it is observed for quasicrystals.
To explain it simply, in a higher dimensional space a quasiperiodic structure can be described as a periodic one. The actual quasiperiodic structure in the 3-D physical space can then be obtained by the appropriate projection and section techniques. Consequently, it is enough to define a single unit cell of the n-D structure whose contents consist of "hyperatoms" (occupation domains) by analogy with the atoms in a normal unit cell. This enables to describe the whole quasicrystal structure with a finite set of parameters. If it was described in 3-D space only, thousands of atoms would be necessary to obtain a representative volume segment of the whole structure as well as all parameters that go with it (e.g. thousands of positions).

The Fibonacci sequence (Quasiperiodicity in 1-D)

The one-dimensional quasiperiodic structure was proposed first by Fibonacci in 1202 and it´s called the Fibonacci sequence. There are several methods to obtain the Fibonacci sequence, which consists of two types of segments, L (long) and S (short). One recipe is to start with a segment and follow the substitution rule S → L and L → LS to obtain successive strings of increasing length.

generation	section F	Fibonacci number
1	L	1
2	LS	2
3	LSL	3
4	LSLLS	5
5	LSLLSLSL	8
6	LSLLSLSLLSLLS	13

For the Fibonacci sequence, the segment ratio L/S is equal to the golden mean $\tau = 2\cos 36° = (1+\sqrt{5})/2 = 1.618034\ldots$ The limit of the frequency ratio of L and S is also the golden mean τ. This irrational number if often encountered when considering fivefold symmetry, as e.g. in a pentagon the ratio of distances (center to vertex): (center to mid-edge) equals τ/2.

On other important property of the Fibonacci chain is its self-similarity, meaning that by an inflation or deflation, i.e., by a substitution rule of the kind $L \rightarrow F_{n+1}$ and $S \rightarrow F_n$, where n denotes the generation number, another Fibonacci sequence of different length arises.

The one-dimensional quasiperiodic structures are rare. Such phases were discovered and characterized in following systems: A-Cu-Mn, Al-Ni-Si [82] or Al-Pd [83].

Quasiperiodicity Generated from a Higher Dimensional Space

A method to construct a quasicrystalline lattice, and a very important concept in quasicrystallography, is the embedding in higher dimensional space. By the cut- or projection-method, a quasiperiodic structure of n dimensions in a *n*-D space can be created from a periodic structure in *d*-D ($d > n$) dimensional space [84–87]. The method is illustrated in Figure 2.1 for $d = 2$ and $n = 1$ on the left column. The periodic structure in the imaginary 2-D space is cut by the "real" physical space. The nodes appear in the physical space only if the distance is smaller than the inter-atomic distance in the 2-D lattice. This dimension is schematized as a short line at every position of the atoms in Figure 2.1.

The starting point is a regular square lattice of lattice parameter a, where the lattice vectors $\overrightarrow{a_1}$, $\overrightarrow{a_2}$ are rotated by an angle α with respect to the cartesian coordinate axes *x* and *y*, respectively.

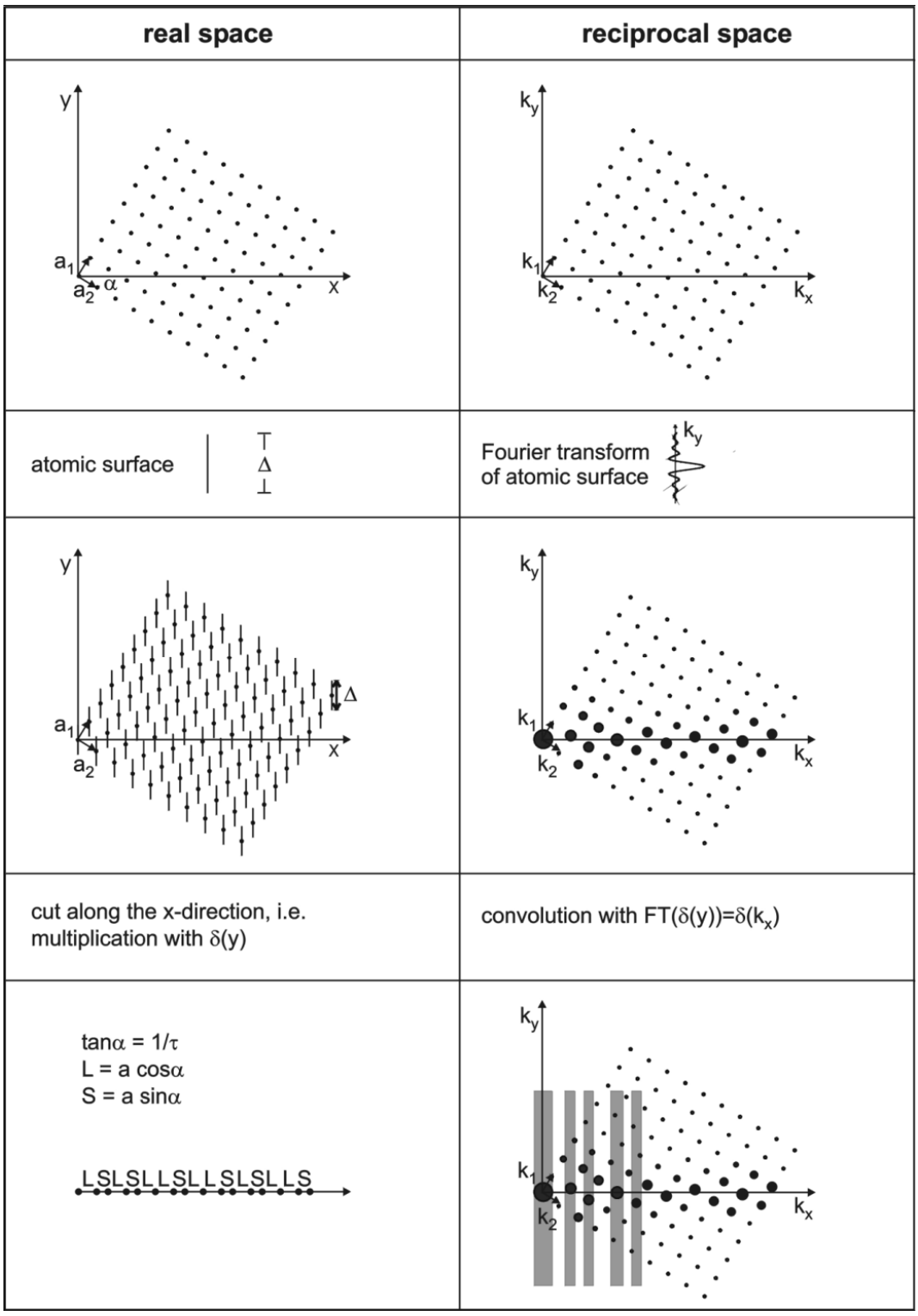

Figure 2.1 Illustration of the higher dimensional concept. The left column describes the cut method to derive a Fibonacci sequence from a periodic square lattice in two dimensions. An equivalent treatment of the lattice in reciprocal space (right column) explains why an aperiodic structure has a sharp discrete and dense diffraction pattern. For clarity, only a few diffraction peaks are indicated by gray bars. Picture taken from [88].

The lattice can then be expressed as:

$$\rho(\vec{r}) = \sum_{n_1,n_2} \delta(\vec{r} - n_1\vec{a}_1 - n_2\vec{a}_2) \quad (2.\ 1)$$

The hypercrystal is now described by decorating the lattice with hyperatoms (atomic surfaces). Decorating the lattice with hyperatoms (HA), in this case a simple one-dimensional line, corresponds to a convolution

$$\rho' = \rho * HA \quad (2.\ 2)$$

With

$$HA(x,y) = \delta(x)f(y), \text{ where } f(y) = \begin{cases} 1, & if \ -\Delta/2 \le y \le \Delta/2 \\ 0, & if \ y < -\frac{\Delta}{2} \ and \ y > \Delta/2 \end{cases} \quad (2.\ 3)$$

and $\Delta = a(\cos\alpha + \sin\alpha)$ the width of the atomic surface. A cut of the decorated lattice along the *x*-axis is mathematically a multiplication with yielding a sequence with two segments, $L = a \cos \alpha$ and $S = a \sin \alpha$. If $\alpha = \arctan 1/\tau$, then $L/S = \tau$, and the sequence is the Fibonacci sequence defined above.

Thus, each position in the sequence can be described by two indices, say h_1h_2, which are the indices of the square lattice. Hence, although the structure is 1-dimensional, two independent indices are needed to characterize the real or reciprocal space positions.

Quasiperiodicity in 2-D

A plane can be fully covered by objects having an axis of rotational symmetry of 2 (rectangles), 3 (equilateral triangles), 4 (squares) or 6 (hexagons). This cannot be done with regular pentagons or polygons that have a number of sides higher than 6. That is why the classical crystallography allows only 2, 3, 4 and 6-fold symmetries.

If a 2-D lattice is constructed using more than one elementary cell, forbidden symmetries can appear as shown first by the British mathematician Roger Penrose in 1974 [89].

The Penrose tiling is an example of a space-filling tiling with tenfold symmetry following the matching rules defined by de Brujin [90].

Like the 1-dimensional Fibonacci sequence, the Penrose tiling is also self-similar. Therefore, by inflation or deflation a Penrose tiling with τ times enlarged or reduced edge length can be obtained by following the transformation rules as indicated in the lower right part of Figure

2.2. Due to these rules a fat rhombus transforms into two fat and one skinny rhombus, while one skinny rhombus is divided into one fat and one skinny rhombus.

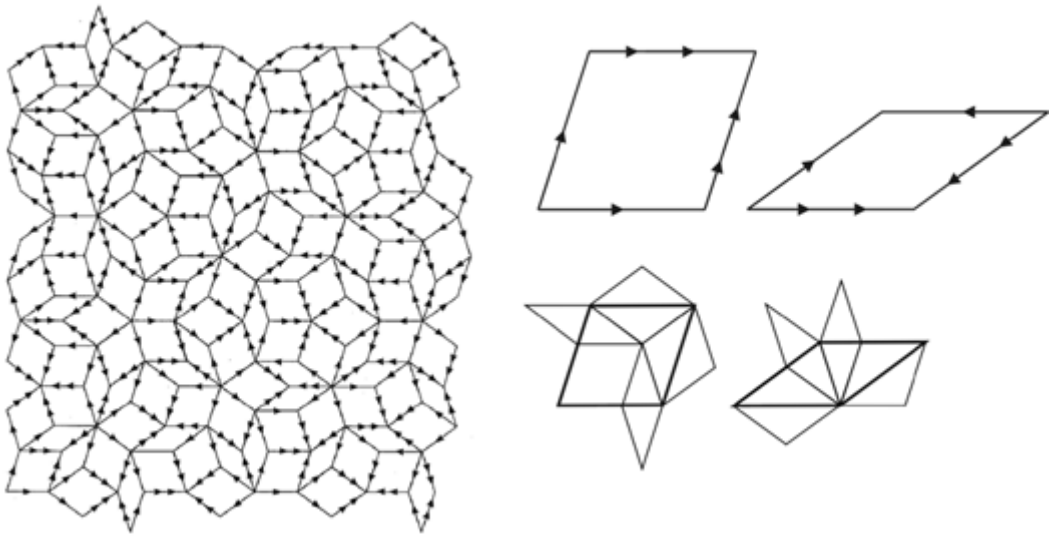

Figure 2.2 A section of the rhombic Penrose tiling obtained from the two tiles, whose edges are labeled by arrows, by following the edge matching rule. The inflation-deflation mechanism is illustrated in the lower right part of the figure (from [84]).

Some examples of 2-D decagonal quasicrystalline systems are: Al_4Fe [91], $Al_{65}Cu_{20}Mn_{15}$ [82], $Al_{64}Cu_{20}Co_{16}$ [92], $Al_{75}Cu_{10}Ni_{15}$ [93].

Quasiperiodicity in 3-D

The icosahedral quasicrystals got their name after the icosahedron, which is one of the five Platon's polyhedrons. It consists of 20 equilateral triangles and it possesses 15 axes of 2-fold symmetry, 10 axes of 3-fold symmetry and 6 axes of 5-fold symmetry, as shown in Figure 2.3. Again, it is not possible to fill completely the 3-D space by using only icosahedrons.

In order to keep the 5-fold symmetry at long distances, it is necessary to use generalized Penrose's trapezoids. The 3-D elementary cells are two rhombohedra [94,95]. The 3-D Penrose tiling formed by these rhombohedra with the matching rules analogical to the 2-D case exhibits a 5-fold symmetry and is sometimes called a “perfect” quasicrystal.

By putting atoms at the vertices of a 3-D Penrose pattern, a Fourier transform can be obtained, which fits very well experimental diffraction patterns of icosahedral quasicrystals.

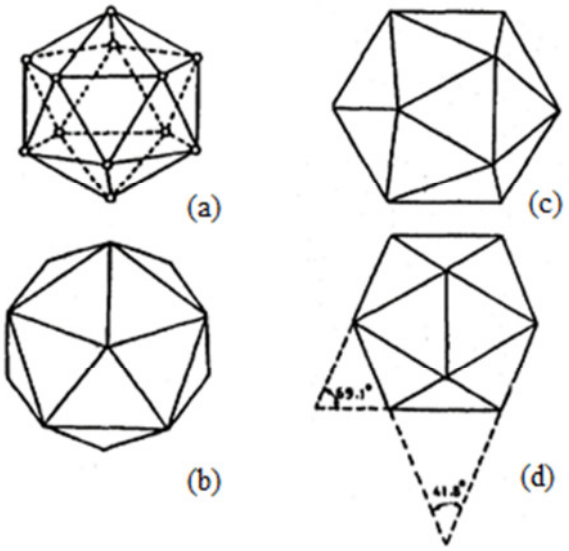

Figure 2.3 The shape of an icosahedron from different projections according to ref [96]. (a) a general view, (b) along the the five-fold axis, (c) along the three-fold axis, (d) along the two-fold axis.

Surely not complete but quite an extensive list of 3-D quasicrystalline phases is provided in Table 2. 1 [97]. In the most cases, the references do not refer to the discovery of the respective quasicrystals but to the papers with the most extensive experimental information.

Table 2. 1 Systems with 3-D icosahedral phases.

QC alloy (composition in at.%)	Reference
$Al_{86}Mn_{14}$	[1]
Al_6CuLi_3	[98]
$Al_{73}Mn_{21}Si_6$	[99]
$Al_{65}Cu_{20}Fe_{15}$	[20]
$Al_{70}Pd_{20}Mn_{10}$	[100]
Ti_2Fe	[101]
Ti_2Mn	[102]
Ti_2Co	[102]
Ti_2Ni	[103]
Nb-Fe	[104]
$V_{41}Ni_{36}Si_{23}$	[105]
$Pd_{58.8}U_{20.6}Si_{20.6}$	[106]

2.1.2 The Structure Factor in Quasiperiodic Systems

The structure factor in periodic lattices is defined as the Fourier transform of the atomic density distribution function $\rho(\vec{r})$ within the unit cell:

$$S(\vec{k}) = \int_{unit\ cell} \rho(\vec{r}) e^{i\vec{k}\vec{r}} d\vec{r} = \sum_{l=1}^{n} \theta_l(\vec{k}) f_l(\vec{k}) e^{i\vec{k}\vec{r}} \quad (2.\ 4)$$

where Θ describes the Debye-Waller term, and $f_l(\vec{k})$ is the atomic form factor of the *l*-th atom in the unit cell.

The structure factor of a quasicrystal's reciprocal lattice is somewhat more complex. Having realized that the intensity of a particular diffraction spot is dependent on its perpendicular space component, the structure factor can be divided into contributions from the conventional atomic scattering factors in parallel space $f_l(\overrightarrow{k_\parallel})$ and from a geometrical form factor $g_l(\overrightarrow{k_\perp})$ in perpendicular space:

$$S(\vec{k}) = \sum_{l=0}^{n} \theta_l(\overrightarrow{k_\parallel}, \overrightarrow{k_\perp}) f_l(\overrightarrow{k_\parallel}) g_l(\overrightarrow{k_\perp}) e^{i\vec{k}\vec{r}} \quad (2.\ 5)$$

Compared to a periodic crystal, the non-unity geometrical form factor resulting from the Fourier transform of the atomic surfaces in perpendicular space leads to an intensity modulation of Bragg peaks not present in conventional crystallography.

2.1.3 Phasons

The additional dimensions of perpendicular space also have an impact on the elastic properties of quasicrystals. While excitations in parallel space correspond to the well-known phonons, an additional degree of freedom arises from excitations in perpendicular space, which are called phasons.

An illustration of this degree of freedom is shown in Figure 2. 4. A displacement of the 2-dimensional lattice and the atomic surfaces by $\vec{u}$ can be separated into a displacement along parallel and perpendicular space, i.e.

$$\vec{u} = \overrightarrow{u_\parallel} + \overrightarrow{u_\perp} \quad (2.\ 6)$$

While periodic crystals also possess a translational degree of freedom in parallel space $\overrightarrow{u_\parallel}$, $\overrightarrow{u_\perp}$ represents an additional degree of freedom in perpendicular space of quasicrystals. A displacement $\overrightarrow{u_\parallel}$ results only in the translation of the Fibonacci sequence as indicated in Figure 2. 4(c). The related elastic excitations are the phonons in conventional crystallography. In contrast, a translation $\overrightarrow{u_\perp}$ along perpendicular space introduces a local rearrangement of atoms, such as *LS* ↔ *SL*, in physical space as indicated by the black letters in Figure 2. 4(d).

These atomic jumps are also called phason flips. The corresponding phason strain leading to the atom jumps is $\frac{d\overrightarrow{u_\perp}}{d\overrightarrow{r_\parallel}}$ in analogy to the elastic strain in conventional crystals $\frac{d\overrightarrow{u_\parallel}}{d\overrightarrow{r_\parallel}}$. Phason flips are regarded as a key mechanism for structural phase transitions [107].

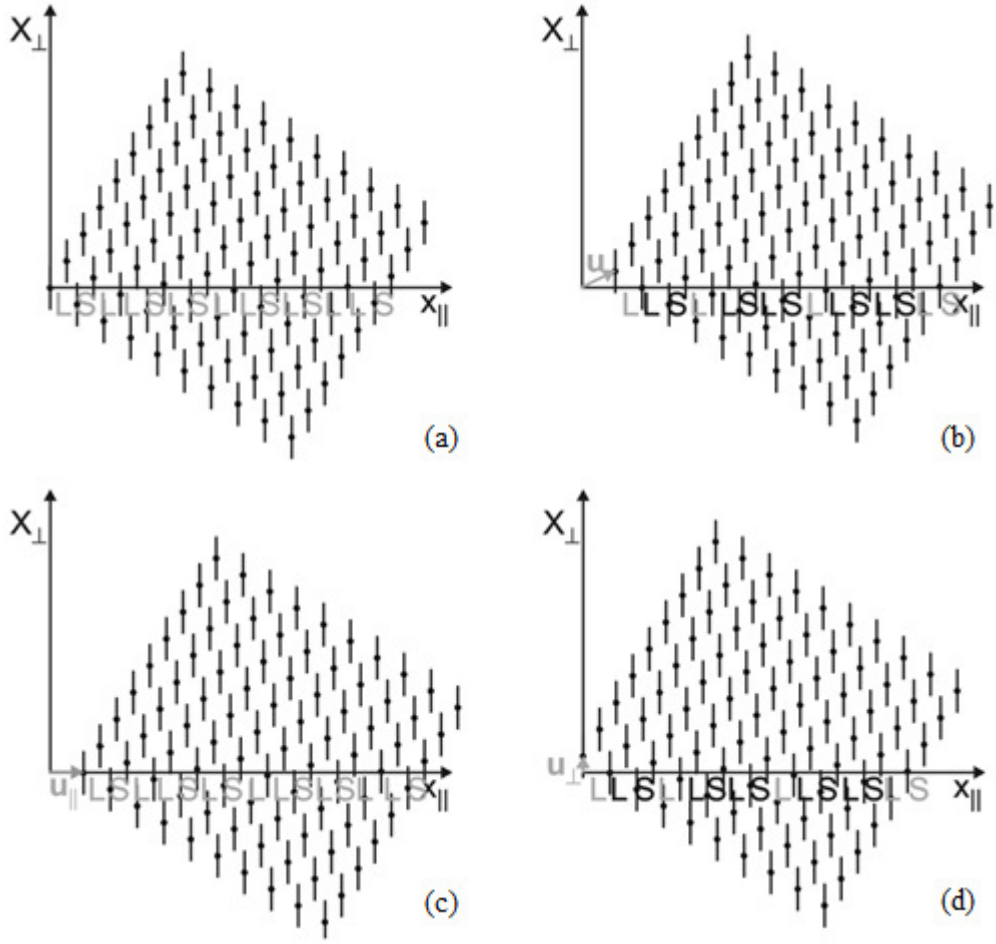

Figure 2. 4 Illustration of phason flips (from [88]). (a) Fibonacci sequence generated from a 2-dimensional periodic lattice. Resulting structure from a displacement (b) $\vec{\boldsymbol{u}}$, (c) $\overrightarrow{\boldsymbol{u}_\parallel}$, and (d) $\overrightarrow{\boldsymbol{u}_\perp}$.

As already indicated in equation 2.5, the intensity of the diffraction spots is not only reduced by the phonon related Debye-Waller factor, but also by a phasonic Debye-Waller term [108]. Recently, single atom jumps were observed experimentally by transmission electron microscopy and their vibrational properties were studied [109]. Phason fluctuations with a non-zero average displacement can lead to peak broadening and a shift of the quasicrystalline diffraction spots [110]. Collective phason flips leading to a deformation of the tiling underlying the quasicrystalline structure have been observed by Edagawa et al. [111].

2.1.4 Approximants

It has been illustrated in the previous section that a non-zero average atomic displacement resulting from a phason strain leads to a change of atom positions. A linear phason strain yields a shearing of the 2-dimensional lattice along perpendicular space as illustrated in Figure 2. 5.

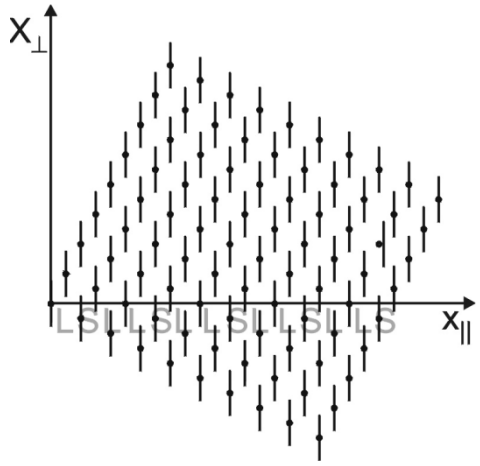

Figure 2. 5. Illustration of an approximant structure with a repetition length of LSL resulting from a linear phason strain (from [88]).

For small shear displacements of the atoms their new positions can be approximated by a tilt of the periodic lattice with respect to physical space. If thereby an angle α with tan α irrational is achieved, a quasiperiodic atomic arrangement results. If the corresponding angle approximates the original one of arctan 1/τ by arctan 1/1, arctan 1/2, arctan 2/3, arctan 3/5 or arctan 5/8 etc. which is the ratio of successive Fibonacci numbers, the atomic structure is called approximant. The repetition length, i.e., the size of the unit cell depends on the angle. For example, an angle of arctan 1/2 leads to the structure in Figure 2. 5 with a repetition length of LSL. This approximant is called 2/1 approximant. The higher the order of the approximant, the more similar its atomic structure is to that of the quasicrystal. Approximants are useful for modeling the atomic structure of quasicrystals in order to determine physical properties, such as the electronic structure [112–115].

2.1.5 Indexing of Icosahedral Quasicrystals

The first quasicrystal found in the Al-Mn system showed icosahedral symmetry, which needs six unit vectors to index the diffraction patterns.

The diffraction pattern of an ideal three-dimensional quasicrystal consists of Bragg peaks located on a lattice given by

$$\vec{Q} = \sum_{i=1}^{6} n_i \overrightarrow{b_i} \quad (2.\ 7)$$

where the $\overrightarrow{b_i}$ are the basis vectors pointing to the vertices along the six fivefold symmetry axes of a regular icosahedron in three dimensions and the n_i are integers that index each vector. The quasicrystal formula is similar to that for a crystal except that the number of basis vectors is greater than the number of dimensions (three), a consequence of the noncrystallographic symmetry.

This work will follow the method proposed by Cahn [42] which uses a system of cubic coordinates in the physical space. In the icosahedral group there exist mutually perpendicular axes of 2-fold symmetry and the three cubic coordinates are chosen parallel to these axes. One disadvantage of this description is the irrationality of Miller indices. The 5-fold symmetry axes have Miller indices of the <1, τ, 0> type. Moreover, some axes can have both rational and irrational indices: four 3-fold symmetry axes are labeled as <1, 1, 1>, while other 6 axes of this type are referred to as $<\tau^2, 1, 0>$. Therefore, another notation with 6 indices was introduced. The irrational numbers are always in the form $n + n'\tau$, n and n' being integer numbers. Every vector $\vec{Q}$ in the reciprocal 3-D space is described by three couples of indices:

$$\vec{Q} = (h + h'\tau, k + k'\tau, l + l'\tau) = (h/h', k/k', l/l') \quad (2.\ 8)$$

The inter-planar distance d for the icosahedral Miller indices [42] $(h/h', k/k', l/l')$ is given by

$$d(h/h', k/k', l/l') = \frac{d_0}{\sqrt{N + \tau M}} \quad (2.\ 9)$$

where d_0 is the 3-D quasilattice constant, which for the icosahedral Al-Cu-Fe equals to d_0 = (17.00 ± 0.02) Å [116], N and M are so-called "principal indices" used to index the Bragg´s peaks which are related to Miller indices $(h/h', k/k', l/l')$ by the equations:

$$N = h^2 + k^2 + l^2 + h'^2 + k'^2 + l'^2 \quad (2.\ 10)$$

$$M = h'^2 + k'^2 + l'^2 + 2(hh' + kk' + ll') \quad (2.\ 11)$$

2.1.6 Properties and applications of quasicrystals

While a large amount of theoretical and experimental research has been dedicated to the atomic structure of quasicrystals, few studies related to their physical or mechanical properties have been reported [117,118].

Quasicrystals exhibit extraordinary properties compared to common metals. Some of these properties (high hardness, low electronic and thermal conductivity – quasicrystals behave as insulators at very low temperature when their structure is perfect – low surface energy, low fracture toughness, low friction coefficient, good oxidation and corrosion resistance, unusual optical properties) could be useful in technological applications.

As far as the applications are concerned, quasicrystals suffer from a serious drawback: they are brittle materials up to a brittle-to-ductile transition temperature.

The mechanical properties of icosahedral Al-Cu-Fe have been studied in detail [118,119]. These quasicrystals are brittle at room temperature and they fracture before reaching the yield point by propagation of cracks or micro-cracks. A brittle-to-ductile transition was observed via compression testing between 700K and 750K (see Fig. 2.6). Above the transition temperature, quasicrystals become plastic and lose their hardness. Giacometti also evidenced that the plasticity at high temperature is controlled by a thermally activated mechanism of dislocation motion.

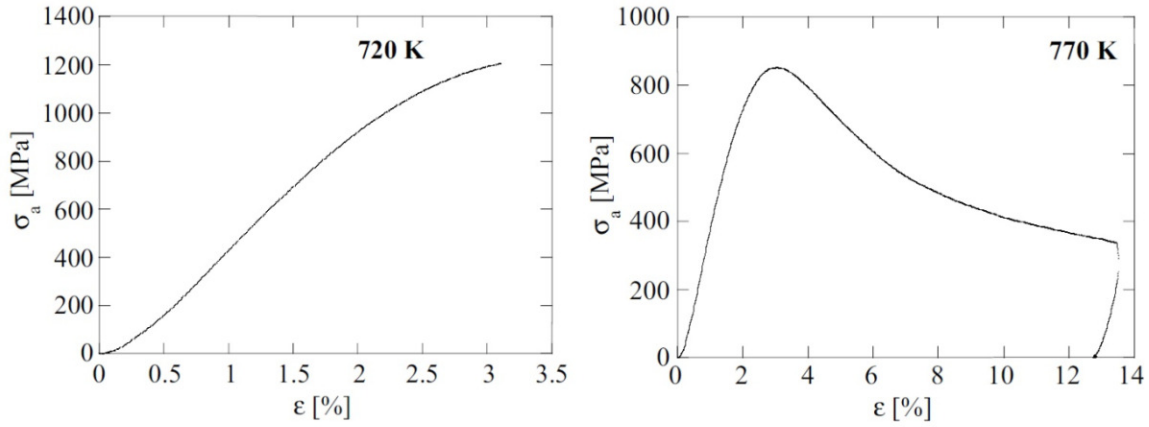

Figure 2. 6 Compression stress-strain curves of icosahedral Al-Cu-Fe, brittle deformation at 720K and ductile deformation with work hardening and yield point followed by strain softening at 770K [118].

The mobility of dislocations is supposed to be inherently limited by the particular quasiperiodic structure [120,121]. The first dislocations which pass within a slip plane have difficulties to move due to the formation of a high energy phasonic displacement field behind them. The further dislocations are moving in planes already faulted exhibiting a lower

resistance to their movement. The size of the disordered region extends by diffusion at high temperatures (see Figure 2. 7). This explains the brittle behavior at low temperatures and the ductile behavior at high temperatures.

The stress strain curves exhibit an elastic stage, a work hardening stage, an upper yield point and then a softening stage (see Figure 2. 6). The upper yield point is therefore associated with low dislocation mobility and not with a low mobile dislocation density, as for example in semiconductors. The dislocation mobility is limited by the presence of localized obstacles, intrinsic to the quasicrystalline structure. Both the density of the obstacles and the energetic barrier decrease with the increasing number of dislocations which have already overcome the barrier.

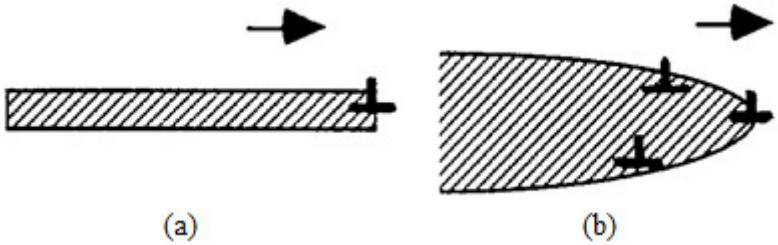

Figure 2. 7 Disordered region promoting further slip activity in the wake of a leading dislocation: (a) localized disorder at low temperatures; (b) diffusion induced extended disorder at high temperatures [121].

The intrinsic low-temperature brittleness of quasicrystals has confined the field of their potential applications to three main areas:

- bulk materials for hydrogen storage [122,123]
- thin or thick films for thermal-barrier or oxidation protection surface coatings [124,125]
- micro- or nano-sized particles for composites reinforcement [126–128]

2.2 Quasicrystal-Polymer Nanocomposites

Quasicrystalline-polymer composites are composite materials which consist on quasicrystalline particles three dimensionally distributed in a polymer matrix. Whether these materials are biphasic without or with weak chemical bonds between the two components is not clear, yet.

Polymers are macromolecules in form of long, flexible chains in which often a string of carbon atoms constitutes the backbone. Within each unit, the atoms are bound together by covalent bonds. UHMWPE in particular has a linear molecular structure, where the chains are long, flexible and may be considered as a mass of spaghetti, as pictured in Figure 2. 9.

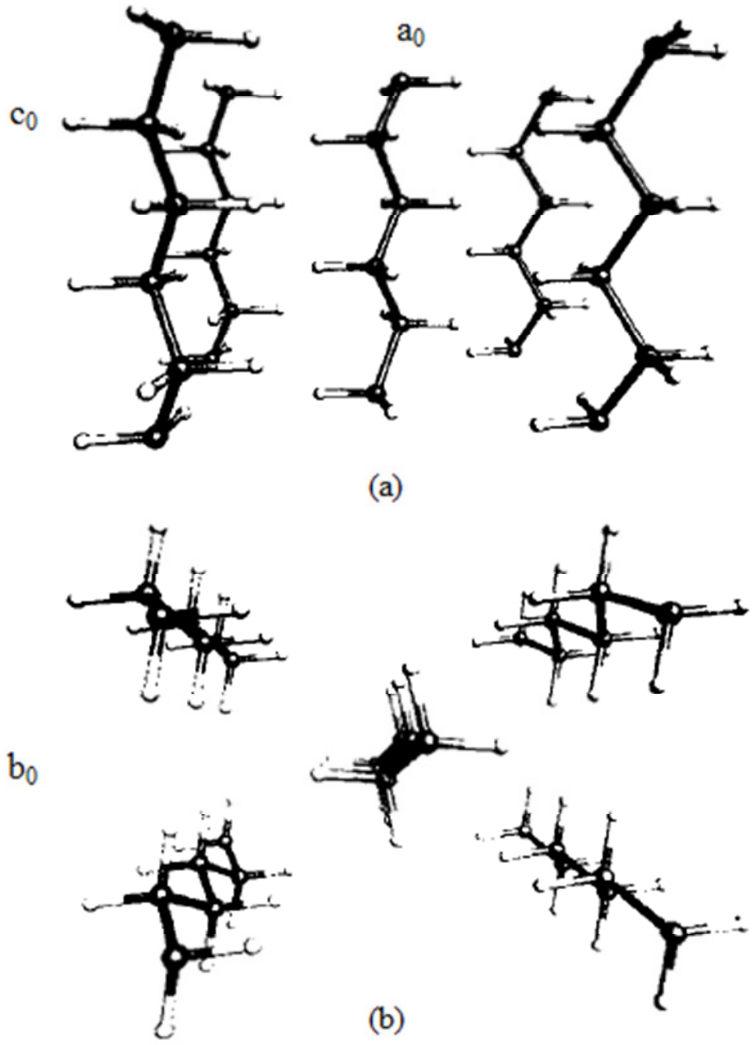

Figure 2. 8 Views of the orthorhombic structure of polyethylene along: (a) b-axis (b) c-axis (the axis of the polymer chain. The larger black circles represent C and the smaller empty circles represent H. (Picture taken from [129])

Polyethylene crystallizes in the orthorhombic structure shown in Figure 2. 8, which is also defines the axes used in the present work. Polyethylene was the first organic polymer for which band structures were reported and the crystallization process was intensively studied [129–131]. Prepared under certain conditions, polyethylene can have monoclinic or hexagonal crystalline form.

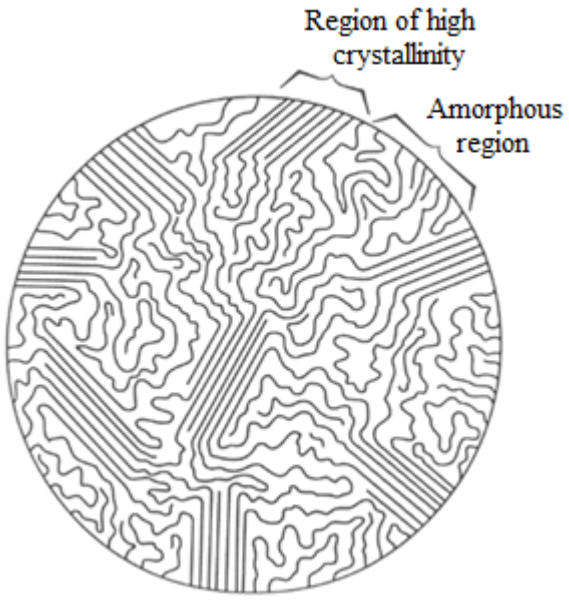

Figure 2. 9 Schematic diagram showing the typical morphology of semicrystalline polymers. The crystallites are formed by aligned chain segments of much larger molecules, with other segments in the disordered matrix. (Diagram from Hayden and Moffatt 1965 [132])

Melt compounding is the most commonly used approach for generating polymer nanocomposites. Here, high-molecular-weight polymer powders such as polyethylene (UHMWPE) can be melted at 180°C, after which the inorganic powder is added to the melt. The filler is then kneaded and compounded thoroughly with the polymer melt in order to achieve a uniform dispersion and distribution of the filler. Although the melt compounding approach requires the use of a high temperature, this can sometimes cause concern with regards to surface modifications [133]. Rastogi [80] discussed the morphological aspects of the so-called `interphase` that exists between the ordered three-dimensional crystalline phase and the randomly structured amorphous phase. He showed that the structure of the interphase strongly depends on the crystallization conditions which influence the amount entanglements present between the crystals. The differences in the melting behavior of the UHMWPE, revealed during different heating rates, are due to differences in the chain dynamics. This causes topological variations on the crystal surface, thus affecting the mechanical properties.
The main advantage of adding inorganic fillers into a polymer is the possibility of providing controlled properties by varying the composition, ratio between components and microstructure of composites. It was already reported that quasicrystalline particles may significantly improve wear resistance in polymer-based composites [24–26]. However, no

study was reported on the influence of the quasicrystalline filler on the crystallization behavior of the UHMWPE.

Chapter 3

Experimental techniques

The experimental procedures and the parameters applied for the preparation of the samples are briefly described in this section. Afterwards the fundamentals of the characterization techniques for structural, physical and mechanical properties of the samples are introduced. In the end the data analysis procedures are presented. First in vitro bio tests performed on the composites are also shortly described.

3.1 Sample Preparation

3.1.1 Powder Metallurgy Synthesis

The mechanical alloying (MA) is a non-equilibrium solid state powder approach which relies on deformation process to mix materials. This technique was used in this work for the intermetallic synthesis of Al-Cu-Fe alloys and nanostructured polymer-quasicrystalline composites.

The extreme deformation experienced by milled material is an intrinsic part of the MA process. Different alloy systems react to milling in different ways depending on the mutual solubility and reactivity of the components, their mechanical properties and the type of milling equipment used. Despite these differences Benjamin and Violin [134,135] identify five progressive stages of alloying:

1. Particle flattering – the particles are flattered becoming flake-like.
2. Welding predominance – the flattened particles weld to form lamellar or layered composite particles.

3. Equiaxed particle formation – the lamellar particles are no longer flake like, becoming thicker and rounded. The shape change is caused by the work hardening of the powders.
4. Random welding orientation – fragments from the equiaxed particles start to weld in different orientations and the lamellar structure starts degrading.
5. Steady state processing – the structure of the material is gradually refined as fragments are taken from the particle that later weld with other fragments in different orientations.

In the present work, nanocrystalline powders were synthesized using a RETSCH PM400 planetary ball mill. Planetary mills use a centrifuge to boost their milling intensity (Figure 3. 1) [135,136]. They frequently have more than one chamber as shown in Figure 3. 1, which are arranged on a large rotating support disk, forcing the milling media away from the centre of the disc to the outer-most part of the chamber wall. The chambers rotate in the opposite sense to the disc, causing the milling media to cascade with a great intensity (Figure 3. 1b).

This type of mill is ideally suited to laboratory use as it has a sample sized capacity and can process several samples at once. It offers a range of milling intensities obtained by varying the speed at which the components rotate.

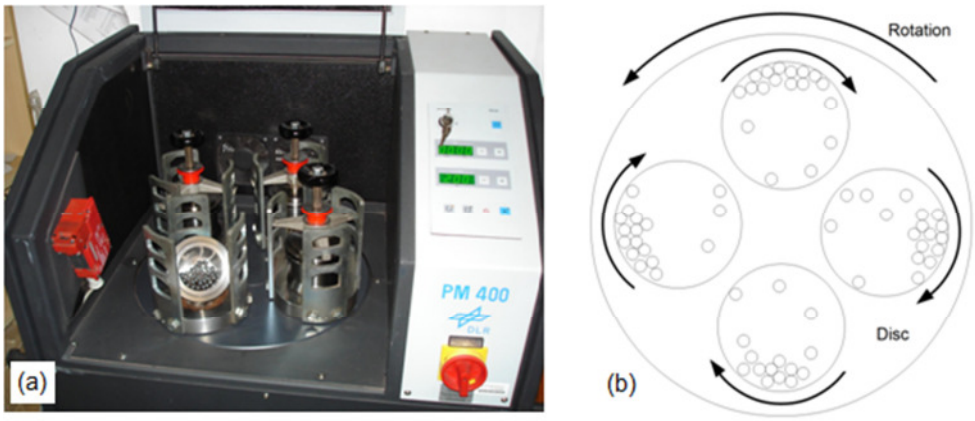

Figure 3. 1 (a) RETSCH PM400 planetary four station ball mill. (b) Schematic planetary mill (top view) [135].

3.1.2 Heating and Compacting Methods

Spark plasma sintering (SPS) and microwave heating are innovative techniques which produce heat inside the material and thus allow volumetric heating for a variety of different materials. This differs from conventional methods where heat is transferred between objects through the mechanisms of conduction, radiation and convection. Furthermore the high heating and cooling rates during SPS and microwave processing can also enable phase transformations of very fast kinetics in e.g. ceramics or metallic alloy systems [137,138].

3.1.2.1 Spark Plasma Sintering Process

Sintering is a process where thermal energy is used for obtaining products with controlled density. The driving force for sintering is the reduction of total interfacial energy. The reduction can be written:

$$\Delta(\gamma A) = \Delta\gamma A + \gamma\Delta A \quad (3.1)$$

where γ is the interfacial energy which is reduced by densification, and A is the total interfacial area which is reduced by grain coarsening.

Spark plasma sintering method (SPS), also named field-activated sintering (FAST) is a new generation of sintering which allows compaction of ceramic and metal powders at low temperature and in short time (within minutes). Common to these systems is the use of pulsed direct current to heat the specimens. Whether plasma is generated has not been confirmed yet, especially when non-conduction ceramic powders are compacted. It has, however, been experimentally verified that densification is enhanced by the use of a pulsed direct-current (DC) or field [139].

The basic configuration of a SPS unit is shown in Figure 3. 2. It consists of a uniaxial pressure device, where the water-cooled punches also serve as electrodes, a water-cooled reaction chamber that can be evacuated, a pulsed DC generator, pressure-, position- and temperature-regulating systems. It is supposed that the pulsed current propagates through the powder particles inside the SPS sintering die, as shown in Figure 3. 3a. The process inventor also claims that the ON- OFF DC pulse energizing method generates: 1) Spark plasma; 2) Spark impact pressure; 3) Joule heating; and 4) An electrical field promoting material transfer and diffusion [140]. Figure 3. 3b illustrates the used ON–OFF pulsed direct current during the entire sintering cycle, with a standard on–off time relation of 12:2.

A unique feature of the SPS process is that it uses very fast heating rates (up to 600°C/min); thus the consolidation rate is greatly enhanced (fully dense materials are obtained within minutes) and the sintering temperature can be a few hundred degrees lower than that typically used in conventional sintering processes [141].

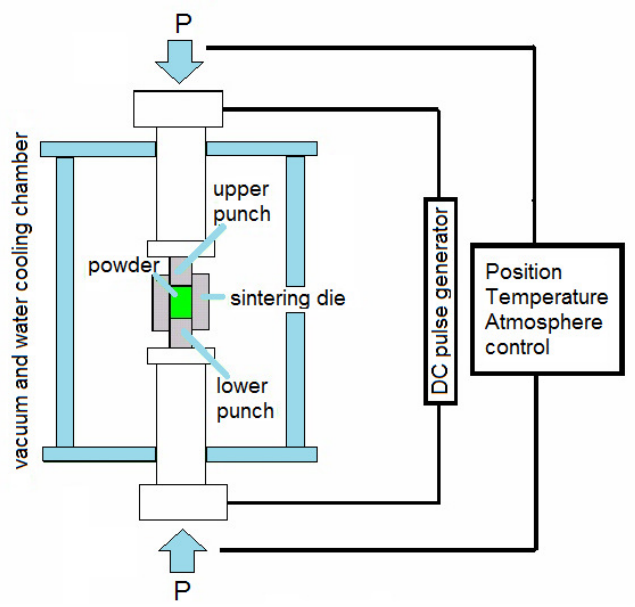

Figure 3. 2 Schematic configuration of a typical SPS system.

Four factors that contribute to the enhanced densification process can be discerned:

1. The use of rapid heating and cooling rates;
2. Rapid transfer of heat because the die itself acts as a heating element;
3. The application of a mechanical pressure exceeding that used in the conventional hot-pressing process;
4. The use of a pulsed DC current to heat the sample, implying that samples are also exposed to a pulsed electric field during sintering. It is generally accepted that application of mechanical pressure promotes the removal of pores and enhances diffusion. However, it is frequently argued that the improved densification rates stem mostly from the use of direct current pulses of high energy.

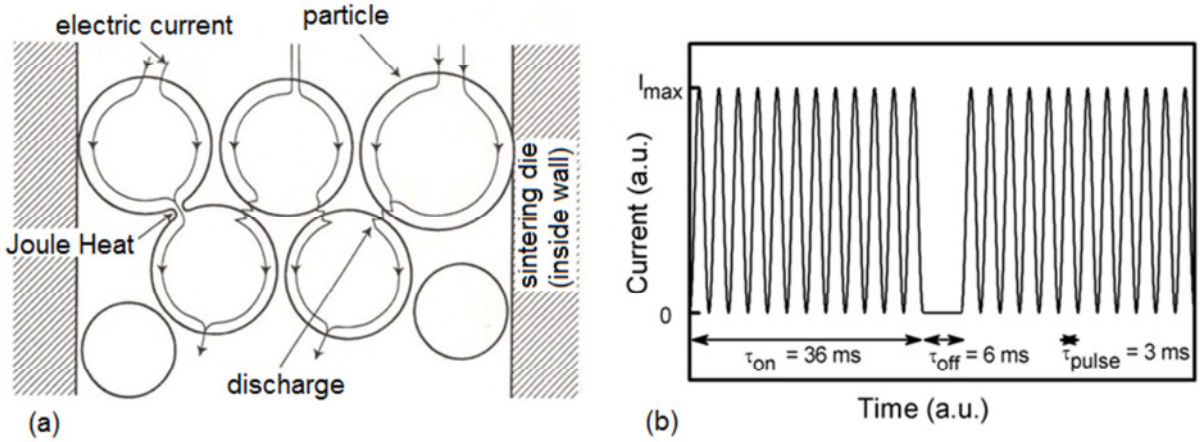

Figure 3. 3 (a) A schematic drawing of the pulsed current that flows through powder particles. (b) The pulsed DC current sequence of 12:2 used in this work for the SPS process.

Further advantages of SPS include ease of operation, accurate digital control of sintering profile as well as good reproducibility and reliability.

In this work, Al-Cu-Fe powder alloys were sintered using a SPS machine with pulsed DC voltage. The nanopowders were loaded into graphite die-punch units to sinter disc-shaped pellets of about 20 mm diameter. The samples were fast heated with 20°C/min to 780°C followed by a dwell-time of 10 min at the sintering temperature and rapidly cooled down. The SPS experiments were conducted in vacuum, under an applied uniaxial pressure of 55MPa.

Sintering of composites was performed in vacuum, under a uniaxial pressure of 7MPa. A pulsed DC voltage was used. Any degradation of the surface modification may have serious impact on the composite properties, so the temperature was at first raised to 170 °C at a fast heating rate of 40 °C/min followed by a short dwell-time of 60 s at this sintering temperature in order to avoid any degradation.

3.1.2.2 Microwave Processing

Microwave radiation is electromagnetic radiation in the frequency range of 300MHz to 300GHz, which correspond to a wavelength range of 1m to 1 mm. The general goal of microwave processing is the generation of heat inside a sample. Because the material itself generates the heat, heating is more volumetric and can be very rapid and selective [142]. Thus, microwave sintering techniques allows for the application of high heating rates, markedly shortening the processing time.

Heating processes are generally described by their temperature profile and their characteristic heating time:

$$\tau_T \sim T/\left(\frac{\partial T}{\partial t}\right) \qquad (3.\ 2)$$

Here τ_T can be considered as a measure how fast heat is deposited inside the sample. Bykov et al. [143] gives an excellent review about thermophysical properties of microwave processing. Recent publications also demonstrated the ability of microwave processing to generate the quasicrystalline icosahedral phase in Al-Cu-Fe allyos [144,145].

For microwave experiments the AlCuFe and QC/UHMWPE composite powders were cold-pressed into 30 mg pellets with a diameter of 5 mm in a uni-axial press under approximately 1 GPa. The samples were placed in a quartz glass tube in the magnetic field anti-node of a single-mode resonator (TE_{102}) made of a WR340 rectangular waveguide at a frequency of

2.45 GHz. Microwave powers were measured with uncalibrated DD112 directional couplers (S-TEAM, Bratislava, Slovakia). The samples temperature was monitored with an IGA 5 infrared pyrometer (IMPAC, Frankfurt am Main, Germany) which was calibrated using a K-type thermocouple (Figure 3. 4).

The pellets were heated up to different maximum temperatures in the microwave resonator with similar heating rates and constant input power, in order to reproduce the temperature sequence of the in-situ X-ray diffraction experiments. The subsequent fast cooling was achieved only by thermal losses of the samples.

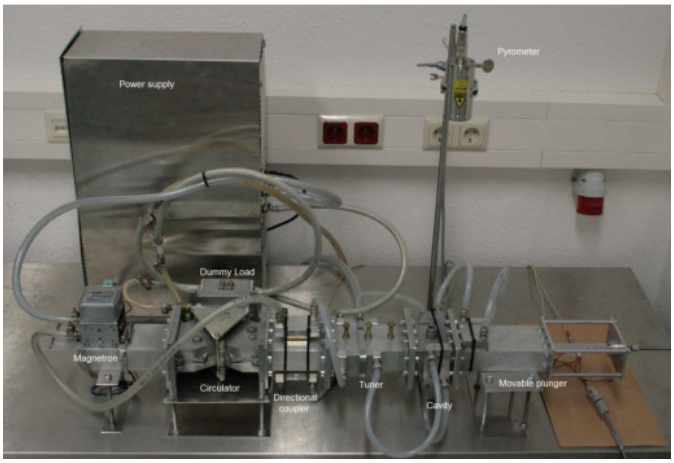

Figure 3. 4 Picture of the microwave applicator. The magnetron is connected to the power supply and is isolated by the circulator and dummy load. Afterwards the incoming and reflected microwave power is measured with microwave diodes at the directional coupler. The tuner can be used to match the load impedance. Samples are processed in the resonant cavity which contains a movable plunger. The temperature signal of the pyrometer and the diode signals are collected by a data acquisition board Picture taken from [146].

The density was measured by Archimedes' principle using water as a medium. Prior the measurements, all the samples were cleaned by mechanical grinding from the graphite paper used in the sintering.

3.2 Surface composition characterization

The surface characterization uses electrons. By the diffraction of electrons on the surface of the sample, information can be gained regarding the surface morphology, structure and composition.

3.1.1 Scanning Electron Microscopy and Energy Dispersive Spectroscopy SEM/EDX

Electron microscopes work exactly as their optical counterparts except that they use a focused beam of electrons instead of light to "image" the specimen and gain information as to its structure and composition. A stream of electrons is formed by an electron source and accelerated toward the specimen using a positive electrical potential. This stream is confined and focused using metal apertures and magnetic lenses into a thin, focused, monochromatic beam which is scanned over the sample. The interactions occurring between the beam and the surface of the sample are detected. A secondary electron (SE) detector was used to image the topography of the surface and the backscattered (BSE) electron detector to evidence the element contrast. Energy dispersive X-ray (EDX) analysis was used to identify and quantify the chemical composition of the samples. The incident electrons cause excitations in the sample atoms, which relax by emitting X-rays specific for the atoms. Qualitative analysis is then done by identification and comparison between the received spectra and characteristic spectra of each element. For quantitative analysis, the measured intensities are recalculated into weight percentage for all elements detected in the sample.

The quasicrystalline samples investigated in this thesis are conductive but the composites are semiconductive. The semiconductive samples were imaged and EDX analyzed in low vacuum mode, at 50 Pa. The electron microscopy examination was performed at IBMT (Institut für Biomedizinische Technik) in Warnemünde. The SEM images were acquired using a Philips XL30-FEI and a Quanta FEG250 SEM microscope operating from 500 V to 30 kV, spot size of a few nanometers and a working distance of 10 mm.

3.3 Structural Characterization

The structural characterization includes the characterization of the crystal structure, the lattice parameter, the composition of the samples and the phase evolution respective grain growth during heating. X-ray diffraction is one of the basic tools of materials science, as it allows determining the grain size, to distinguish between different phases and different orientations in the samples and it is non-destructive.

The structure of the samples has been checked with X-ray diffractometry (XRD) equipment situated at the Physics Institute, in the department of New Materials. Synchrotron radiation (at HASYLAB/DESY, beamline B2, BW5 and F2.1) was additionally used to analyze subtle structural details and to follow structure evolutions as a function of temperature even in small steps on the other. The high-quality diffraction data was used for the interpretation of microstructures, based on analyzes of the half-widths and shapes of the reflection profiles. The technical details of the equipment as well as the analysis procedures used in this work are described in this subchapter.

3.3.1 X-ray Diffraction Analysis

The equipment used for the XRD measurements is a D8 Bruker AXS with a General Area Diffraction System (GADDS). Its X-ray source consists of a copper anode ($K_{\alpha 1}$=1.54056 Å and $K_{\alpha 2}$=1.54439 Å) and a Göbel-mirror system. This setup delivers a well monochromatized and parallelized X-ray beam of the CuK_{α}, wavelength $\lambda_{K\alpha}$ = 1.54178 Å [147]. The working conditions for the diffractometer were 40 kV and 40 mA. The 2-dimensional HI-STAR detector offers the fast and precise measurement of the diffraction patterns. The scanning was performed in the range of $10° < 2\theta < 85°$ with an angular resolution of 0.04° and an integration time of approximately 0.45 s per step.

The intensity of a Bragg peak is influenced by several parameters, namely the volume fraction of the constituent phases, the symmetry of their atomic structures, the scattering factor *F*, the Debye-Waller temperature factor, preferred orientation (texture) effects, as well as the scattering geometry employed (absorption effects, the Lorentz-polarization (*LP*) factor) and the X-ray wavelength λ (anomalous scattering).

3.3.2 High Energy Powder Diffraction using Synchrotron Radiation

High energies have the advantage that they scatter mainly into the forward direction. The scattering angle 2θ is related through Bragg's law to the momentum transfer *Q* by

$$\sin\theta = Q/2k \qquad (3.3)$$

where k represents the wave vector, $k = 2\pi/\lambda$, which typically lies in the range of 60 $Å^{-1}$. *Q* being equal to a reciprocal lattice vector *G* of up to 10 $Å^{-1}$, 2θ may reach up to 10°. A second advantage is the relatively flat Ewald sphere as demonstrated in Figure 3. 5. Since the energies

are about 10 times higher than for conventional X-rays, the curvature of the Ewald sphere is about 10 times smaller. Low-energy Ewald spheres strongly bend away from a plane in reciprocal space, a crystallographic zone, and only a few reciprocal lattice points in some arbitrary directions may lie on or in the vicinity of the sphere. For high energies, the sphere smoothly takes off the zone, having reciprocal lattice points from several Brillouin zones in their vicinity.

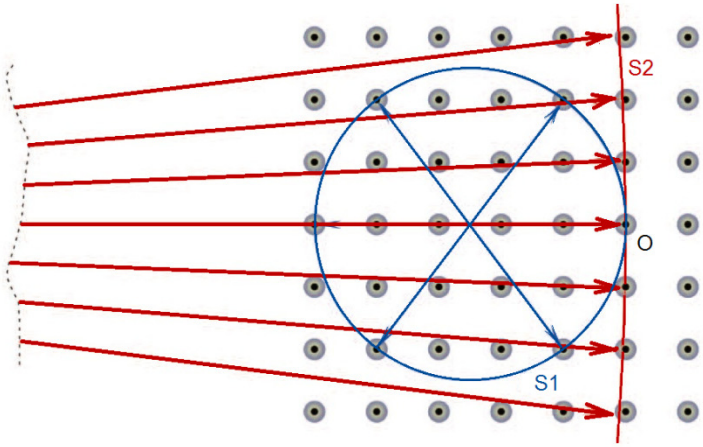

Figure 3. 5 Ewald-spheres S1 and S2 for low- and high-energy X-rays, respectively, which differ typically by one order of magnitude in their radius. S1 is strongly curved and only a few reciprocal lattice points may lie in or near to it, the reflected wave vectors going into arbitrary directions. The curvature of S2 is much smaller and the sphere takes off smoothly a plane in reciprocal space. Diffraction goes mainly into the forward direction and diffuse halos around the Bragg peaks can be mapped in a single shot over several Brillouin zones. Illustration adapted from [148].

High-energy synchrotron X-ray diffraction was performed at BW5 beamline (HASYLAB/DESY). BW5 is dedicated to X-ray scattering experiments at energies between 60 and 150 keV. The large penetration depth at these energies of typically several mm to cm allows the investigation of bulk materials and complex sample environments. The experimental station is equipped with a triple axis diffractometer and a MAR345 image plate camera. The beamline optics consists of a 2 mm Cu window removing all heat loads from the crystals. A triple-axis diffractometer is setup in the experimental hutch.

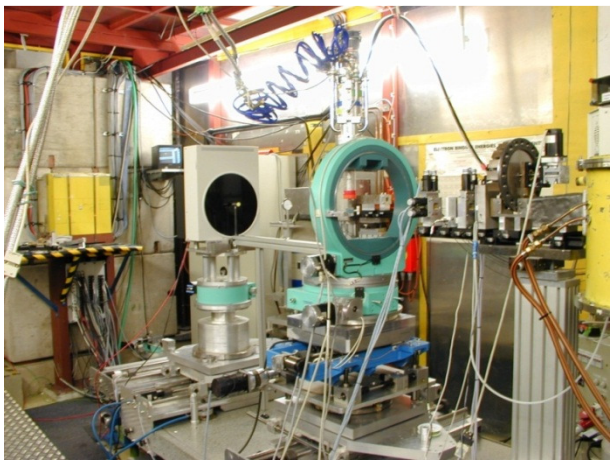

Figure 3. 6 View of the BW5 triple-axis diffractometer. 1: Huber circle 480 carrying the single counter. 2: analyser crystal and attenuator. 3: MAR345 image-plate detector.

A detailed description of the beamline and its key components is given in reference [149].

3.3.3 High-resolution Powder Diffraction using Synchrotron Radiation

X-ray diffraction experiments were performed using the high-resolution diffractometer (B2) at the synchrotron radiation laboratory HASYLAB/DESY in Hamburg, Germany. At this beamline, synchrotron radiation is delivered by a bending magnet insertion device situated at approximately 35 meters away from the location of the sample.

The diffractometer comprises two Huber parts situated on opposite sides of the synchrotron radiation beam. The Huber parts may separately be displaced horizontally along the normal to the synchrotron radiation beam and define a vertical scattering plane. While one of the Huber parts is a two-circle part able to carry both the sample and the detector holders, the second Huber part can be used for mounting additional equipment. The main advantage of the setup is that due to the independent motion of the two Huber parts, it can easily accommodate relatively large-size equipment (furnaces, cryostats, pressure-cells etc.) necessary for various sample environments.

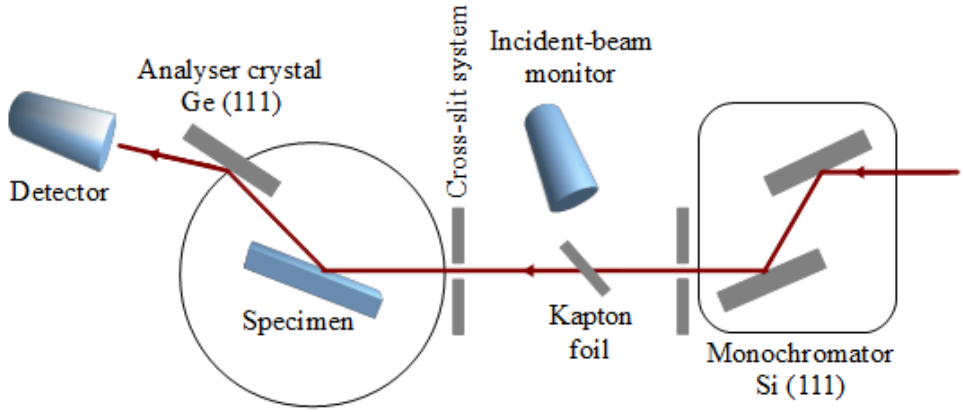

Figure 3. 7 Schematic view of the B2 high-resolution powder diffractometer at DESY/HASYLAB.

For the high-resolution setup used for most of our step-scanning measurements, Soller slits as well as a Ge(111) analyser crystal were mounted in front of the NaI scintillation detector. The desired wavelength is selected by a monochromator consisting of two water-cooled Si(111) crystals enclosed in a He-tank (Figure 3. 7). The wavelengths used for the measurements presented here were chosen between 0.6-1.2 Å. The primary intensity I_0 of the beam at the sample location is measured by a scintillation counter placed after the exit of the monochromator tank. In this way, identical counting statistics conditions may be ensured for intensity measurements performed at different 2θ scattering angles. Therefore, for the step-scanning as well as for image-plate detector measurements, the counting/exposure time is automatically adjusted so as to compensate for the decreasing intensity of the synchrotron radiation beam delivered the bending magnet insertion device.

The general expression for the intensity of a powder X-ray diffraction line is given by [150,151].

$$I_{hkl}(2\theta) \sim m_{hkl} \cdot LP(2\theta) \cdot |F_{hkl}|^2 \cdot A \qquad (3.\ 4)$$

where m_{hkl} is the multiplicity of the scattering plane (*hkl*), LP is the combined Lorentz and polarisation factor, F_{hkl} is the structure factor (accounts for the scattering power of all constituent atoms) and A is an absorption term also depending on the scattering geometry. For the case of the flat-specimen (Bragg-Brentano) triple-axis geometry of the high-resolution powder diffractometer used for the present experiments (Figure 3. 7), the Lorentz-polarisation (LP) factor is given by:

$$LP = \frac{1 - K + K \cdot \cos^2 2\theta \cdot |\cos 2\theta_A|}{2 \sin 2\theta \cdot \sin \theta} \qquad (3.\ 5)$$

where θ_A is the scattering angle of the analyser crystal and K represents the fraction of vertically polarised radiation in the diffraction plane. In the ideal case, the radiation is 100 % polarised in the horizontal plane of the synchrotron so that K = 0. In practical cases, K may however range between 5 to 15 %.

As direct measures of line broadening one may use the full-width at half-maximum FWHM: $\Gamma = 2\omega$ (where ω = half-width at half maximum or HWHM, given in °2θ or radians) or the integral breadth β, defined as the width of a rectangle with the same amplitude and area as the X-ray diffraction peak:

$$\beta = \frac{\int I(2\theta)d(2\theta)}{I_{\max}} = \frac{\int I(s)d(s)}{I_{\max}} = \frac{area}{amplitude} \qquad (3.\ 6)$$

3.3.4 In-situ high-temperature X-ray diffraction experiments

The crystallization and grain-growth of our MA powders was followed during in-situ continuous heating and isothermal experiments for temperatures as high as 800°C. The specimens are mounted into 0.3 μm quartz capillaries and placed into a STOE oven (Figure 3. 8). The sample holder also allows for the specimen rotation during the measurement, so that texture effects are minimized. The furnace is operated under continuous protective-gas flow (Ar). The specimen temperature is measured using thermocouples mounted in the immediate vicinity of the capillary sample holder. The scattered intensity is monitored for scattering angles of up to 120° 2θ using a semi-circular image-plate detector, which allows for the one-step acquisition of the XRD patterns. The acquisition times may be reduced to only a few minutes [145], so that time-resolved experiments are also possible with this setup.

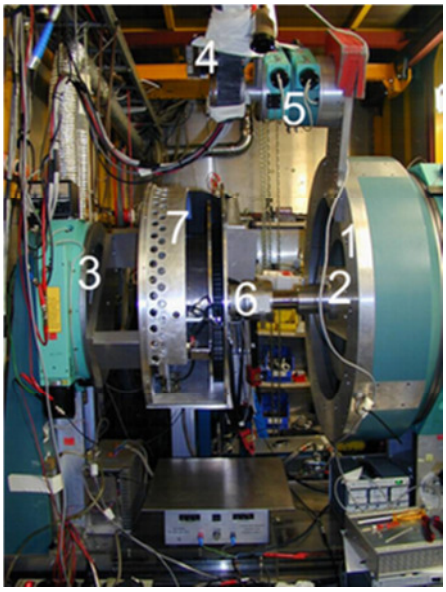

Figure 3. 8 View of the B2 diffractometer. The synchrotron beam enters the hutch from the back. The monochromator vessel is behind the diffractometer inside the hutch. 1: Huber circle 480 carrying the single counter. 2, 3: Huber circles 440 for sample environments or image-plate detector which can be moved laterally. 4: Single counter with analyser crystal and attenuator. 5: Two Huber circles 410 for counter alignment. 6: Stoe furnace. 7: Image-plate detector [153].

3.3.5 Diffraction data-analysis procedures used in the present work

In this work the convolution fitting method were implemented to correct the instrumental broadening [154].

After removing the instrumental broadening from the observed line profile h(2θ), it is possible to analyse the pure-specimen line profile, identify the sources of line-broadening and extract quantitative microstructural information. The main sources are the size and strain terms which are interconnected: for example, dislocations commonly cause strain but also arrange into boundaries between incoherently diffracting domains.

Scherrer [155] gave a basic first definition of the "apparent" coherent domain size:

$$\langle D \rangle_V = \frac{K\lambda}{\beta_S cos\theta} \qquad (3.\ 7)$$

The constant K depends on crystallite shape, but it is often taken equal to unity. The size broadening contribution is independent of the reflection order, that is, independent of diffraction angle 2θ. The domain size $<D>_V$ is a volume-weighted quantity.

For the analysis of the angular-dispersive diffraction patterns, the software package Peakfit@ from SPSS Science Inc. [156] was used. The experimental diffraction patterns were modelled by assuming a polynomial baseline and Voigt-type diffraction lines. Scattering arising from amorphous specimen holders (such as capillaries) were also taken into account. The Voigt function used for the present peak-shape analysis provides the Gauss (ω_G) and Cauchy-Lorentz (ω_L) components of the linewidth as fitting variables:

$$Voigt(2\theta) = a_0 \cdot \frac{\int_{-\infty}^{\infty} \frac{\exp(-t^2)}{\frac{a_3^2}{2a_2^2} + \left(\frac{x-a_1}{a_2\sqrt{2}} - t\right)^2} dt}{\int_{-\infty}^{\infty} \frac{\exp(-t^2)}{\frac{a_3^2}{2a_2^2} + t^2} dt} = I_0 \cdot \frac{\int_{-\infty}^{\infty} \frac{\exp(-t^2)}{\frac{\omega_L^2}{2\omega_G^2} + \left(\frac{2\theta - 2\theta_0}{\omega_G\sqrt{2}} - t\right)^2} dt}{\int_{-\infty}^{\infty} \frac{\exp(-t^2)}{\frac{\omega_L^2}{2\omega_G^2} + t^2} dt} \qquad (3.8)$$

together with the usual parameters: peak position 2θ, amplitude I_0 (taken as the diffracted intensity at 2θ), the full-width-half-maximum (FWHM = β) and the peak area (A).

The instrumental resolution function was determined from experimental data on standard NIST 660a (LaB_6) specimen. This specimen is particularly suited for performing the instrumental broadening correction, due to its sharp Bragg reflections. Lanthan-hexaboride was used to determine the wavelength of the monochromatic radiation as well as the intrinsic linewidth (instrumental broadening $\beta_g(2\theta)$) of the diffraction lines (Figure 3. 9a).

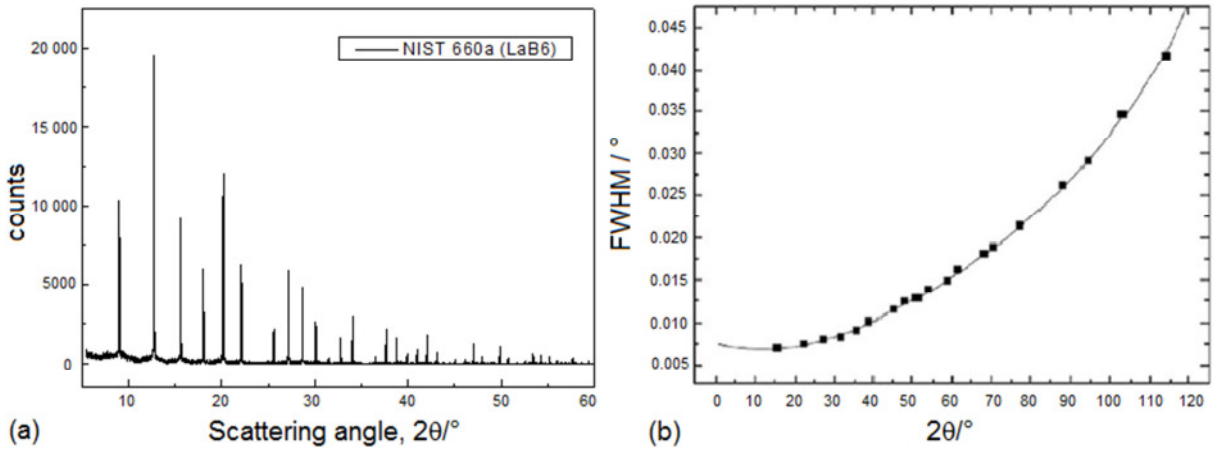

Figure 3. 9 (a) X-ray diffraction pattern of the NIST 660a (lanthan-hexaboride LaB_6) standard specimen used to determine the resolution function of the B2 instrument. (b) Instrumental resolution function of the B2 high-resolution diffractometer (NIST 660a lanthan-hexaboride LaB_6 standard).

Figure 3.9b illustrates a fit of the measured FWHM(2θ) for the LaB_6 specimen using the Caglioti relation (3.9). The model parameters are U = 0.00309, V = 0.0006 and W = 0.00151.

The instrumental resolution function determined in this way was further used to deconvolute the instrumental broadening contribution from the measured diffraction patterns.
Most often, the relation proposed by Caglioti et al. [154] relation is used:

$$FWHM^2(2\theta) = U\cdot\tan^2\theta + V\cdot\tan\theta + W \quad (3.9)$$

where FWHM represents the full-width at half-maximum of the Bragg reflections.
The instrument resolution function was obtained using an interpolation procedure based on the Cagliotti formula (3.9) for the angular range of interest (10÷70°2θ). The instrumental broadening correction was performed for the experimental FWHM values according to:

$$\beta_f^2 = (\beta_h - \beta_g)\cdot\sqrt{\beta_h^2 - \beta_g^2} \quad (3.10)$$

where the indices *h*, *g* and *f* indicate the experimental β_h, instrumental β_g and specimen β FWHM or integral breadth contributions, respectively.
The values for the corrected FWHM (β_f) were used to evaluate the particle size $\langle D\rangle_V$ according to the Scherrer equation (3.7), therefore often assuming microstrain-free specimens. The shape constant *K* was conventionally taken equal to unity ($K \approx 1$).
Additional information on the temperature evolution of average grain-sizes could be obtained in some cases directly from the Cauchy-Gauss components of the diffraction linewidths, within the limits of the Halder-Wagner approximation. The present analysis was restricted to the strongest (18, 29) and (20, 32) icosahedral reflections.

3.3.6 In-situ high-pressure high-temperature diffraction experiments

The in-situ X-ray diffraction measurements under applied pressure were performed at the MAX80 instrument installed at the F2.1 beamline at HASYLAB/DESY (Figure 3. 10). The MAX80 instrument uses a cubic-anvil-type press, which is known to provide better results for isotropic pressure generation compared to other multiple-anvil high-pressure devices [157].

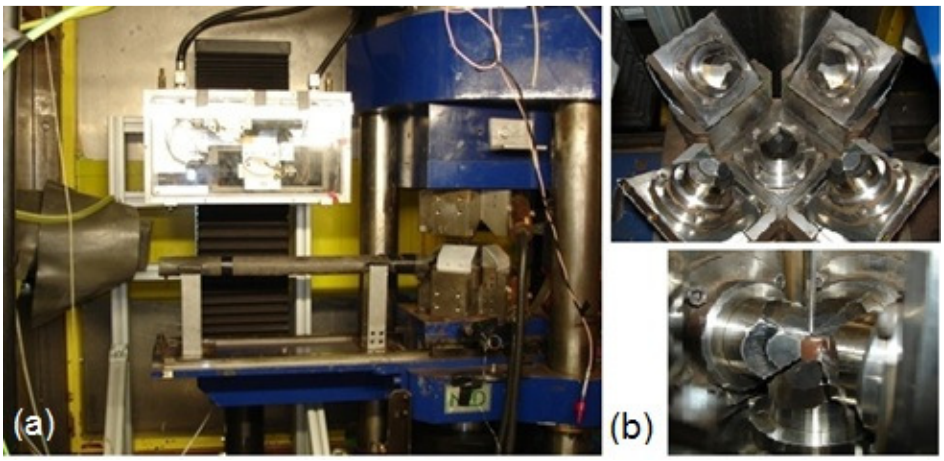

Figure 3. 10 (a) General view of the high-pressure MAX80 set-up at the F2.1 beamline (HASYLAB/DESY). (b) Geometric arrangement of the WC anvils and the amorphous boron cube (sample container). Picture taken from [158].

The external pressure is generated by six syncronized anvils (sintered 6Co-WC). Teflon sheets are squeezed between the anvils, in order to reduce friction and provide electrical insulation during high-temperature experiments. The applied force is generated by a uniaxial hydraulic press, and equally transmitted to each of the faces of the cubic pressure medium formed by the anvils (Figure 3. 10).

Both white (energy-dispersive EDX mode) and monochromatic (angular-dispersive ADX mode) incident beam X-rays can be used. The incident beam divergence is about 0.3 mrad; additional slit systems are used to select a narrow parallel incoming beam. The vertical gap between the anvils is smaller than 0.5 mm so that it also acts as vertical beam definer. The instrument limitations are Pmax = 6÷8 GPa depending on the size of the sample container and anvils and Tmax = 1800°C. The experiments reported here were however performed only until a maximum temperature of 900°C.

Sample preparation: the powder sample is mounted inside amorphous boron - epoxy resin cubic container of either 4 or 6 mm edge size (Figure 3. 11). A graphite cylinder and copper rings are provided for current heating. The specimen is mounted within a boron nitride cylinder together with the pressure calibration material (NaCl). Boron nitride powder layers further separate the sample from the NaCl pressure marker and the graphite cylinder, so that the sample is protected against chemical contamination during the diffraction experiment.

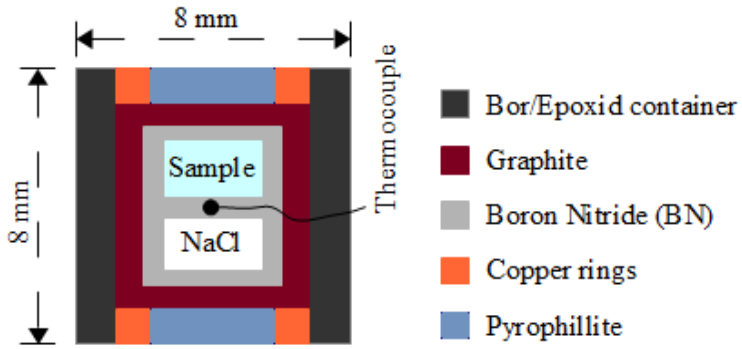

Figure 3. 11 Schematic illustration of the high-pressure sample preparation procedure.

The main differences of the energy dispersive X-ray diffraction EDX method to the conventional angular-dispersive method using monochromatic X-rays are as follows:

- the incident beam is polychromatic ('white' beam),
- the scattering angle ($2\theta_0$) is fixed during the experiment but may be optimized for each particular measurement. There is no mechanical movement during the recording of the diffraction patterns,
- the detector is an energy-dispersive one,
- all reflections are recorded simultaneously,
- the counting time is relatively short due to the high detector efficiency and the simultaneous recording of reflections.

The main advantage of the EDX diffraction method is the simultaneous recording of all reflections and short exposure times, which are essential to studies of structural transitions including their kinetics. The fixed geometry is also very convenient for in situ experiments when cryostates, ovens or high-pressure cells are used.

The EDX method relies on the use of a well-collimated and polychromatic (white) incident synchrotron radiation beam [159,160]. The photon energy distribution of diffracted photons, measured at a fixed scattering angle ($2\theta_0$), has the role of an analyzer. Each {hkl} set of crystal lattice planes with interplanar spacing d_{hkl} will select from the incident white beam and scatter into the detector only those photons having an energy E_{hkl} satisfying the Bragg equation :

$$2d_{hkl}sin\theta_0 = \lambda_{hkl} = \frac{hc}{E_{hkl}} = \frac{12.398}{E_{hkl}} \quad (\text{keV}\cdot\text{Å}) \qquad (3.\ 11)$$

where λ is given in Å and the energy in keV (h is Planck's constant and c the velocity of light). The Bragg equation is usually written in the more convenient form:

$$d_{hkl}E_{hkl}sin\theta_0 = 6.199 = C \quad (3.\ 12)$$

where the constant term C on the right-hand side is given in (keV·Å). The integrated intensity of a reflection record by the detector along a unit length of the Debye-Scherrer ring is given by the formula [161]:

$$I_{hkl}(E) = C \cdot \{I_0(E) \cdot E^{-2} \cdot m|F|^2 \cdot \eta(E)A(E,\theta_0) \cdot L_p(E,\theta_0)\}_{hkl} \cdot sin^{-3}\theta_0 \cdot \Delta\theta_0 \quad (3.\ 13)$$

where C is a constant for a given experiment (given by Eq. 3.12), $I_0(E)$ is the incident beam intensity per unit energy range, m_{hkl} the multiplicity factor, and F_{hkl} the structure factor including the atomic scattering factors with the corresponding Debye-Waller factor and $\Delta\theta_0$ is a convolution of the incident and diffracted beam divergences. $\eta(E)$ is the detector quantum efficiency, which must either be be measured or taken from efficiency curves supplied by the detector producer.

3.4 Thermoanalytical Characterization

Thermal analysis methods are used to investigate the physical and/or chemical properties of materials as they change with temperature. Differential scanning calorimetry (DSC) was used here to identify the temperature ranges for the important phase transformations and their thermal stability. Also, the crystallization kinetics of Al-Cu-Fe as-milled alloys under isochronal conditions was analysed and the crystallization process for the composites was studied.

3.4.1 Differential Scanning Calorimetry

The basic idea in the DSC is to measure the required heat flow rate difference to keep the sample and reference at the same temperature during heating and cooling. In order to achieve reliable results from DSC measurements the thermal conditions always have to be comparable to each other. DSC determines the temperatures of the material transformations and quantifies their heat exchanges, i.e. enthalpy changes in the alloys.

The measurements were performed using a heat flow NETZSCH 404 C Pegasus DSC under high purity argon with disc-shaped samples having a weight of approximately 13 mg encapsulated in platinum pan coated with alumina. An empty pan was used as a reference. During the measurements, the samples were protected with high purity flowing argon.

Temperature scans were made in the range 50 – 800°C with constant heating and cooling rates of 5, 10, 15, and 20 K/min. The amount of energy, which has to be supplied to or withdrawn from the sample to maintain zero temperature differential between the sample and the reference is the experimental parameter displayed as the ordinate of thermal analysis curve.

DSC measurements in the low temperature region were done with two devices: a power compensated PERKIN-ELMER Pyris Diamond DSC in the workgroup of Polymer Physics and a Mettler Toledo DSC 1 in the Institute of Biomedical Engineering (IBMT) at the University of Rostock.

3.5 Mechanical characterization

In the thesis, nanoindentation and Vickers microindentation testing, as well as compression strength testing were carried out to evaluate the mechanical properties.

The nanoindentation tests were conducted with a Berkovich indenter using a fully calibrated Nano Indenter UNMT (Universal Nano/Micro Tribometer, CETR). In each test run, the indenter was driven into the specimen surface (loading half-cycle) under a load gradually increased to the predetermined peak value, unloaded gradually to 10% of the peak load (unloading half-cycle) after being held at peak load for 30 s, and then driven again into the specimen surface to a higher value of the peak load. Such a procedure repeated for twelve times with increasing peak loads and resulted in a load-displacement curve containing twelve loading/unloading cycles. For each material, two or three load-displacement curves were measured. Load and displacement are continuously monitored during a loading–unloading sequence and hardness as well as Young's modulus is then calculated from the load–displacement curves taking into account the geometry of the indenter.

The micro hardness measurements were performed using a Vickers micro hardness test apparatus under a known load. Pressing a point with a diamond tip on the sample surface with a known force, the size of the diagonal is taken as a measure of the hardness. In the composite samples, the hardness has been tested with a small load (50 N), in different points of the pellet. In the quasicrystalline samples, the overall structure was tested using a load of 0,1 kg. An average of minimum 6 hardness indentations on each sample surface was measured.

Compressions strength tests have been also performed at room temperatures to assess the strength of the composite materials. The testing was conducted with a Zwick Universal Test machine at strain rates of 0.01 and 1/s. Tests were run using constant velocity control profiles. Load and stroke were acquired during the compression test by a data acquisition system and later converted to true stress-true strain curves.

3.6 Biocompatibility tests

In this work, only preliminary in vitro tests were performed at the Biology Faculty of the University of Rostock (Dr. Margareta Lantow). In order to test the biocompatibility and stability of the composites, the samples were incubated in simulating body fluid (SBF, according to (Kokubo and Takadama, 2006) which has ion concentrations nearly equal to those of human blood plasma. Therefore, the composites were incubated in 50 ml tissue culture tubes (TPP, Germany) in SBF at 37°C, 5% CO_2, 120 rpm for 1 and 3 months in an incubator shaker (Controlled Environment Incubator Shaker, New Brunswick Scientific Co. Inc., Germany). Following, the samples were dried at room temperature and their weight was determined.

For studying the releases of the Al, Cu and Fe into SBF solution, their concentrations were measured in the extracts by inductively coupled plasma-optical emission spectroscopy (ICP-OES) using an IRIS INTREPID II spectrophotometer (Thermo Fisher, Schwerte, Germany) equipped with a CID detector at Lehrstuhl für Kolbenmaschinen und Verbrennungsmotoren Universität Rostock. The operating parameters and analytical line wavelengths chosen for the measurements were typical. To ensure high-quality trace metal detection, a blank sample of body simulation fluid was used for correction of analytical signals measured by ICP-OES. The detection limit was 0.01 mg/l.

Human MG63 osteoblastic-like cells were cultured and further cytotoxicity tests were performed to analyze the cellular growth and viability. Details of the tests are presented in the Appendix.

Chapter 4

Phase Evolution Analysis of the i-Al-Cu-Fe System

This chapter is devoted to a quantitative and qualitative study of mechanically activated Al-Cu-Fe ternary alloys and their evolution towards ideal quasicrystals. In order to get a better understanding of the solid state transformation during microwave (MW) and SPS processing, we investigated the solid-state transformations by in-situ high temperature X-ray diffraction (HTXRD) (recorded at the F2.1 beamline at DESY/HASYLAB) and DSC. We analyzed different alloy compositional ranges to determine the best Al-Cu-Fe alloy composition which results in the formation of stable quasicrystalline phase. The observation temperature ranges from 20 to 800°C. Different phase transitions are identified and discussed. Their transition temperatures are close to those expected for structural bulk phase transitions. After finding the most suitable composition stoichiometry in the $Al_{67}Cu_{23}Fe_{10}$ alloy we studied the influence of the milling time on the formation of pure icosahedral (i) phase. We have succeeded to obtain a stable single phase quasicrystal directly by mechanical alloying. Possible mechanisms which could explain the growth of the single icosahedral phase during milling are discussed. Mechanical properties of sintered pellets by hot pressure (HP), microwave heating (MW) and spark plasma sintering (SPS) are compared and discussed.

4.1 Phase Transitions and Phase Stability of Al-Cu-Fe Alloys

A provisional vertical section along the line $Al_{70}Cu_{20}Fe_{10}$ and $Al_{64}Cu_{24}Fe_{12}$ is proposed and shows the phases that exist at equilibrium at various temperatures in this range of compositions. In-situ XRD analysis was used in order to get a better understanding of the solid state transformations during DSC.

Figure 4. 1 shows the sequence of diffraction patterns collected in-situ during non-isothermal annealing. Selected diffraction patterns taken at different temperatures are also shown (Figure 4. 2) to illustrate the solid-state transformations during non-isothermal annealing more in detail. The Al, Cu and Fe powders are quite similar in nature. They are all soft and would be expected to aggregate readily, noting that while Fe crystals are naturally body-centered cubic while aluminum and copper have a face-centered cubic structure.

The as-milled powder mixture contains significant amounts of remaining elemental Al fcc, Cu bcc and Fe fcc and a small amount of Al_2Cu tetragonal phase. During continuous heating, the transformation of the as-milled Al-Cu-Fe follows a complicated path. As shown in Figure 4. 1, at least three stages can be distinguished for different alloy composition, although the number of elementary processes taken place is even higher. The order of phase transformation depicted in Figure 4. 1 is the same for all six compositions and illustrates that the Al-based intermetallics initially formed are enriched by either Cu (Al_2Cu) or Fe ($AlFe_3$), so copper and iron are separated as much as possible in the initial stage of transformations. The reaction Al + Cu $\rightarrow$ Al_2Cu takes place after 150 °C. The intermetallic Al_2Cu is present in the phase composition until 350 – 450 °C for all the compositions with some variations. The metastable cubic Al(Cu, Fe) phase, which can be seen almost during the entire heating treatment, decomposes, reorders and finally transforms into the tetragonal Al-rich ω-phase.

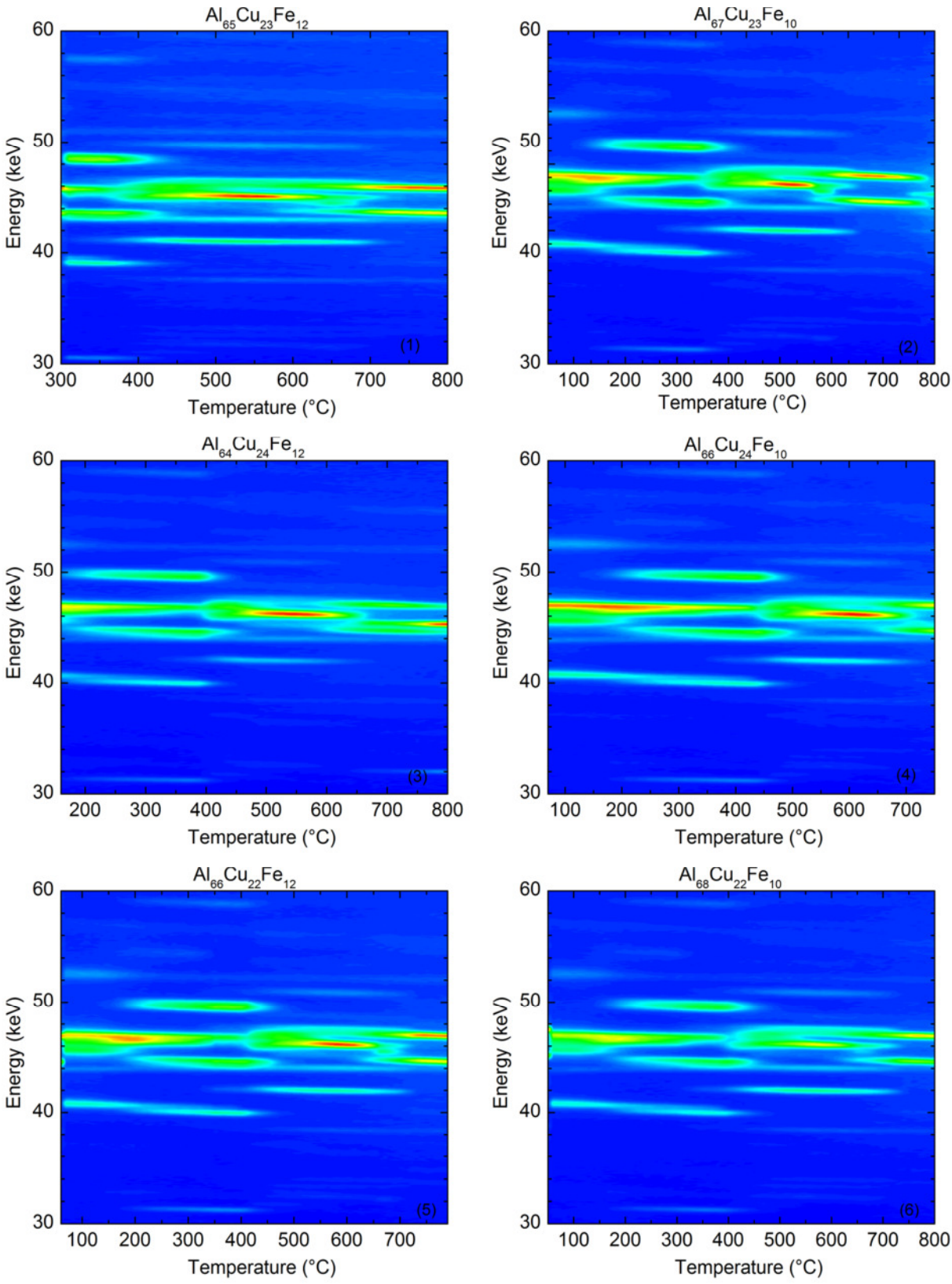

Figure 4. 1 In-situ EDXRD diffractograms (HASYLAB/F2.1) showing the phase composition change under heating with 10 K/min in different Al-Cu-Fe mechanically alloyed compositions: (1) $Al_{65}Cu_{23}Fe_{12}$, (2) $Al_{67}Cu_{23}Fe_{10}$, (3) $Al_{64}Cu_{24}Fe_{12}$, (4) $Al_{66}Cu_{24}Fe_{10}$, (5) $Al_{66}Cu_{22}Fe_{12}$ and (6) $Al_{68}Cu_{22}Fe_{10}$.

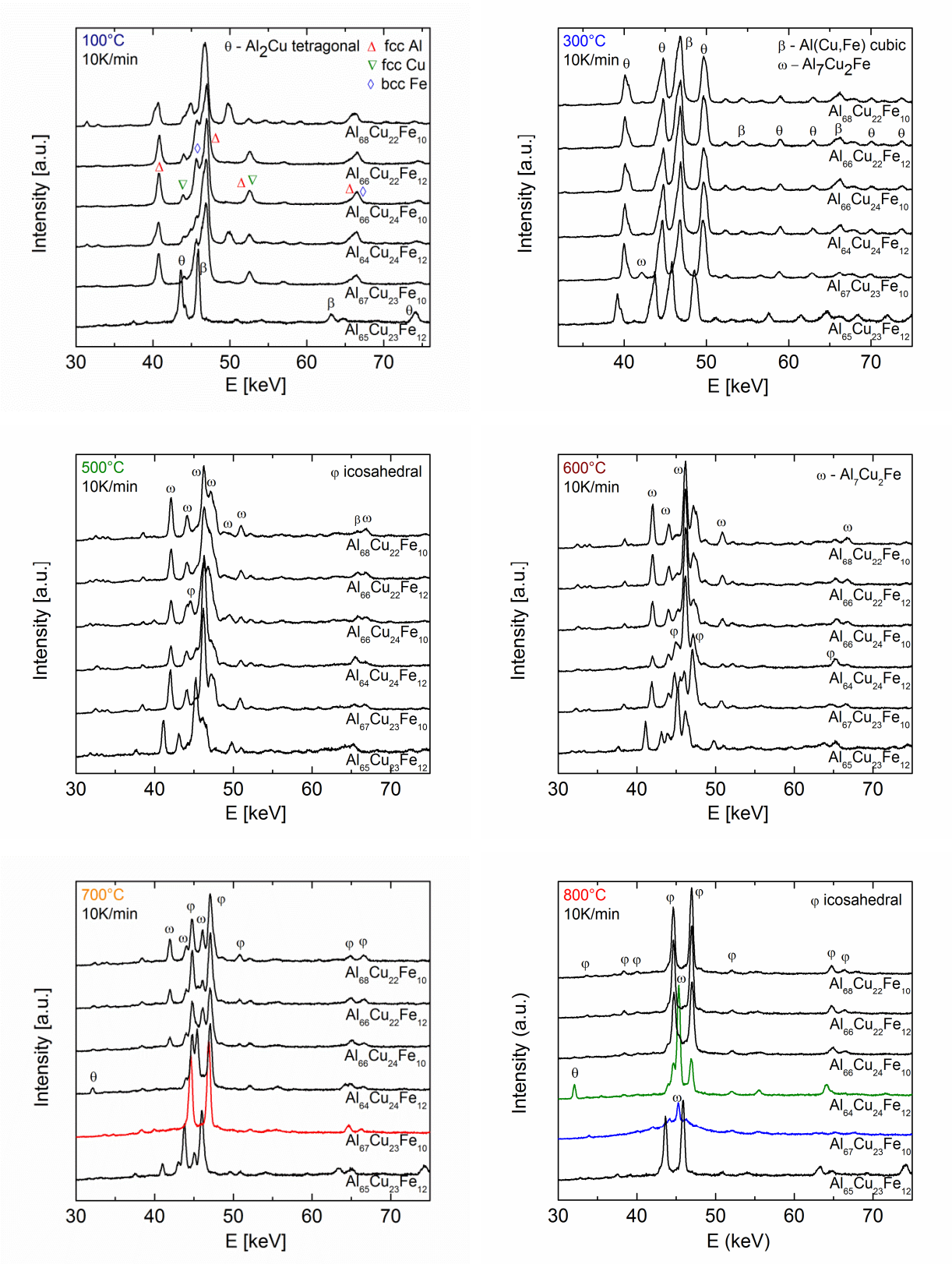

Figure 4. 2 Selected EDXRD patterns (HASYLAB/F2.1) showing the solid-state reactions at selected temperatures in different Al-Cu-Fe compositions.

The ω-Al_7Cu_2Fe is the main precursor of the quasicrystalline icosahedral φ-phase, in good agreement with other literature results [162,163]. The small difference in the atom positions between the ω precursor and the φ-phase explains the low energy required for the phase transition.

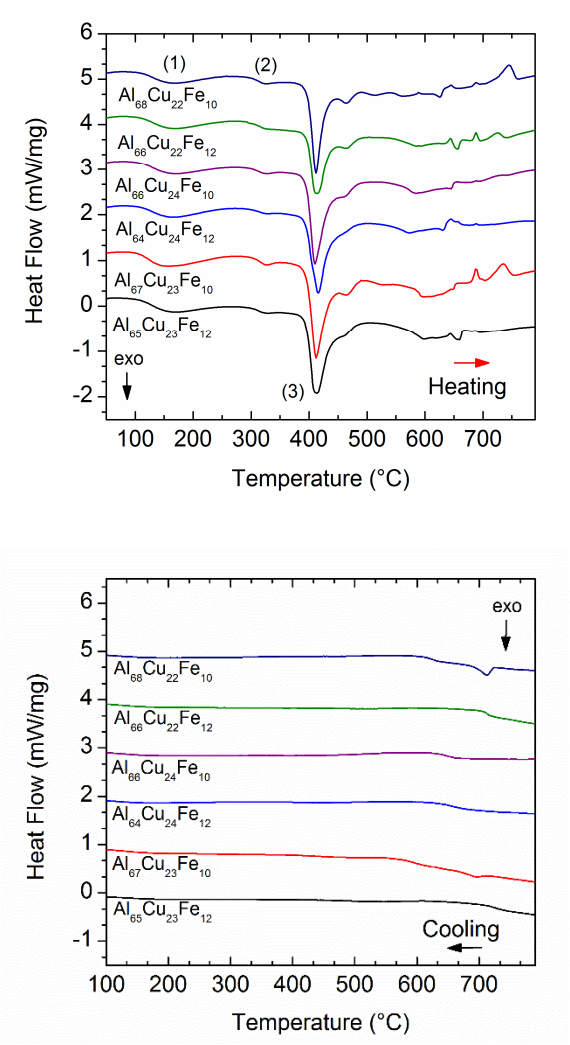

Figure 4. 3 DSC heating and cooling curves performed at β = 10 K/min for the as-milled Al-Cu-Fe samples: (1) $Al_{65}Cu_{23}Fe_{12}$, (2) $Al_{67}Cu_{23}Fe_{10}$, (3) $Al_{64}Cu_{24}Fe_{12}$, (4) $Al_{66}Cu_{24}Fe_{10}$, (5) $Al_{66}Cu_{22}Fe_{12}$ and (6) $Al_{68}Cu_{22}Fe_{10}$.

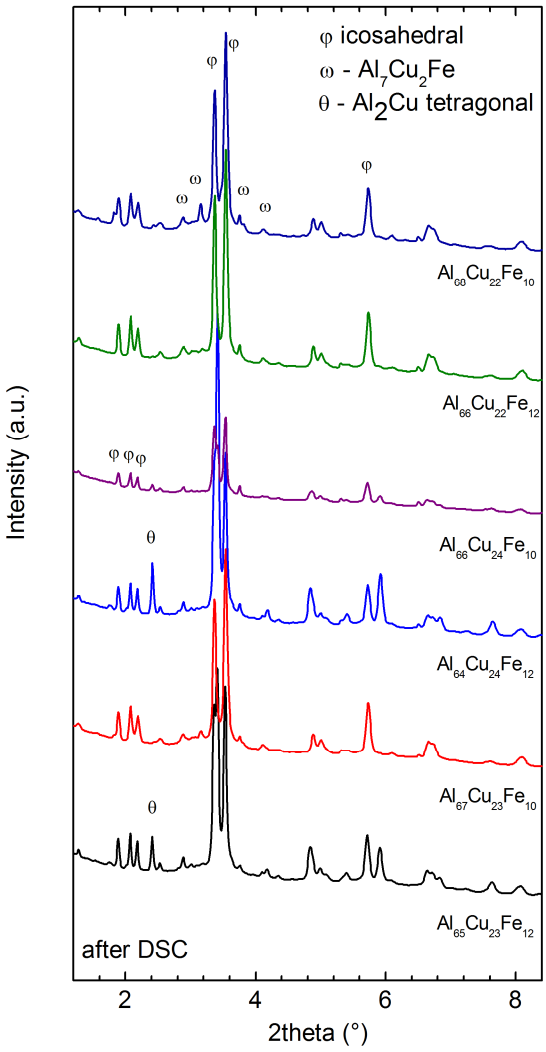

Figure 4. 4 X-ray diffraction patterns measured after the DSC treatment (HASYLAB/beamline BW5, λ = 0.1239 Å).

The nucleation of the quasicrystalline phase takes place the fastest at 510°C for the alloy composition of $Al_{66}Cu_{22}Fe_{10}$ and develops as a single phase at 700°C where it remains stable until 760°C. For the $Al_{67}Cu_{23}Fe_{10}$ composition, the φ-phase nucleates at 570°C and transforms

into a single phase at 670°C being stable until 800 °C. These results establish that there exists a single phase domain where the φ-phase is perfect and remains stable for most of the analysed compositions except for $Al_{64}Cu_{24}Fe_{12}$ where is never present as a single phase.

Figure 4. 3 shows the typical DSC curves for the as-milled samples, recorded at a scan rate (β) of 10 K/min. On heating the system, several broad exothermal peaks are observed. In general, the main transformation processes of the sample heated in the DSC set-up, marked by numbers in the heating curves were also identified in the EDXRD patterns. In all sample compositions, at the initial stage of heating, Al-based intermetallic enriched by Cu or Fe are formed in the range of 100 – 350°C (2). Also, the pure elements dissolve in the intermetallic matrix and about 15-20 at.% of the Al_2Cu phase form in this temperature interval (1). In the next temperature range (350 – 450°C) the ternary intermetallic compound Al_7Cu_2Fe appears, which is the main precursor of the icosahedral phase (3). A small exothermic event can be seen between 450 – 500°C and could correspond to the formation of the $AlFe_3$ phase (4). The process of φ phase formation starts after 450°C (5). Some weak exothermic events, which cannot be related to known phases, can be also observed in the DSC curves. In $Al_{67}Cu_{23}Fe_{10}$, $Al_{66}Cu_{22}Fe_{12}$ and $Al_{68}Cu_{22}Fe_{10}$ compositions show an endothermic event at 720 – 750°C which can be attributed to a melting process.

In the subsequent DSC cooling processes the sample only undergoes one transformation around 700°C showing that the ternary phase transformation is irreversible. XRD was performed on the samples after the DSC treatment in order to demonstrate that the QC phase is stable during cooling. The XRD spectra presented in Figure 4. 4 show indeed that, the QC phase is still present here, although a secondary ω phase can be found, as well. The formation of the secondary ω-phase during cooling suggests that the cooling rate could affect the stability of the single φ-phase.

The onset and end temperatures observed for the icosahedral transition in nanostructured Al-Cu-Fe alloy specimens are summarized in Figure 4. 5. One first observes that differential scanning calorimetry measurements detect the onset of the phase transitions at lower temperatures than high-temperature XRD. This is due to the fact that a sufficient number of crystal grains must have formed to provide detectable X-ray diffraction lines.

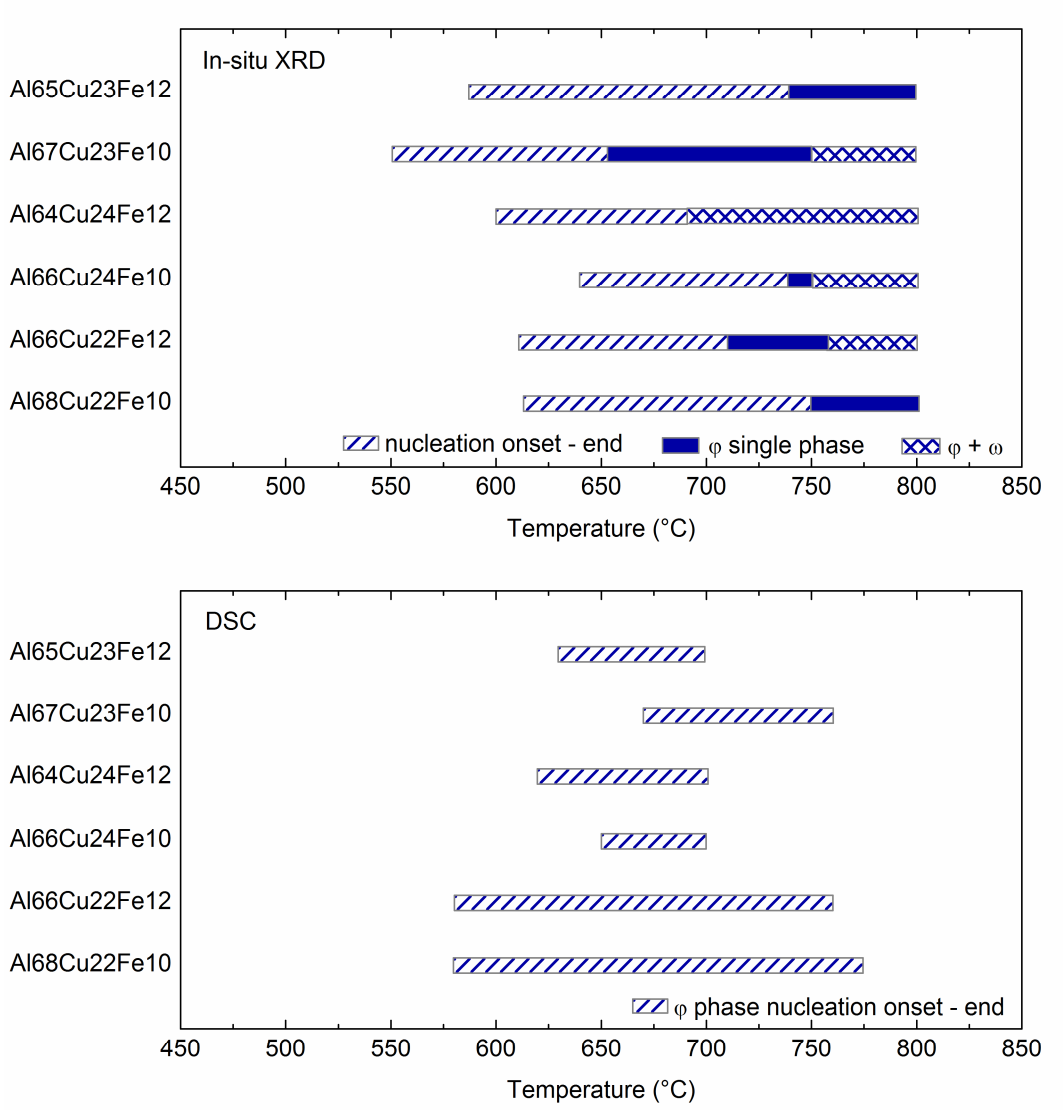

Figure 4. 5 Transformation temperatures for the icosahedral transition in nanostructured Al-Cu-Fe alloys as determined by HT-XRD and DSC experiments (uncertainty ≈ 20°C).

Although both in-situ XRD and DSC samples were heated with 10 K/min it is still questionable to associate the DSC maxima with any phase transformation from the XRD data only. Each DSC maximum corresponds to more than one phase transformation. In fact, these DSC peaks correspond to the increase of the total rate of solid-state reactions. The formation of ternary QC alloys is accompanied by a relatively large thermal effect; the total exothermic heat determined form the DSC curves was ~ 18 kJ/mol. At the same time the interaction character in the corresponding binary systems are very different. The Al-Cu and Al-Fe are characterized by negative heats of intermetallic compound formation (-12,2 kJ/mol for Al_2Cu, -22.2 kJ/mol for AlFe, -19.9 kJ/mol for AlCu [164]) whereas the Fe-Cu system has a significant positive heat of mixing (~ + 15 kJ/mol [165]). The repulsion forces between Cu

and Fe have an important influence on the element distribution in the phases during the transformation on heating. During subsequent heating the chemical composition of phases gradually approaches to the average chemical composition of the alloys. The XRD data for temperatures higher than 400°C show that ternary phases are formed from the binary Al-based phases with the evolution of heat. Besides, the DSC cooling curves and the XRD spectra taken after cooling, show no reverse of the ternary phase into a binary phase, which means that, in spite of chemical repulsion of the Cu and Fe atoms, the Al-based ternary phases are more thermodynamically stable than the mixture of the binary intermetallics. This indicates strong atomic bonds in such ternary structures, including the QC phase.

The results obtained by differential scanning calorimetry (DSC) and X-ray diffraction (XRD) confirm that the icosahedral phase (i-phase) is formed by a peritectic reaction. A single i-phase can be obtained during heating in all studied compositions except for $Al_{64}Cu_{24}Fe_{12}$. In this composition range, although the φ-phase appears between 620 – 700°C, it never develops into a single phase during continuous heating. The longest time pure icosahedral phase remains stable (from 650 – 750°C) is in the $Al_{67}Cu_{23}Fe_{10}$ alloy composition. This is the reason we have chosen this composition for the study of milling time influence on the formation of quasicrystals and further hot pressing processing.

4.2 The influence of milling time on the morphology and the formation of quasicrystals in $Al_{67}Cu_{23}Fe_{10}$ alloys

The process of preparing the quasicrystalline phase was optimized by varying the composition of the initial batch. As shown in our previous experiments, single-phase quasicrystals can be obtained in several Al-Cu-Fe compositions by 10 hours MA followed by annealing. Salimon et al [162] stated that the milling conditions should be taken into account in order to produce effectively single-phase quasicrystals. Our previous investigations showed that $Al_{67}Cu_{23}Fe_{10}$ composition (where the concentration of elements is given in at. %) is optimum for producing single quasicrystalline phase by MA upon subsequent heating. We chose this alloy to investigate the effect of the milling time on the formation of the φ-icosahedral phase, since the quasicrystalline phase formed starting from this composition mixture was shown to be stable over a longer temperature range (from 650 – 750°C). Samples taken after 10, 20, 40 and 80-hour milling were examined.

SEM, EDX and XRD studies were conducted on the powders. SEM looks at the shape and structure of the milled powder particles, while the chemical composition was investigated by EDX, to determine whether the samples were being contaminated by material from the mill wall. XRD analysis shows the phase composition after different milling times and in-situ XRD the phase evolution during heating. X-ray diffraction line broadening was used to determine changes in the average grain sizes distributions in the ball-milled materials.

The SEM investigation of the $Al_{67}Cu_{23}Fe_{10}$ milled powders (see Figure 4. 6) showed flake particles developing from the differently shaped starting powders. The equilibrium morphology of the powders resulting from cold-welding and fragmentation processes is generally irregular, featuring both coarser that coexist with finer isolated plate-like particles. The size of the alloy particles decreases from 5 – 20 μm after 10-hours milling to 2 – 10 μm after 20-hours of milling. The idea that the composite particles after 10 hours include fragments of the elemental starting powders is confirmed by the XRD spectra taken after milling (Figure 4. 8a). After 20 hours the individual elemental particles have mostly been captured by welding to other particles. Toward 40 hours of milling an increasing number of composite particles with the different ingredients arranged in parallel layers appear in the coarser size fractions. During this period, there is also a substantial increase on the relative amounts of the coarse size fractions, but also on the amount of the finer particles. This powder particles are probably pieces fractured from the edges of the coarse composite particles, which were not cold welded to other lamellae. The powder size does not change drastically during this time period but the plate-like particles tend to transform into more equiaxed-like particles. If the processing time period continues for 80 hours, there is a sharp decrease in the amount of very coarse plate-like particles and a trend toward more equiaxed dimensions (see Figure 4. 6 k, l). Along with elongated particles and particles with sharp edges, the powder contains rather many particles of a polyhedral shape, especially in the 80-hour milled samples. Ultrafine alloy particles cold-welded onto flat particle surfaces are observed as well. At this point, the welded layer on the balls and the vial wall was quite thick which implies that plastic deformation and cold welding occurred predominantly by the compression of free particles between colliding balls rather than by the addition of particles to the welded surface layers followed by de-welding to give coarser composite particles.

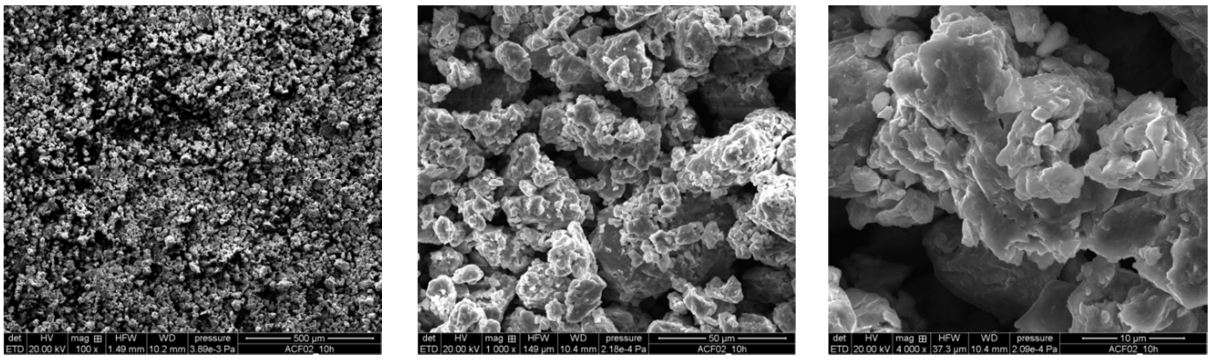

a) 10h, 100x b) 10h, 1000x c) 10h, 4000x

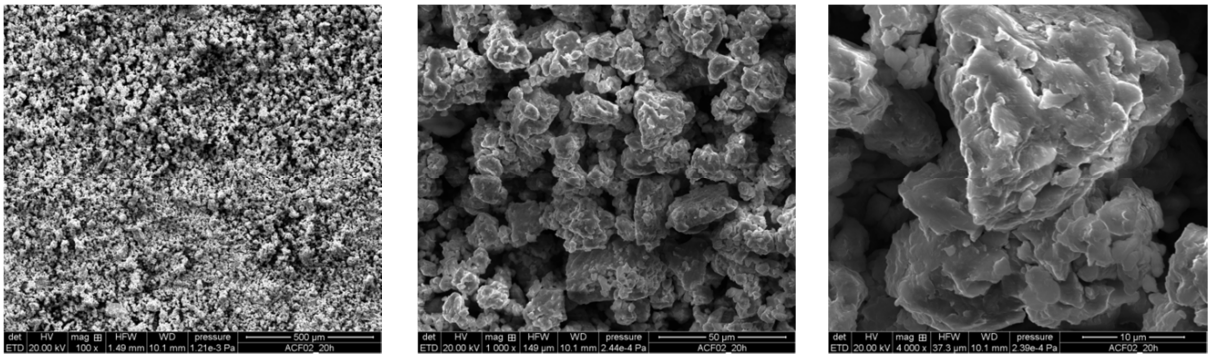

d) 20 h, 100x e) 20 h, 1000x f) 20 h, 4000x

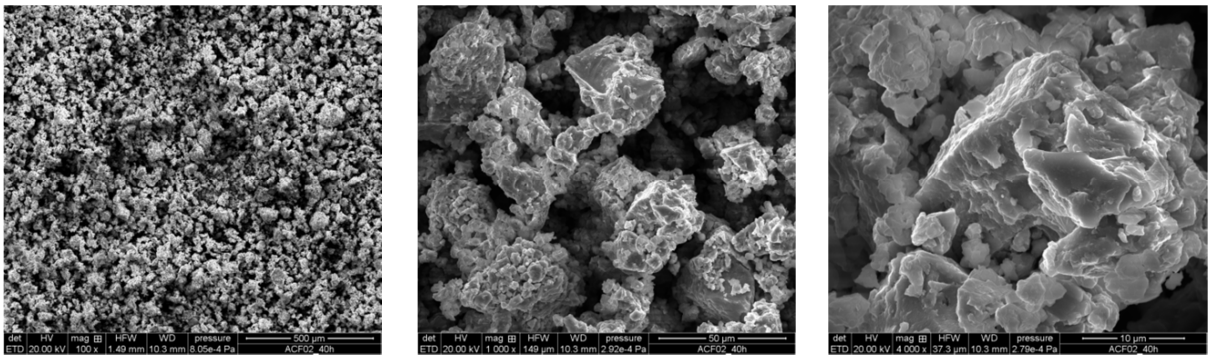

g) 40 h, 100x h) 40 h, 1000x i) 40 h, 4000x

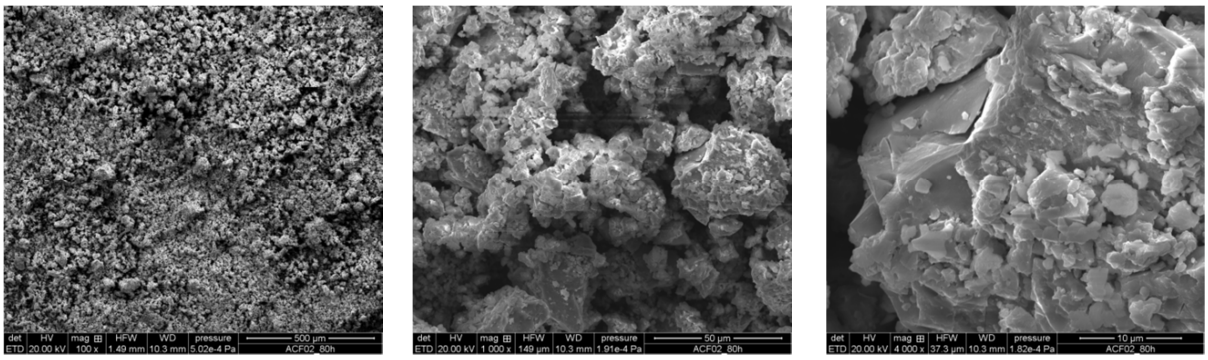

j) 80 h, 100x k) 80 h, 1000x l) 80 h, 4000x

Figure 4. 6 SEM micrographs of the $Al_{67}Cu_{23}Fe_{10}$ ball-milled powders for a), b), c) 10 hours, d), e), f) 20 hours, g), h), i) 40 hours and j), k), l) 80 hours. Small, equiaxed particles have shown that have escaped heavy processing during their time in the mill. The larger sharp-edged particles become more common as milling progresses.

In addition to SEM study, a cursory EDX analysis was made of the early samples to see if there was significant contamination of the material. The analytical compositions of the final powders are all very close to the starting nominal values. There was however small amount of oxygen (< 2 wt. %) to be found. A slightly higher Fe content (up to 3 at. %) was due to milling media debris mixed into the alloys during 80 hours milling (see Table below). Taken into account that the accuracy of the measurement lies at ~ 2 %, one can say that almost no traces of contamination from the milling tools were found after 10, 20, 40 hours processing and these alloys show a nominal composition which is close to the one in the initial batch of 67 at% Al, 23 at% Cu and 10 at% Fe (see Figure 4. 7).

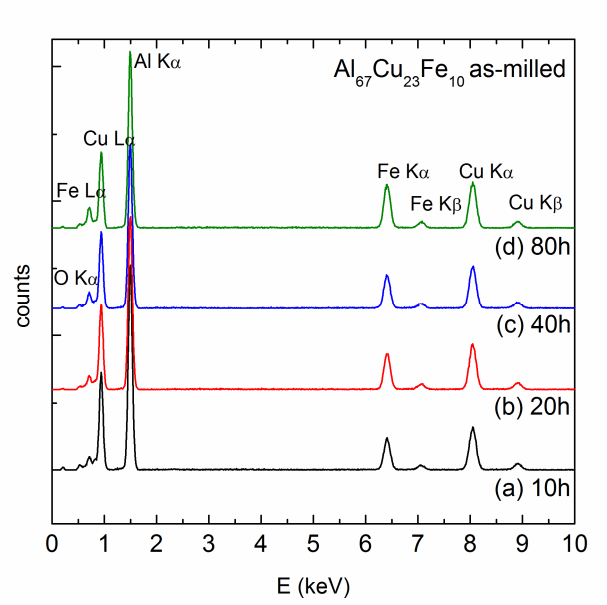

Element	At. %			
	10h	**20h**	**40h**	**80h**
Al	63,4	66	64,4	62,1
Cu	22,6	23,2	23	23
Fe	10,2	10,6	11,2	13,6
O	1,6	1,2	1,4	1,3

Figure 4. 7 EDX spectra showing the element distribution (left) and the table showing the composition of the alloy after milling in atomic percent (at. %).

The complex interplay between chemical alloying phenomena and structural deformation of the powders makes the interpretation of mechanical alloying mechanism extremely complex. The X-ray diffraction patterns from mechanically milled $Al_{67}Cu_{23}Fe_{10}$ powders after different milling times (10, 20, 40 and 80 h) are shown in Figure 4. 8. The alloy milled for 10 hours shows sharp diffraction peaks of elemental Al, Cu and Fe and a small peak from the Al_2Cu phase. Milling for 20 hours leads to a disappearance of remaining Al, Cu and Fe content. The amount of Al_2Cu phase increases after 20 hours of milling and some amount of disordered Al(Cu, Fe) intermetallic phase with a bcc structure is formed. If the milling continues up to 40 hours, the homogenization of the Al-Cu-Fe alloy is gradually completed, the disordered Al(Fe, Cu) compounds rearrange into a primitive cubic structure, and a certain amount of

ternary phase with a bcc structure having Al_3Fe as prototype is formed. The pattern shown in Figure 4. 8(d) reveal that the formation of a single φ-phase is possible by MA directly, when the elemental mixture is processed for 80 hours. The QC phase forms via reordering of the ω-Al_7Cu_2Fe intermetallics and remains the single constituent phase under longer processing time. The diffraction pattern corresponding to the icosahedral phase was indexed using the Cahn indeces (M, N), as described in Chapter 3.

Salimon el al. [162] also reported the production of a QC phase directly during MA in $Al_{67}Cu_{22}Fe_{11}$ after only 1 hour of milling but as a metastable phase. A longer processing time resulted in their case in the dominance of the Al(Cu, Fe) cubic phase which we observed in our system after 20 hours of milling.

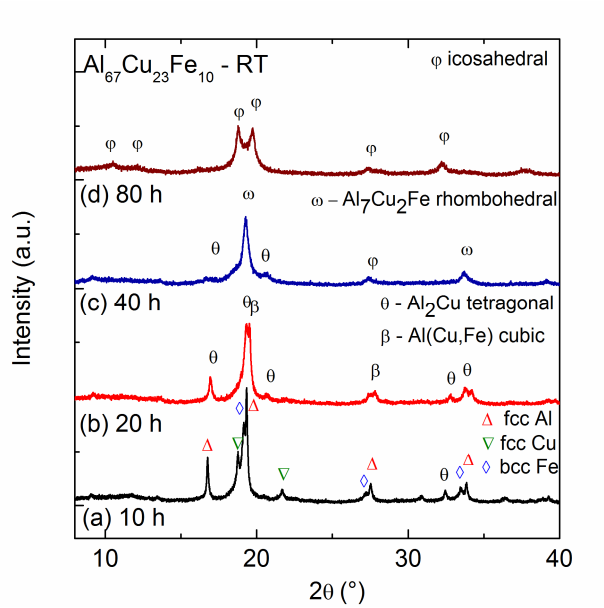

Figure 4. 8 X-ray diffraction patterns (HASYLAB/beamline B2, λ = 0.65125Å) of the as-milled $Al_{67}Cu_{23}Fe_{10}$ powders after (a) 10, (b) 20, (c) 40 and (d) 80 h of milling.

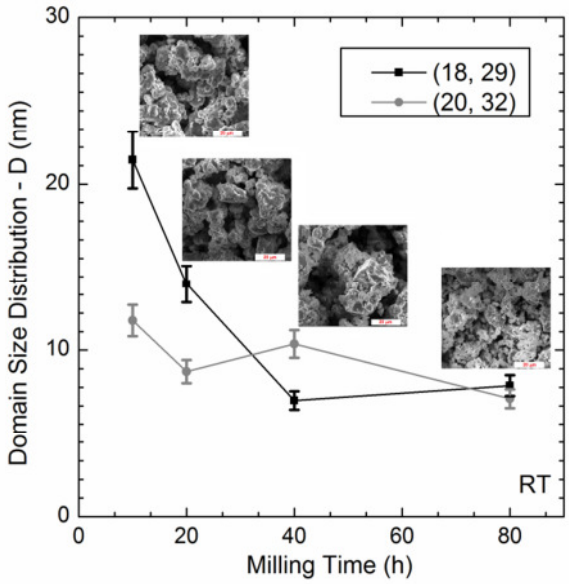

Figure 4. 9 Average domain-sizes evaluated using the Scherrer equation along the (18, 29) direction and (20, 32) direction *versus* milling time. (HASYLAB/beamline B2, λ = 0.65125 Å).

As can be seen, the initially sharp diffraction lines broaden significantly during milling and decrease in intensity. This is due to finite size broadening and atomic-level strain broadening. To separate these two effects, the full width at half maximum (FWHM) of the Bragg peaks as a function of the diffraction angle was analyzed. The size broadening profile was approximated by a Cauchy function and the strain broadening profile by a Gaussian function.

The effect of milling time on the domain size distribution (D) of the $Al_{67}Cu_{23}Fe_{10}$ powders is shown in Figure 4. 9. Scherer method was used to calculate the domain size distribution for the

icosahedral (18, 29) and (20, 32) main reflections. The experiments were performed using synchrotron radiation at the B2 beamline in HASYLAB. The positions of the X-ray diffraction peaks were determined by fitting them to lorentzian functions, and a similar procedure was followed for diffraction peaks from fine lanthan-hexaboride (NIST 660a, LaB_6). X-ray diffraction line broadening was used to determine changes in the average grain sizes distributions in the ball-milled materials before and during heat treatment. Approximate corrections for instrumental broadening were performed by subtracting from the measured peak width a width determined from a lorentzian fit of a nearby peak in the diffraction pattern from the reference (LaB_6) sample. During milling for 10 hours, the grain size of the elemental Al, Cu and Fe powders decreases to the nanometer scale (21 nm). Our results indicate however, that the binary alloy formation occurs when the grain sizes are in the range of 8–16 nm, which corresponds to a milling time of 20 hours. After 40 hours ternary alloy are present which translates into a smaller domain size of 7–12 nm. An increase up to 80 hours in the milling time leads to almost no further change of the domain size. This means that the condition of steady state processing is achieved already after 40 hours of MA The structural refinement continues however and the ternary Al_7Cu_2Fe rhombohedral phase transforms into a QC with $Al_{67}Cu_{23}Fe_{10}$ alloy composition.

4.3 The sequence of phase transformations during heating in $Al_{67}Cu_{23}Fe_{10}$ alloys

The performed investigations have revealed that the $Al_{67}Cu_{23}Fe_{10}$ composition is optimum for producing the quasicrystalline phase by mechanical alloying. This composition was used to thoroughly investigate the formation of the single-phase quasicrystalline structure.

The in-situ measured XRD patterns showing the change in the phase composition during heating are presented in Figure 4. 10.

The samples milled for 10 and 20 hours show similar evolution of the structure in the early stages of heating. As can be seen in the selected patterns for both cases (Figure 4. 11), the initial peaks of aluminum, becomes weaker and broads quickly after 200°C, while those of Fe and Cu do not change so fast. This indicates that the amount of aluminum decreases and aluminum dissolves into iron and copper, so that supersaturated solid solutions of metastable binary Al(Cu, Fe) alloys are formed. These intermetallic constituents are formed in the 40

hours milled sample already during MA but as a disordered bcc Al(Cu, Fe) intermetallic. This phase composition transforms into a primitive cubic structure during heating and it is present until around 400°C. At higher temperatures (300 – 500°C) the ternary intermetallic ω-Al_7Cu_2Fe compound forms, which is a stable phase in the concentration range close to the $Al_{67}Cu_{23}Fe_{10}$ composition. The ω-Al_7Cu_2Fe alloy is the main precursor of the icosahedral quasicrystalline φ-phase. The process of QC phase formation starts at temperatures higher than 550°C for 10 and 20 hours of milling and 520°C for 40 hours of milling.

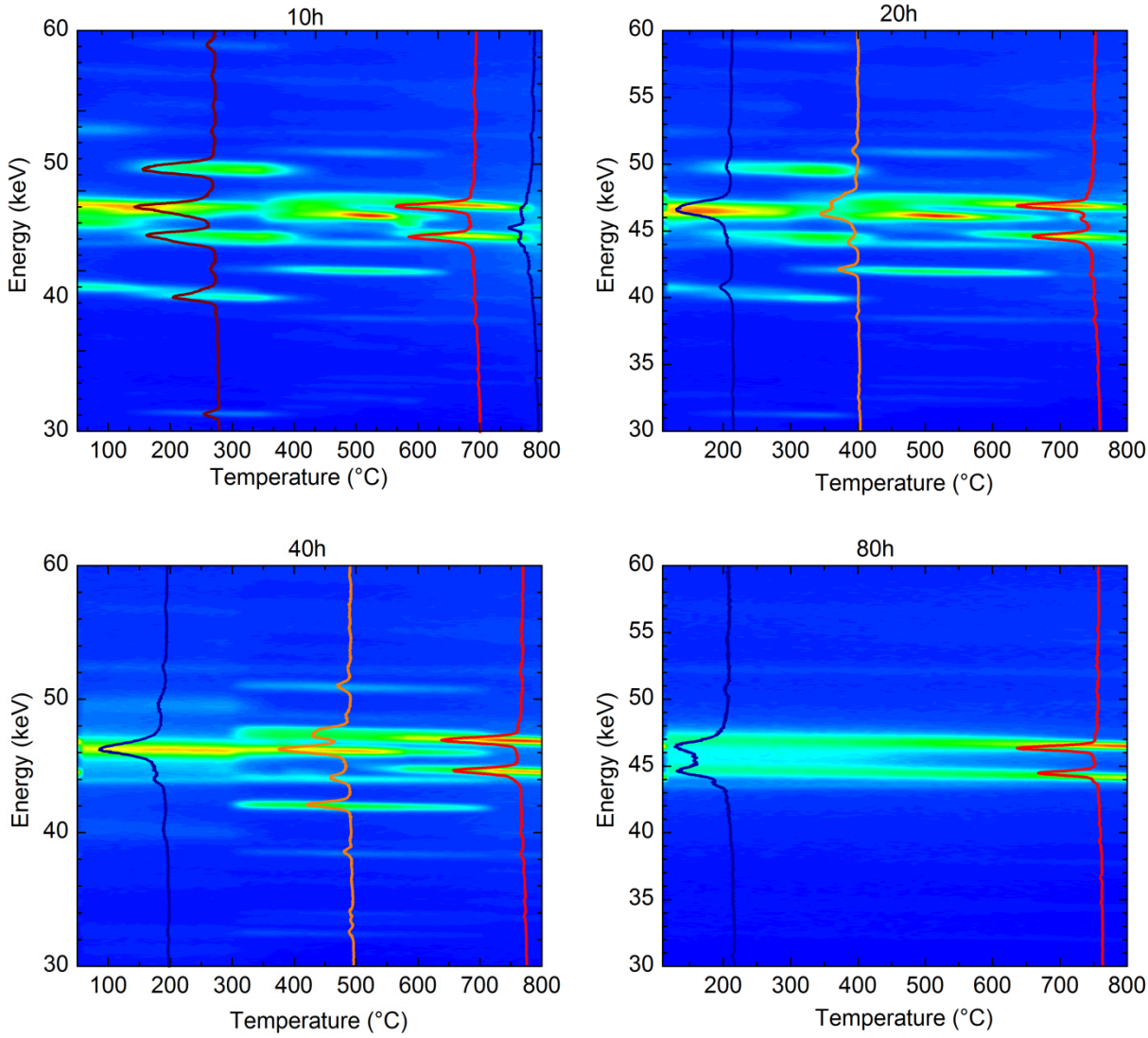

Figure 4. 10 In-situ EDXRD diffractograms showing the phase evolution during heating of the Al67Cu23Fe10 powders milled for 10, 20, 40 and 80 hours.

At the temperatures 650 – 750°C (sample milled for 10 h), higher than 690°C (sample milled for 20 h) and over 720°C (sample milled for 40 h) only quasicrystalline phase pattern was identified by in-situ X-ray diffraction. The exact temperatures and stability ranges is depicted in Figure 4. 12.

The 80 hours milled sample shows only quasicrystalline peaks which are relatively small in intensity at the beginning. During the heat treatment, a considerable increase in the structural perfection of the icosahedral phase occurs which is observed by both a perfectioning in the peak positions and a narrowing in the peak widths of the X-ray powder diffraction spectra (Figure 4. 11). Also an increase in the peak intensity can be seen which is mostly because of the increase in the crystallite size from 8 ± 2 nm up to 85 ± 20 nm as seen in Figure 4. 13a.

Both the partial ordering of the Al(Cu, Fe) intermetallic after 40 hours of milling and the formation of single icosahedral φ-phase after 80 hours of milling indicate that a longer processing time increases the processing temperature, which induces a thermal relaxation of the long range ordered quasicrystalline structure.

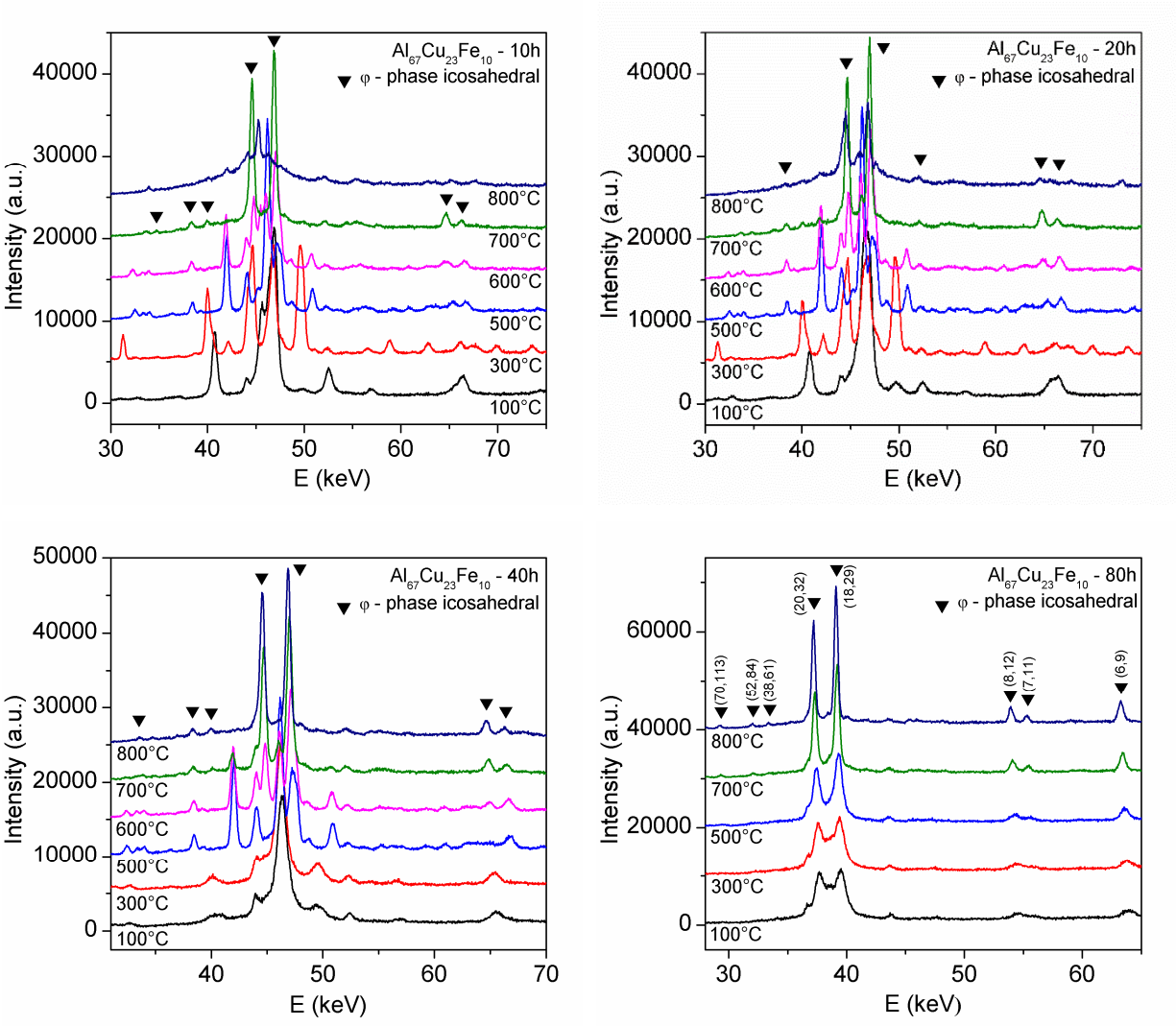

Figure 4. 11 Selected EDXRD patterns (HASYLAB/F2.1) of the Al67Cu23Fe10 powders milled for 10, 20, 40 and 80 hours at different temperatures.

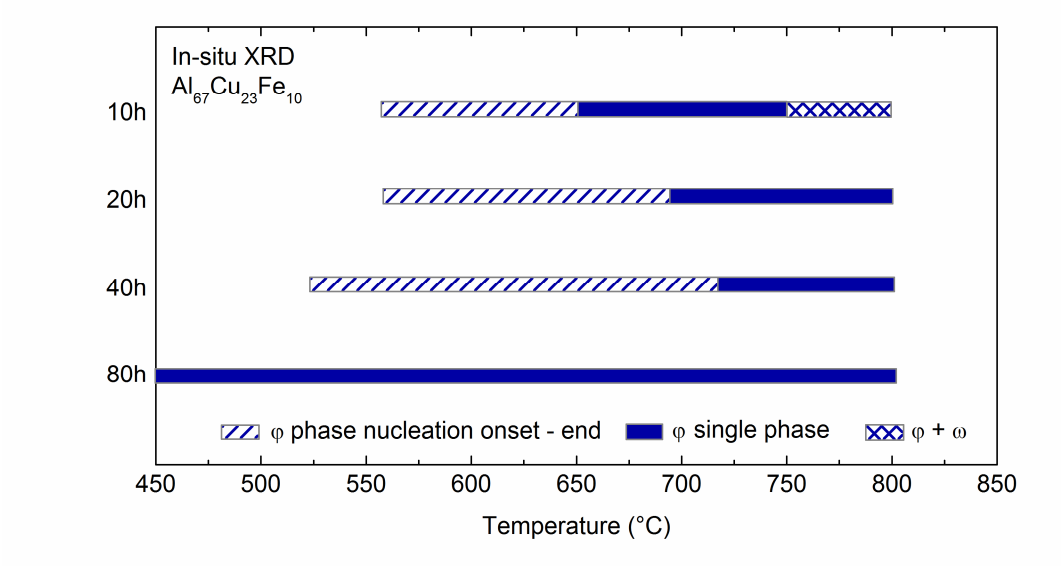

Figure 4. 12 Transformation temperatures for the icosahedral transition in nanostructured Al-Cu-Fe alloys as determined by HT-XRD experiments (uncertainty ≈ 20°C).

A preliminary analysis of the grain-size evolution during continuous heating was performed using the normal grain growth model. Figure 4. 13 (a) shows the general tendency of the domain size increase with the temperature. For simplicity, only the results along the (18, 29) direction and (20, 32) direction are presented here. The crystallite size measured for the other reflections showed the same tendencies. For the samples milled for 10 and 20 hours, the domain size increases continuously with the temperature. The samples milled for 40 and 80 hours show rather a plateau in the domain size until 400°C and 500°C, respectively. After this temperature a sudden jump from 7-9 nm up to ~ 50 nm at 600°C, followed by a continued increase to 80 – 90 nm at 800°C is to be seen. The in-situ XRD pattern of a 10 hours milled sample shown in Figure 4. 13b exemplifies the increase of the peak intensity and decrease of the peak broadening with temperature.

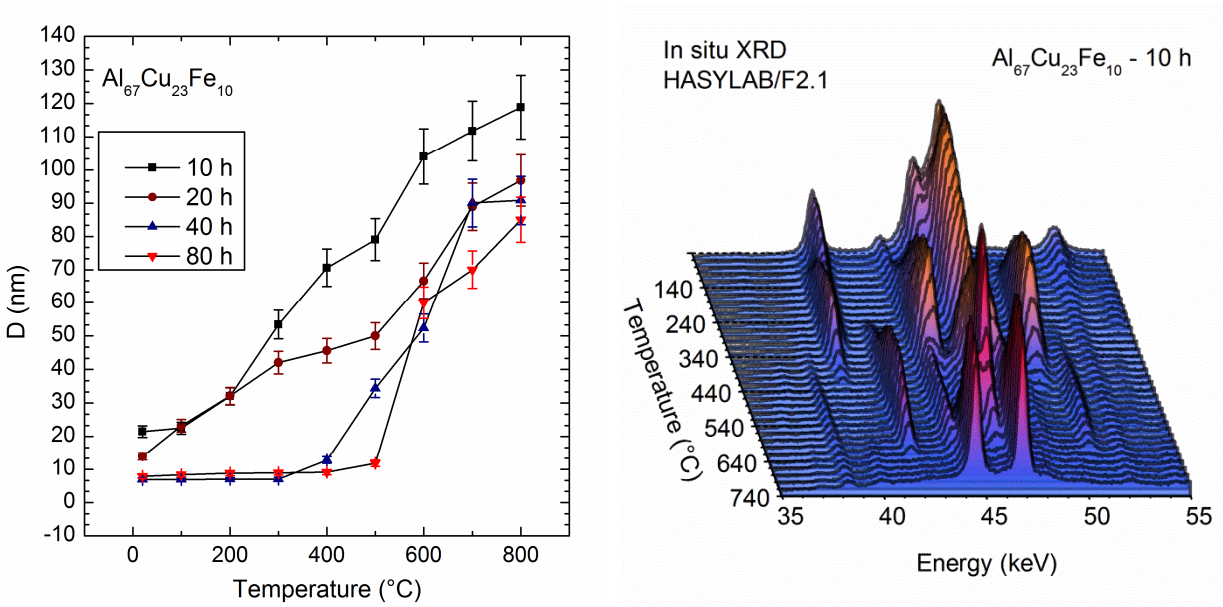

(a) **(b)**

Figure 4. 13 (a) Effect of the heating temperature on the average domain-sizes of $Al_{67}Cu_{23}Fe_{10}$ alloys milled for 10, 20, 40 and 80 hours, evaluated using the Scherrer equation along the (18, 29) direction and (20, 32) direction. (HASYLAB/DESY, beamline B2, $\lambda = 0.65125$ Å) (b) In-situ XRD pattern of an $Al_{67}Cu_{23}Fe_{10}$ alloys milled for 10 h showing the change in the intensity and line broadening of the peaks with temperature.

The mechanochemical interactions in the vicinity of the quasicrystalline region in Al-Cu-Fe can be expressed by the equation in Figure 4. 14.

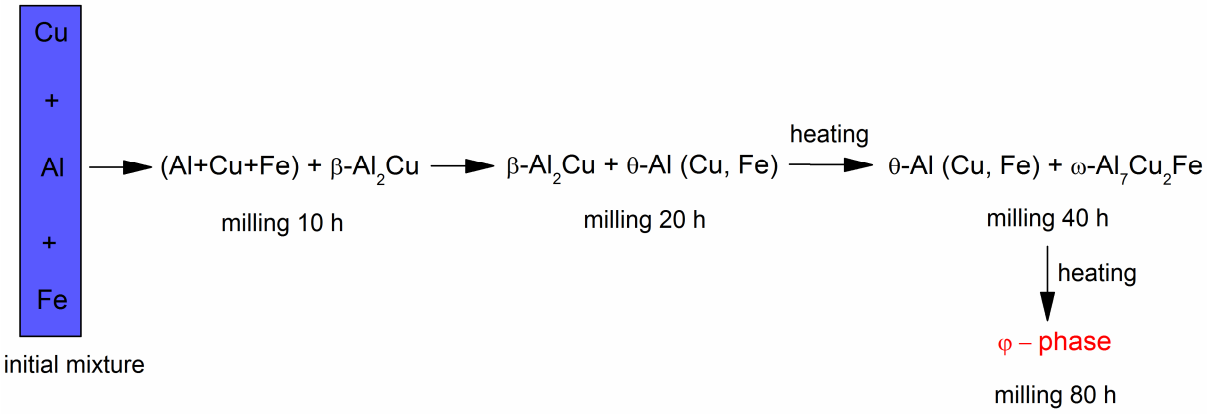

Figure 4. 14 Schematic of the phase evolution during milling and subsequent heating of mechanically alloyed $Al_{67}Cu_{23}Fe_{10}$ composition. It shows the QC phase formation takes place either during heating the as-milled powders or directly during MA at longer milling times. This can be a consequence of an increase of the temperature during the milling process, which induces a thermal relaxation of the atomic structure.

The DSC traces of the milled alloy are shown in Figure 4. 15. The DSC measurements were performed for powder ball milled $Al_{67}Cu_{23}Fe_{10}$ alloys using heating rates of 5, 10, 15 and 20 $K \cdot min^{-1}$. The thermal evolution of the crystalline phases is similar for the alloys milled for 10 and 20 h. Below 500 °C several exothermic solid-state processes related to the crystallization and chemical reactions of the elemental components can be distinguished. At about 100 °C starts a shallow and broad peak (1) which is typical for relaxation processes. A crystallization peak at about 300 °C (2) is then followed by a sharp main exothermic peak at 400 °C (3). In the second part of the scan the sample exhibits decreasing heat evolution, which is due to the grain growth of some quantities of the crystalline phases already present in the powder. Between 550 – 750°C many overlapped exothermic and endothermic peaks are observed. This implies that at least three thermal effects of different natures may be involved. These events are smaller and separated at β = 5 K/min, they grow and become wider at β = 10 and 15 K/min, being completely overlapped at β = 20 K/min. At this heating rate they appear like one big exothermic reaction. It is to be noted that the characteristic temperature, T_m, of maximum heat flow shifted to higher temperatures for higher heating rates. The exothermal reactions correspond to the complete diffusion of the binary compounds into the ternary ω-phase followed by icosahedral phase formation and grain growth. The endothermic peaks are probably related to melting processes.

The alloy milled for 40 hours (Figure 4. 15 c) shows no thermal event below 300°C. This is probably because the system already reached a certain degree of thermal relaxation during milling. The first thermal event is the crystallization peak at 300°C which is the same as peak number (2) in the 10 and 20 hours milled samples. The main exothermic peak at ~ 400°C (3) seen in the first two samples can also be seen here, but has the same intensity as the previous one. The main exothermic events here can be seen in the temperature range from 550 – 750°C.

Figure 4. 15(d) shows the DSC behavior of the alloy milled for 80 hours. As expected, no thermal events are to be seen until 550°C. The DSC curve confirms the XRD results showing that the single QC phase is formed directly during MA. The exothermal peak seen after 550°C at β = 5 and 10 K/min is exclusively related to grain growth process. However, at a faster heating rate (β = 15 and 20 K/min) a second exothermal event can be noticed here at ~ 750°C. Based on the XRD spectra taken after the DSC process (Figure 4. 16), we assume this is a sign of destabilization of the φ-phase and its transformation into the binary Al(Cu, Fe) phase with a partially ordered cubic structure. Besides, the relative intensity of the two main QC

peaks (18, 29) and (20, 32) is opposite that for the primitive icosahedral peaks produced by milling and heating with 5 or 10 K/min.

The cooling curve reveals that the phase transformations leading to binary Al-based compounds are irreversible which implies that none of these intermediate binary phases would be formed on fast solidification. However, one can see at least one exothermic event which we assume corresponds to the formation of the ω-phase during slow cooling. Indeed, the XRD spectrum taken after DSC treatment clearly shows a decrease on the peak intensity of the ω-phase with the cooling rate. So we conclude that increasing the cooling rate this peak will completely disappear.

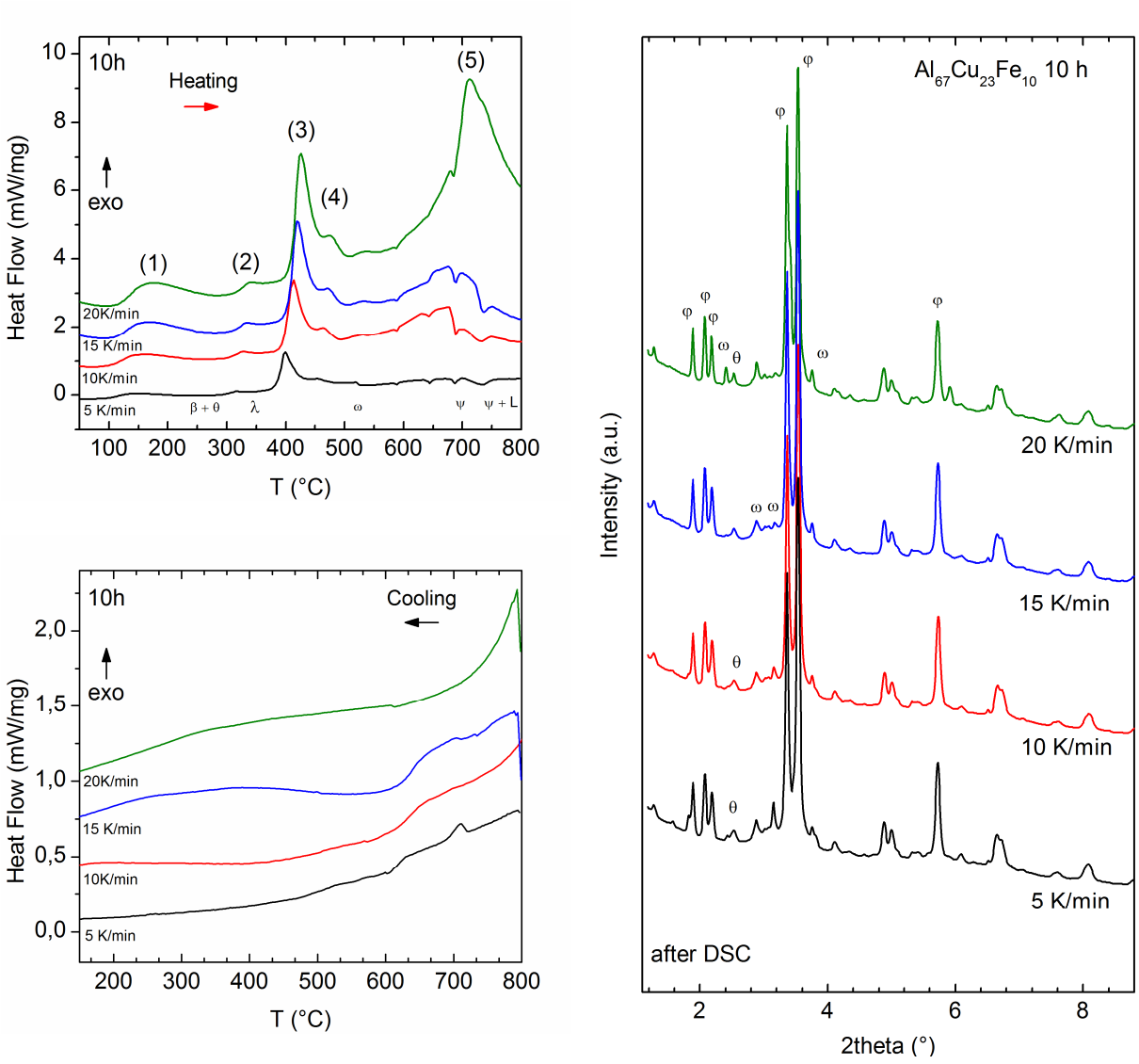

(a) DSC (left) and XRD (right) of $Al_{67}Cu_{23}Fe_{10}$ alloy milled for 10 hours.

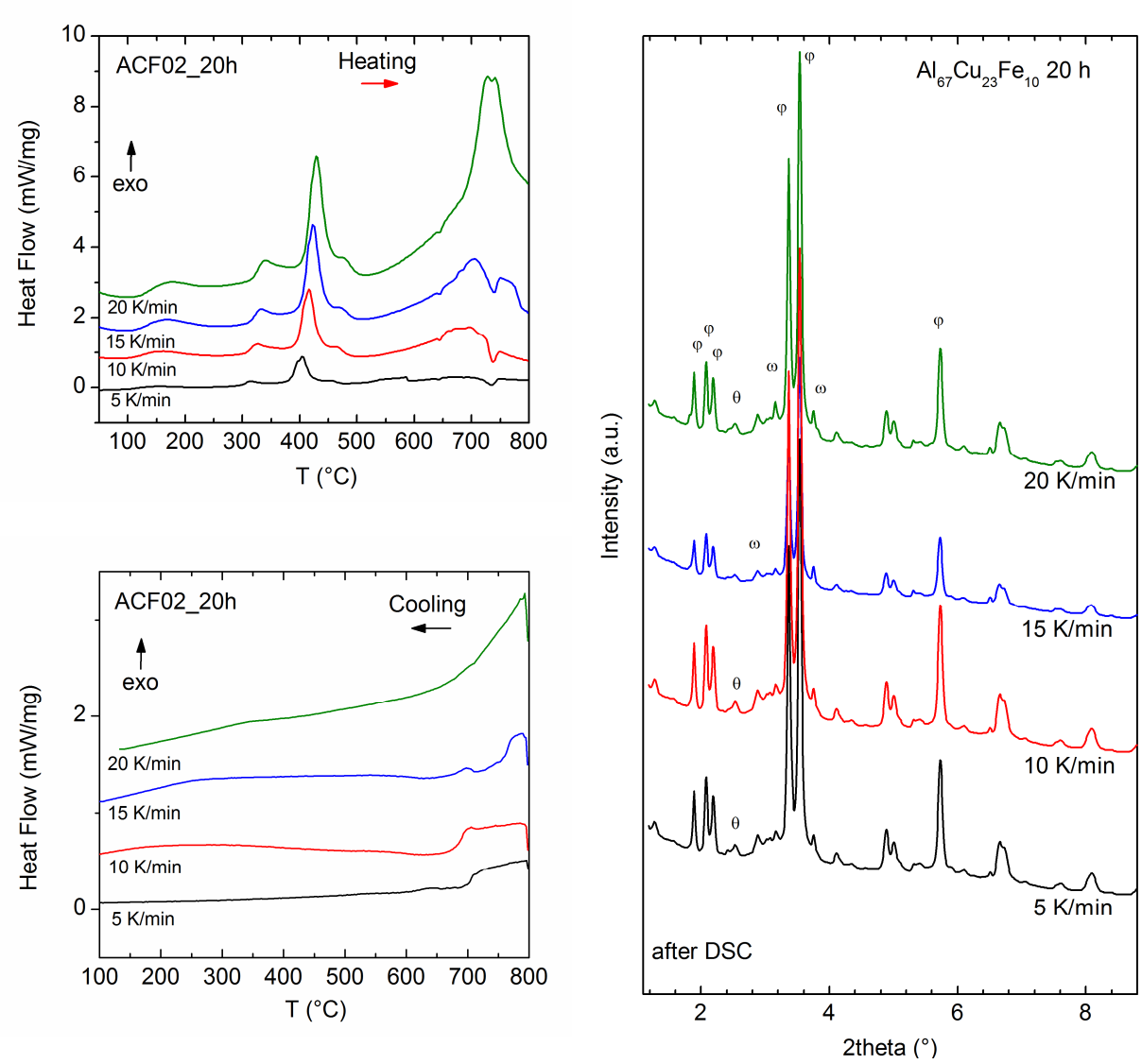

(b) DSC (left) and XRD (right) of $Al_{67}Cu_{23}Fe_{10}$ alloy milled for 20 hours.

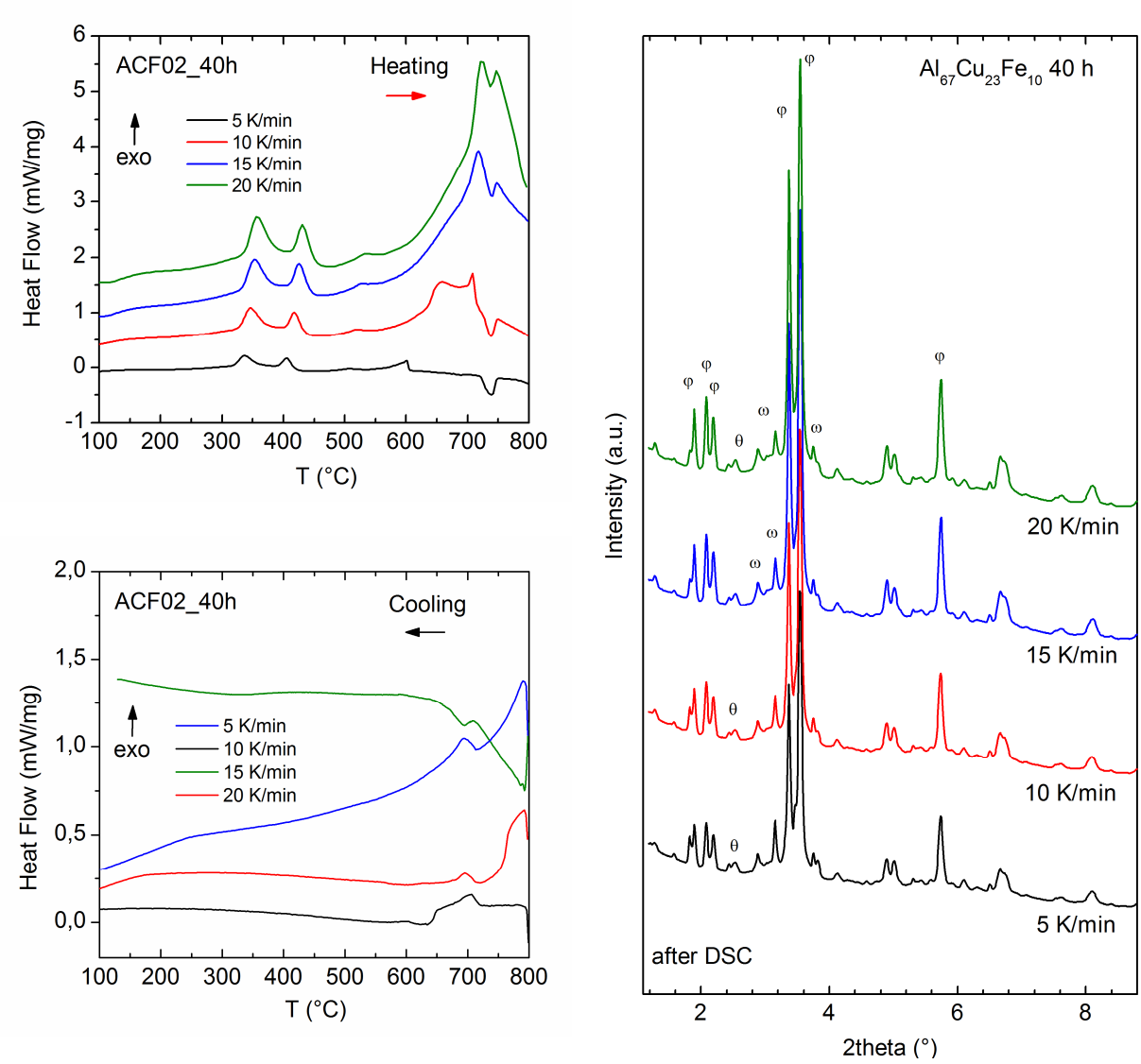

(c) DSC (left) and XRD (right) of $Al_{67}Cu_{23}Fe_{10}$ alloy milled for 40 hours.

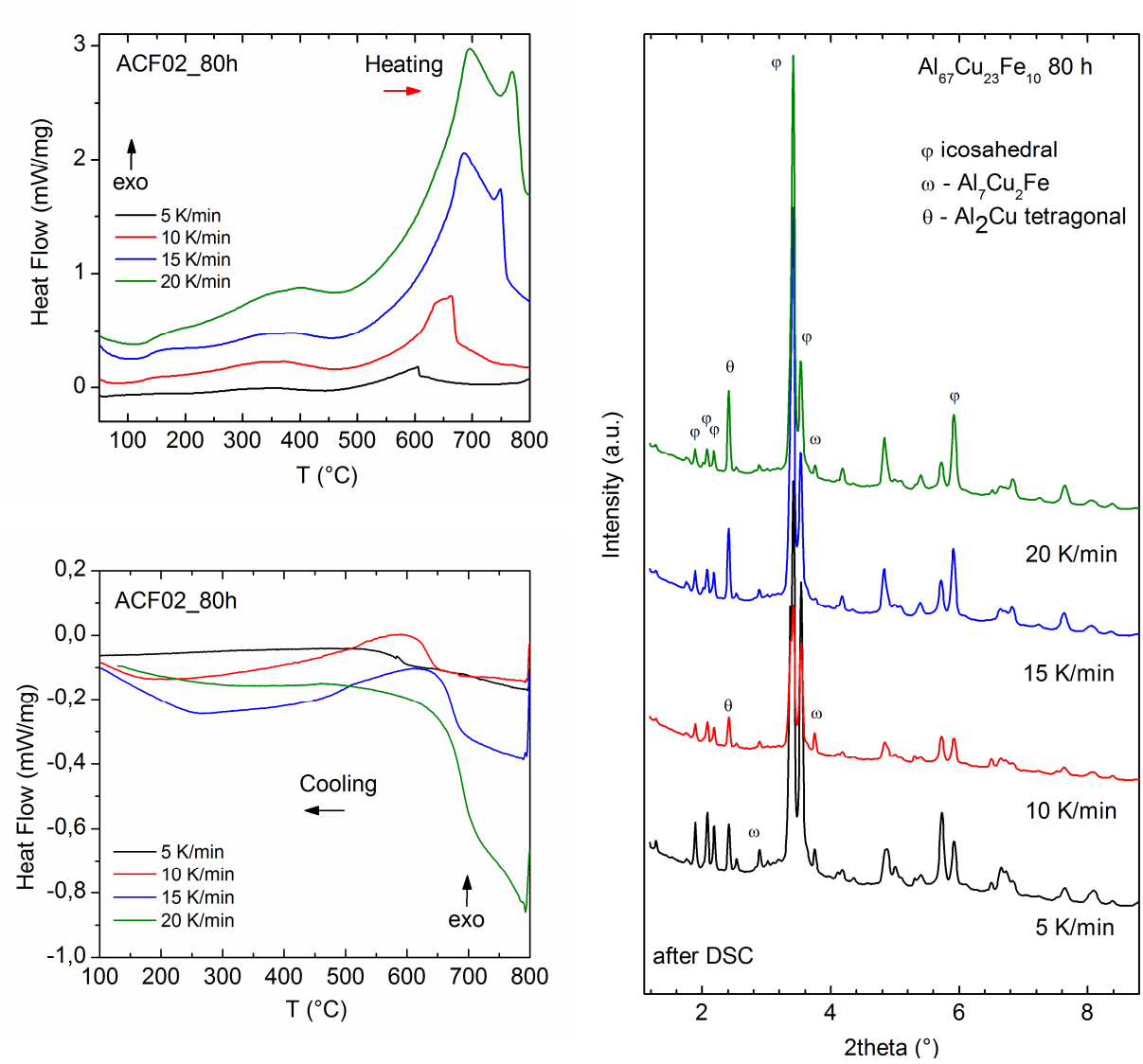

(d) DSC (left) and XRD (right) of $Al_{67}Cu_{23}Fe_{10}$ alloy milled for 80 hours

Figure 4. 15 The DSC heating and cooling curves performed at β = 5, 10, 15 and 20K/min, after MA of $Al_{67}Cu_{23}Fe_{10}$ alloy milled for (a) 10 hours, (b) 20 hours, (c) 40 hours and (d) 80 hours.

Figure 4. 16 XRD patterns taken after DSC cooling process (HASYLAB/beamline BW5, λ = 0.1239Å) of $Al_{67}Cu_{23}Fe_{10}$ alloy milled for (a) 10 hours, (b) 20 hours, (c) 40 hours and (d) 80 hours.

The Kissinger plots $\ln(\beta/T_p^2)$ versus $1/T_p$ are shown in Figure 4. 17. Based on the slope of the Kissinger plot, when the rate constant is fitted to the Arrhenius expression, a negative value of activation energy (E_a) will result. The activation energy is obtained from the Kissinger equation:

$$\ln\left(\frac{\beta}{T_p^2}\right) = Const. - E_a/RT_p \qquad (4.1)$$

The value of the E_a for the φ-phase transformation is calculated to be: ~ – 26 kJ/mol for $Al_{67}Cu_{23}Fe_{10}$ alloys milled for 10 h, – 20 kJ/mol for 20 h and – 23 kJ/mol for 40 h. This

means the rate of reaction decreases with increasing temperature which translates into energy release. The transformations exhibiting negative activation energies are typically barrierless reactions, suggesting that the formation of the icosahedral phase is energetically favored. The thermal effect determined in the 80 hours milled sample is – 86 kJ/mol. Since the QC phase is already present as a single phase after milling, this thermal effect corresponds to the formation of a more stable modification of the QC phase. Also the sudden grain growth registered after 500°C for the 80 h milled powders, contributes to this exothermal effect. The more structurally stable φ-phase modification is already formed at 500°C after 80 hours of milling.

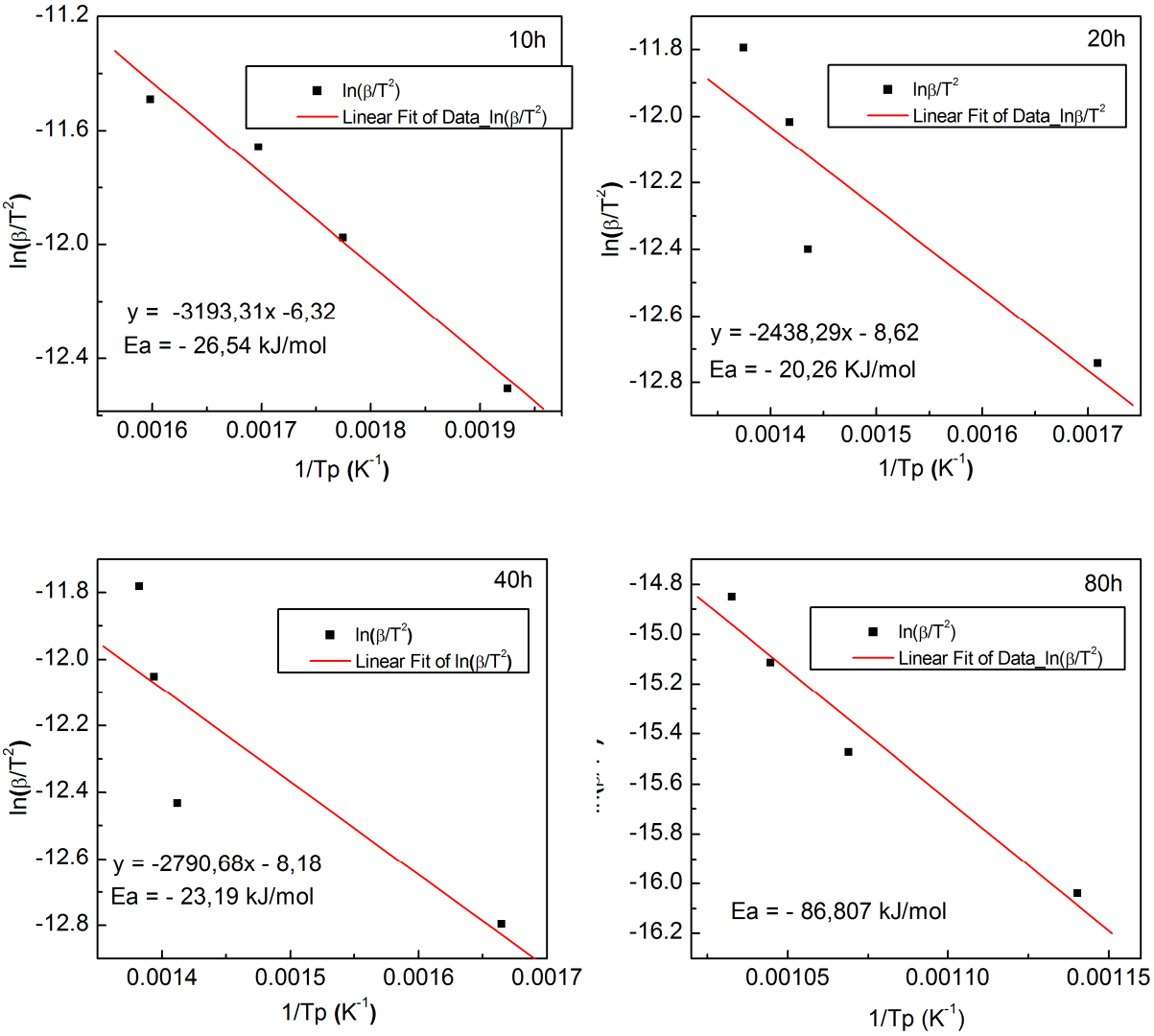

Figure 4. 17 Kissinger plots of QC phase formation in $Al_{67}Cu_{23}Fe_{10}$ alloys. The linear regression of experimental data yields $E_a = -26$ kJ·mol^{-1} (for milling time of 10 h), $E_a = -20 \pm$ kJ·mol^{-1} (20 h), $E_a = -23$ kJ·mol^{-1} (40 h) and $E_a = -86$ kJ·mol^{-1}.

Comparing the DSC curves (Figure 4. 15) with the phase evolution diagrams (Figure 4. 10) one can see that is not so trivial to associate the observed DSC maximum with any particular phase transformation using the XRD data only. Each DSC maximum corresponds to a simultaneous progress of more than one phase transformation. In fact, these DSC peaks reflect the relative maximums of solid-state reactions total rate.

The formation of ternary QC alloys is accompanied by a pronounced thermal effect. The total exothermal effects determined from the DSC curves were between – 26 kJ/mol and – 20 kJ/mol for $Al_{67}Cu_{23}Fe_{10}$ alloys milled from 10 – 40 h. These values are in good accordance with data reported by other authors [166]. The thermal effect determined for the 80 hours milled sample was – 86 kJ/mol. At the same time the characters of interaction in corresponding binary systems are essentially different. As mentioned before, the Al-Cu and Al-Fe systems are characterized by negative heats of intermetallic compounds formation whereas the Fe-Cu system possesses significant positive heat of mixing. The forces of repulsion between Cu and Fe have a pronounced effect on the elements distributions over the phases during the transformations caused by heating and also by a longer milling processing. The aluminum-based intermetallics formed at the initial stage of mixing are enriched either with Cu or with Fe, these elements are separated as long as possible. Upon further heating, the chemical composition of the coexisting phases gradually approaches the average composition of the alloy. Increasing the heating rate leads to a shift in the formation temperature accompanied by an increase in the exothermal effect. The chemical composition of the Al_7Cu_2Fe ω-phase is similar to the composition of the $Al_{67}Cu_{23}Fe_{10}$ φ-phase. It has been shown that the cooling rate plays an important role on freezing the φ-phase structure at high temperature. Too slow cooling can result into formation of a secondary ω-phase, although it is worth to mention that the QC phase still remains the main volume fraction even after slow cooling with 5 K/min.

We found that the direct preparation of single QC phase by mechanical alloying is possible during the use of long-term intensive treatments. However, the quasicrystalline structure formed directly through MA is characterized by structural disordering and transforms upon heating into a more stable modification already at 500°C.

4.4 Quasicrystalline phase formation during sintering of $Al_{67}Cu_{23}Fe_{10}$ alloys

4.4.1 Microwave sintering (MW)

After we investigated the effect of the MA processing conditions on the formation of stable QC phase during continuous heating, we concluded that a fast cooling is an important factor which contributes to the preservation of the pure QC phase. It is possible to apply the advantages of microwave processing with its volumetric heating and according time and energy savings to the synthesis of icosahedral Al-Cu-Fe systems. We compare these results with in-situ time resolved monitoring of solid state transformations during non-isothermal heating of the powders in order to evaluate the use of inductive microwave heating for the synthesis of quasicrystalline Al-Cu-Fe.

For microwave experiments the $Al_{67}Cu_{23}Fe_{10}$ pellets with a density of 3,25 $g \cdot cm^{-3}$ were heated up to different maximum temperatures in the microwave resonator with similar heating rates and constant input power, in order to reproduce the temperature sequence of the in-situ X-ray diffraction experiments (Figure 4. 19). The subsequent fast cooling was achieved only by thermal losses of the samples.

The microwave heating processes (see Figure 4. 18) provides reproducible time dependencies for the sample temperature and absorbed microwave power. The step-like changes of the absorbed microwave power as well as the variations in the heating rates directly indicate phase changes in the sample during microwave heating. These thermal events are in good agreement with the DSC and XRD already discussed in the previous section. Therefore we assume that microwave heating in the magnetic field anti-node features the same thermal events as conventional heating for comparable heating rates.

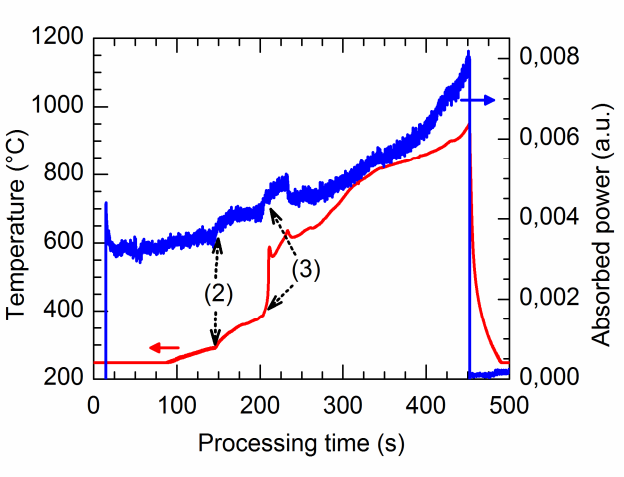

Figure 4. 18 Typical microwave heating process of a $Al_{67}Cu_{23}Fe_{10}$ pellet at constant input power. Both, the absorbed microwave power (blue) and the temperature profile (red) feature various thermal events. Fast cooling (> 50 K s^{-1}) between 950 °C and 500 °C starts immediately after microwave switch-off.

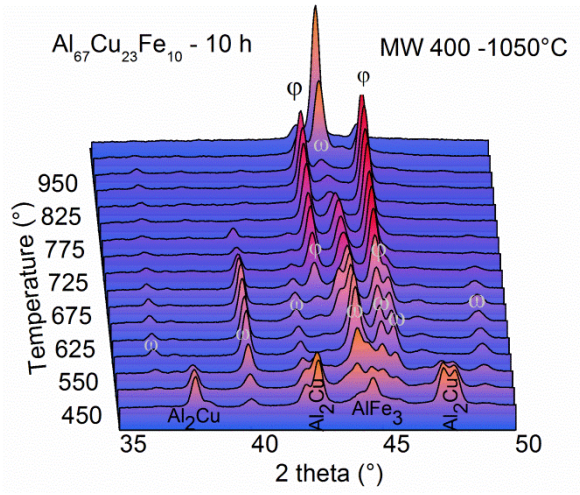

Figure 4. 19 XRD spectra (taken ex-situ) showing the phase evolution of the system during continuous microwave heating.

Especially the dominant exothermic peak (3) leads to a strong increase in the heating rate at approximately 400 °C. The further increase in absorbed power and temperature above 800 °C can be assigned to melting and degradation processes of the alloy system and a corresponding change in microwave absorbance. We previously discussed the importance of the fast cooling on the preservation of the QC phase. So we chose the microwave processing for its main advantage in contrast to conventional heating which is the relatively fast cooling of the sample after power switch-off. Without special efforts cooling rates of over 50 K·s^{-1} are possible only from thermal losses which were maximized by an increase in the surface to volume ratio of the pellets.

The in-situ XRD measurements were further compared to the ex-situ XRD spectra taken for the fast cooled pellets from microwave processing. Figure 4. 20 shows the XRD patterns for different pellets of the same weight, diameter and composition, heated up in the microwave cavity to different maximum temperatures, after fast cooling back to room temperature. The quasicrystalline phase is observable after microwave processing up to 800 °C but not as a single phase, because traces of ω-phase are also present. The XRD spectra in Figure 4. 20 are point-wise measurements along the sample surface which reveal however, the presence of pure icosahedral φ-phase in the middle of the pellet and a mixing of φ and ω-phases at both edges. This can be explained by the inverse temperature gradient during microwave

processing. The shift of the transition temperatures is due to the different heating rates during conventional and microwave heating influence the observed phase kinetics.

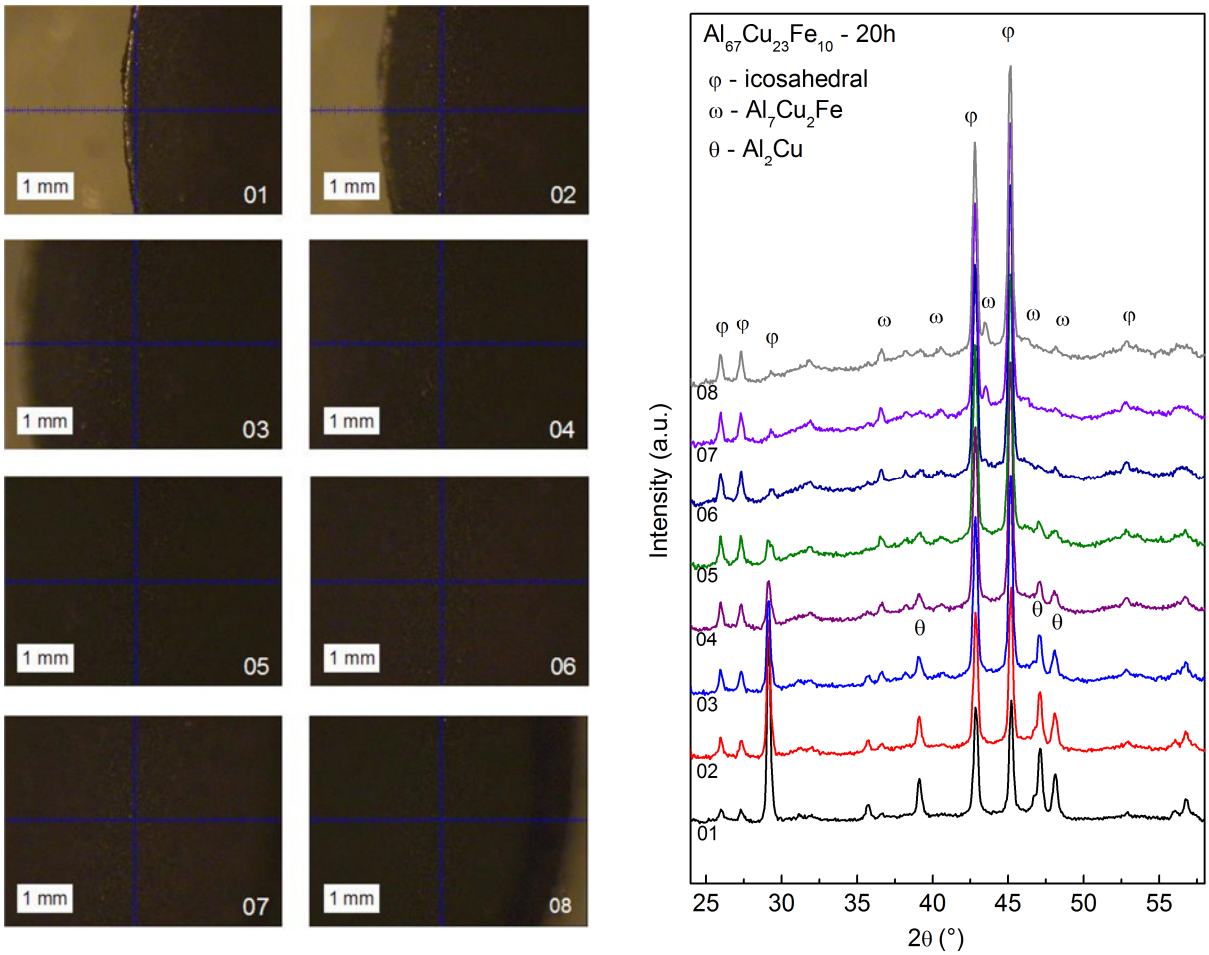

Figure 4. 20 XRD patterns taken on 8 different spots of a 5 mm microwave sintered pellet at 800°C (λ = 1.54184 Å). The corresponding pictures with the position of the 8 spots on the 5 mm pellet are shown on the left side: 01 (0 mm), 02 (1 mm), 03 (1.5 mm), 04 (2 mm), 05 (2.5 mm), 06 (3 mm), 07 (3,5 mm) and 08 (4,5 mm).

When compared with the as-pressed sample, microwave sintering resulted in a densification increase from 3.25 g·cm^{-3} to 3.93 g·cm^{-3}. Figure 4. 21 depict images with the microstructures of both as-pressed and microwave processed alloy. The as-pressed pellet possesses non-uniformly distributed grains, with large angular pores, while the microwave heated sample exhibits finer, more uniform morphology and smaller pore size. This is due to the grain growth restriction by short microwave-time processing and it can be associated with the improvement in density of the sample. Meanwhile, microwave sintering leads to finer microstructure and pore size, which is associated with the improvement in the sample's density.

The hardness is independent from the pores shape however it is determined by the special atomic arrangement in the icosahedral quasicrystalline structure and the densification of the specimen. Thus, a higher hardness and Young's modulus was measured in the microwave heated sample compared to the as-pressed pellet by nanoindentation. The obtained values for hardness and Young's modulus in the as-pressed specimen are (1.8 ± 0.4) GPa and (40 ± 10) GPa, respectively, while in the microwave processed sample, hardness was found to be (6 ±2) GPa and the Young modulus to be (120 ± 30) GPa.

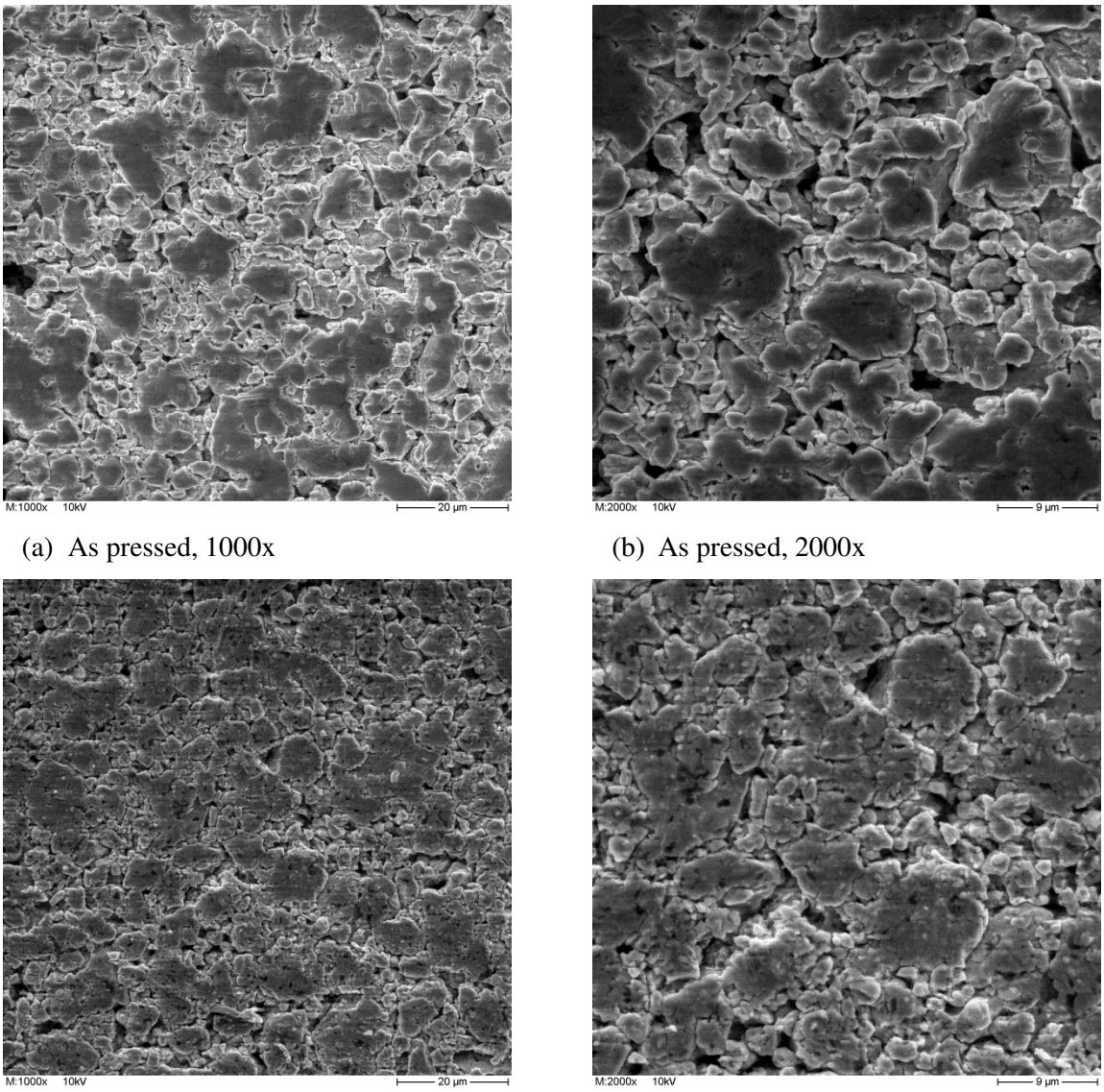

(a) As pressed, 1000x (b) As pressed, 2000x

(c) MW sintered, 1000x (d) MW sintered, 2000x

Figure 4. 21 SEM micrographs taken on the $Al_{67}Cu_{23}Fe_{10}$ pellets (a, b) as pressed, (c, d) microwave sintered at 800°C.

Microwave heating in the magnetic field anti-node was used to obtain quasicrystalline phase at atmospheric pressure and normal environment combined subsequent ultra-fast cooling to ambient temperatures. XRD analysis was carried out to identify the main constituents after

microwave processing, at room temperature. The change in the heating rate causes a shift in the transition temperatures, but the evolution of the constituent phases with the temperature remains almost the same as during conventional heating. Note that a comparison between in-situ synchrotron analyses with ex-situ X-ray diffraction of the microwave heated samples is possible, due to the available ultra-fast cooling rate that freezes the solid state transformations. The microwave processed sample showed a smaller porosity, consisting of very small, relatively rounded and more uniformly distributed pores, as against the as-pressed pellets which showed a bigger porosity, mainly consisting of large, angular and non-uniform distributed pores.

The improved mechanical properties of the microwave processed sample may be attributed to the smaller porosity in comparison to the as-pressed specimen, in addition to the effect of higher density observed.

4.4.2 Spark plasma sintering (SPS)

We discussed in the previous sections that heating and cooling rate plays an important role for the formation of a single quasicrystalline phase. Indeed, a slow rate of solidification leads to formation of macrosegregates which are very difficult to eliminate even after long thermal treatments. On the contrary, the fast solidification freezes the structural state at a high temperature, where the chemical segregation is smaller. This way, the thermodynamical equilibrium can be reached faster by an annealing process, during which the metastable phases will be dissolved and the single icosahedral phase will be formed. The densification, phase transformation/reaction and grain growth processes are most often observed to occur simultaneously during conventional sintering of materials, which implies that it is difficult to study the kinetics of each process separately. Using SPS, however, the densification process can be accomplished at such a low temperature that the kinetics of grain growth is retarded, and so are the phase transformation/reactions. Furthermore, the phase transformations/reactions can be accomplished before the grain growth process is initiated.

This therefore provides us with a unique opportunity to monitor the kinetics of densification, phase transformation/reactions and grain growth separately.

The Al-Cu-Fe milled powders were subsequently solidified by spark plasma sintering processing (SPS). Typical shrinkage data recorded during densification of an $Al_{67}Cu_{23}Fe_{10}$ alloy by SPS is given in Figure 4. 22. During SPS, the dimensional change (densification) of

the powder compact was automatically recorded by the displacement of the upper piston. It is seen that densification occurs mainly during the initial heating stage of the SPS process. The densification starts at 400°C and ends at 440°C when a constant heating rate of 40 $K \cdot min^{-1}$ and a compressive stress of 50 MPa were applied. The recorded maximum shrinkage rate is 4.26 $mm \cdot min^{-1}$ after only 1 minute (1). At least 4 displacements peaks (2) are registered in the next 4 minutes until 440°C which indicate phase transformations. This result is in good agreement with the DSC, XRD and MW presented in the previous sections. Full density and complete phase transformation was approached after holding at 800°C for 20 min. In the holding period another couple of displacement peaks (3) are registered which could be explained by melting and extensive particle rearrangement effected by enhanced grain boundary sliding. At the end of the SPS processing (4) the final elimination of closed pores and the growing of large elongated grains occur.

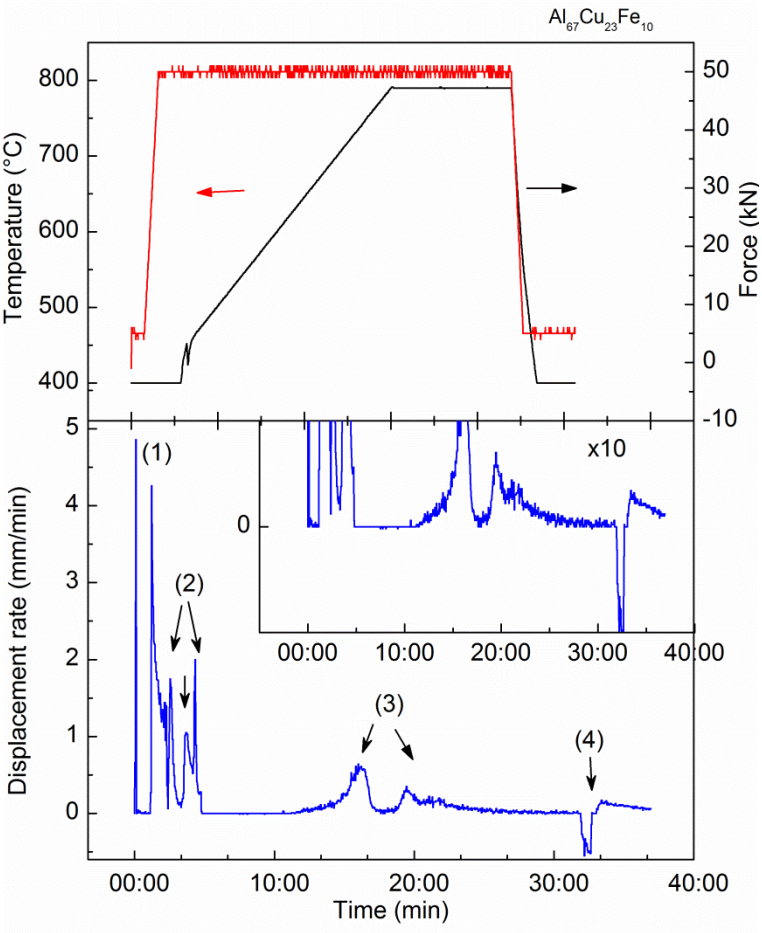

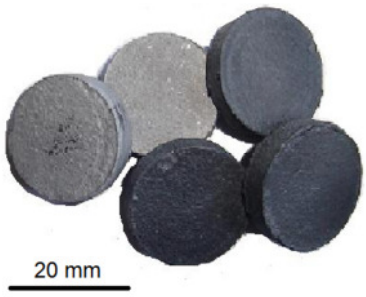

Photograph showing the Al-Cu-Fe pellets after SPS processing.

Figure 4. 22 The SPS sintering diagram of the as-milled $Al_{67}Cu_{23}Fe_{10}$ powder. During the initial stage, the powders are heated to 790°C at 40°C/min. The isothermal stage is defined by a dwell time of 20 min at the sintering temperature (790°C). The pressure applied was 50MPa at the sintering temperature.

The evolution of the microstructure during the sintering process is presented in Figure 4. 23. The average values of the grain sizes are plotted in Figure 4. 24. The grain sizes increases with sintering temperature.

The microstructures of the sample sintered at 800°C reveals the presence of elongated grains with the elongated direction perpendicular to the pressure direction, but also few large equiaxed grains. Neither pores nor macroscopic defects as cracks are visible. The rapid grain growth occurring at elevated temperatures, enhanced by prolonged dwelling, is a common phenomenon often observed during spark plasma sintering.

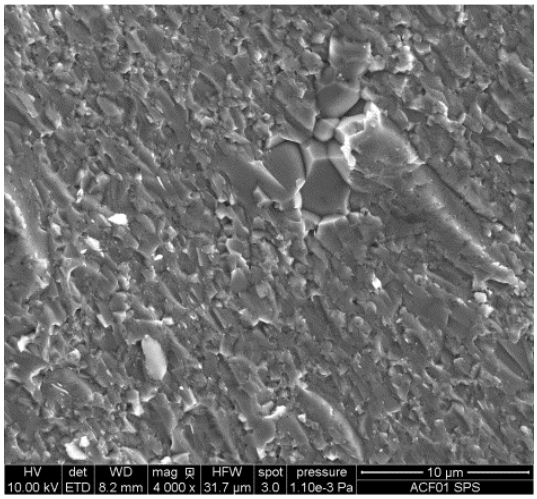

(a) $Al_{67}Cu_{23}Fe_{10}$, 800°C, 4000x

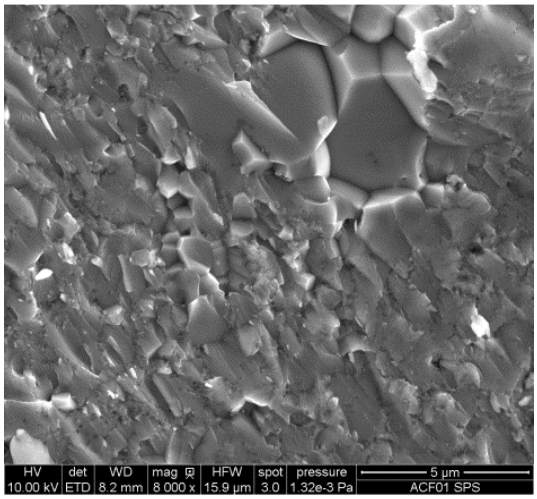

(b) $Al_{67}Cu_{23}Fe_{10}$, 800°C, 8000x

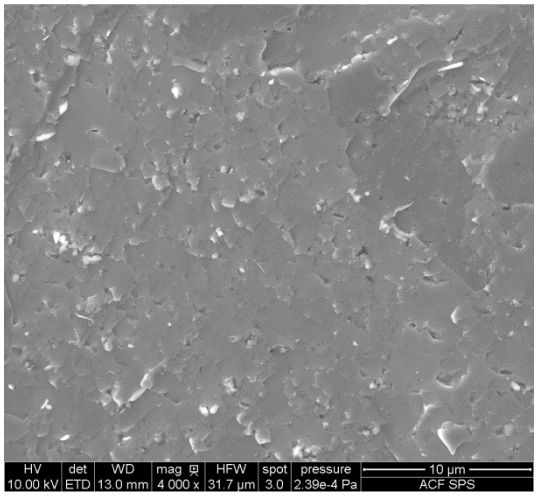

(c) $Al_{67}Cu_{23}Fe_{10}$, 790°C, 4000x

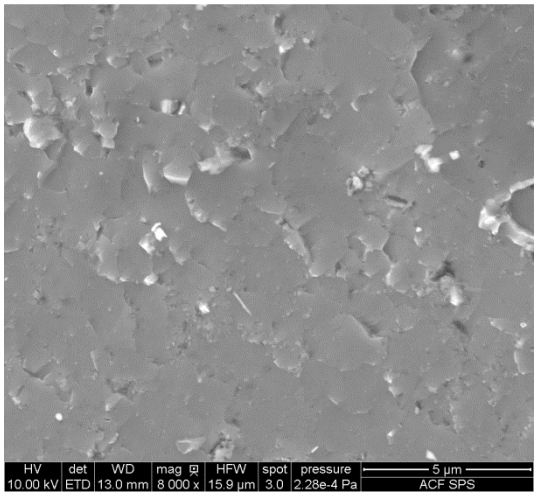

(d) $Al_{67}Cu_{23}Fe_{10}$, 790°C, 8000x

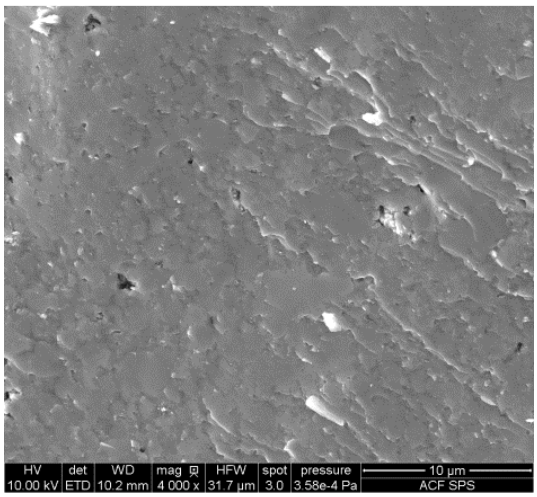

(e) $Al_{67}Cu_{23}Fe_{10}$, 780°C, 4000x

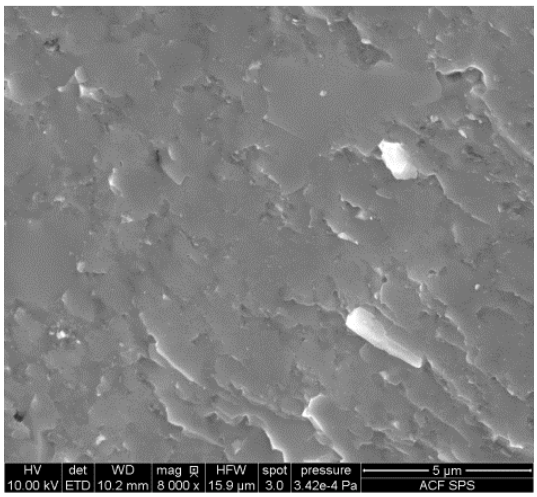

(f) $Al_{67}Cu_{23}Fe_{10}$, 780°C, 8000x

Figure 4. 23 SEM micrographs taken on the fracture surfaces of $Al_{67}Cu_{23}Fe_{10}$ pellet, revealing the microstructure development after SPSing using a heating rate of 20 $K \cdot min^{-1}$ with a constant pressure of 50MPa: (a), (b) both micron equiaxed grains and elongated grains obtained when a temperature of 800°C and a holding time of 25 min was applied; (c), (d) elongated grains formed at 790°C after 20 min holding time; (e), (f) elongated grains formed at 780°C after 20 min holding time.

Sintering of Al-Cu-Fe alloys is a complex process, during which grain growth takes place simultaneously with densification and phase transformation. Therefore, it is not an easy task to clarify the mechanisms determining the rate of grain growth, for example. However, it was possible to define a `kinetic window` during which it is possible to prepare dense samples and simultaneously avoid grain growth (see Figure 4. 24). Within 780-790°C densification is aided by enhanced grain sliding. Grain growth is, however, strongly temperature dependent and takes place above a threshold temperature. In this case, abnormal grain growth starts to take place at 800°C, resulting to a bimodal microstructure with large grains (up to 3µm) embedded in the matrix of fine grains (~ 800 nm). Previous research [137] demonstrates that grain growth is dominated by an Oswald ripening mechanism driven by the reduction of interface energy, that is, the smallest grains deriving from the precursor powder and early precipitates dissolve in the liquid formed at high temperatures and are being transported in the liquid to larger grains where they re-precipitate.

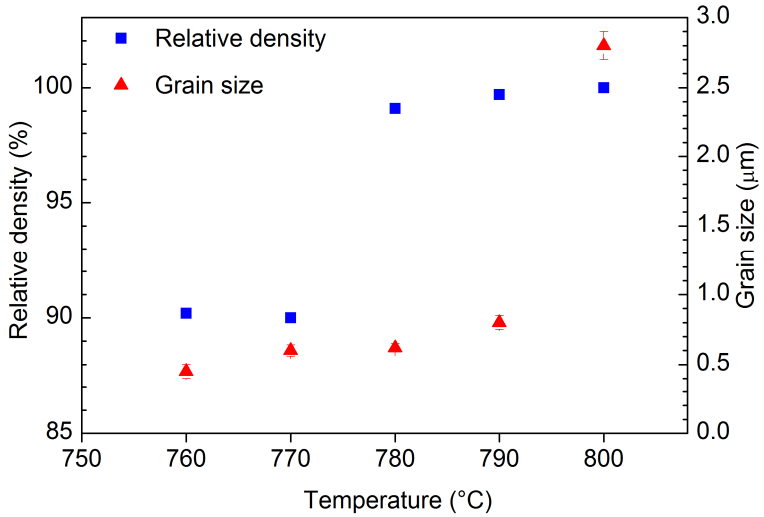

Figure 4. 24 Relative density and grain size plotted versus sintering temperature for a $Al_{67}Cu_{23}Fe_{10}$ sample.

The observed morphology of the sintered sample at 790°C shows that uniform microstructures are preserved throughout the specimen thickness during processing by SPS, while no exaggerated grain growth was registered. The structure presents reminiscent of interlocked microstructures, likely to form in the presence of liquid (molten alloy) phases. Interlocked microstructures of elongated grains are known to promote the improvement of mechanical properties [167]. A decrease in the processing temperature to 780°C leads to a similar uniform microstructure, however some small pores can be noticed here, as well. So we can conclude that a processing temperature of 790°C is the best choice to simultaneously prepare fully densified samples and avoid grain growth.

XRD analysis was used to investigate the in-plane uniformity of the sintered specimens, from the point of view of its phase constitution. The XRD pattern from an SPS processed sample is compared with the XRD pattern from a conventionally HP sample in Figure 4. 25. The sample conventionally compacted for 1 hour at 790°C consists of φ-phase, however not as a single phase, some amount of ω-phase could also be detected. The XRD spectra taken from the SPS processed pellet evidence the presence of single quasicrystalline phase both on the center as well as at the specimen edges [168].

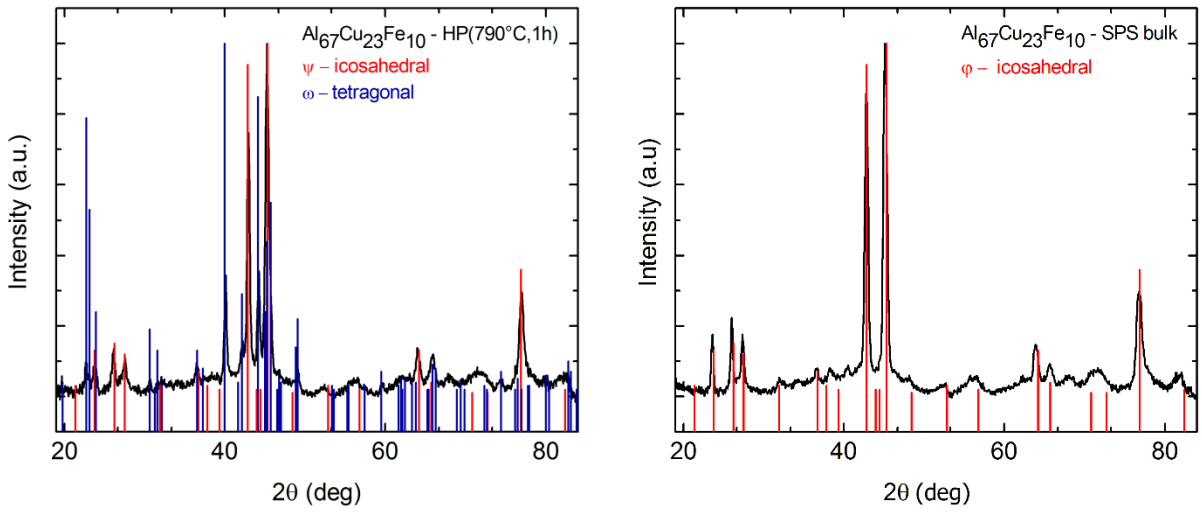

Figure 4. 25 XRD spectra showing the phase composition of a HP sintered pellet at 790°C for 1 hour (left) and an SPS processed pellet at 790°C for 20 min (λ = 1.54184 Å).

Chemical mapping by SEM/EDX further confirmed the chemical homogeneity of the sintered samples (Figure 4. 26). Chemical composition maps were obtained from external pellet surface as well as from fracture surfaces of the sintered body. The analysis performed over an area of 80 µm × 60 µm reveals no significant chemical composition gradients. While Al is uniformly distributed within the sintered specimen, a few grains slightly enriched in either Cu or Fe were noticed. This rather points to the retention of residual amounts of precursor phases in the sintered part.

EDX on the surface reveals small traces of SiO_2 from the sandpaper used to remove the graphite layer. Inside de pellet the composition is otherwise homogenous and finally dispersed.

Vickers hardness was also measured using a square-based pyramid diamond indenter with an angle of 136º between opposite faces subjected to a load of 1 kgf which was maintained for 10 s. After the force has been removed, the diagonal lengths of the indentation were measured and the arithmetic mean, d, was calculated. The Vickers hardness number, HV, is given by:

$$HV = \frac{2Fsin\frac{136^\circ}{2}}{d^2} = 1.854\frac{F}{d^2} \quad (4.2)$$

Where F = Force in kgf, d = arithmetic mean of the two diagonals and HV = Vickers hardness.

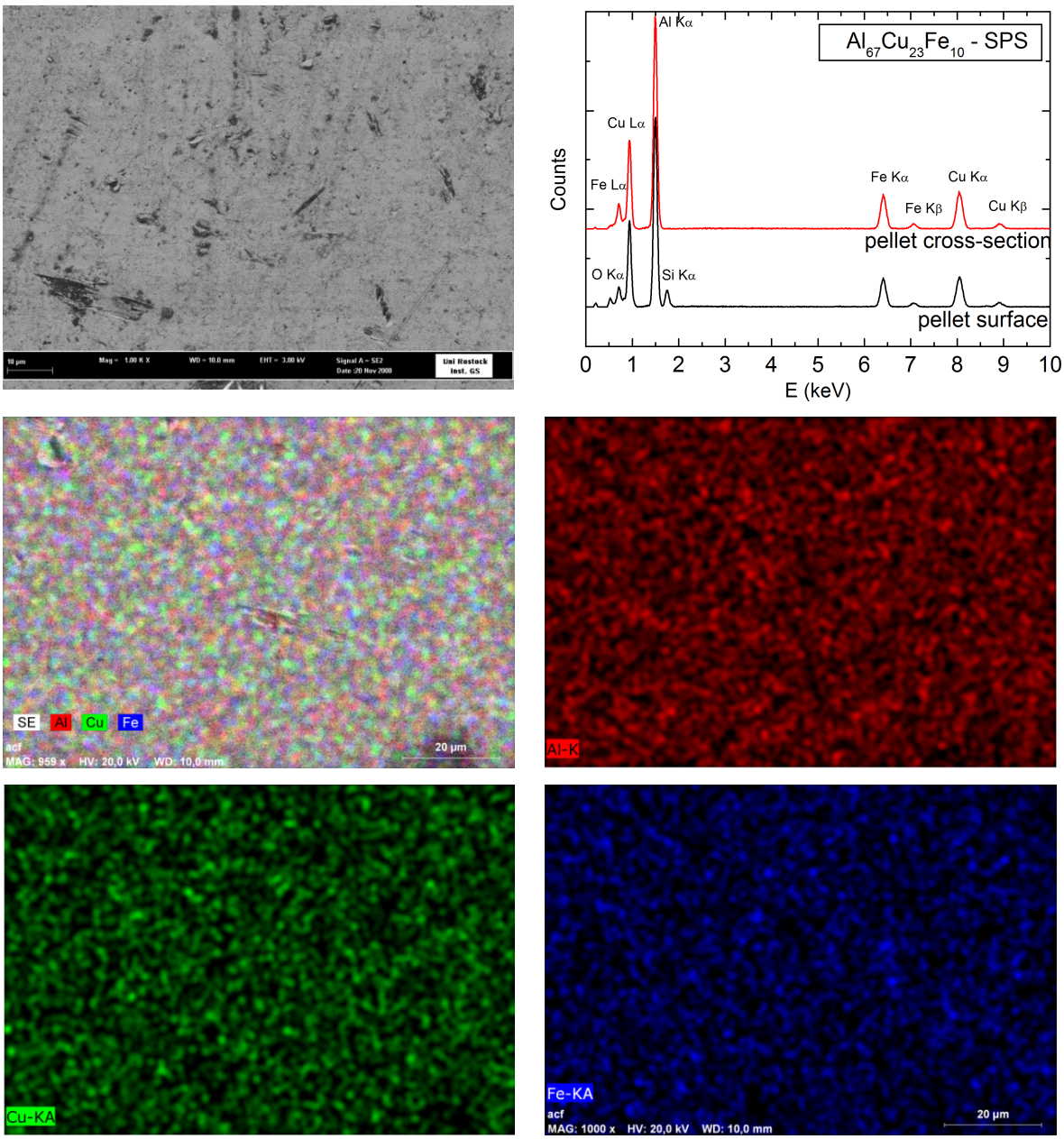

Figure 4. 26 EDX composition maps of the $Al_{67}Cu_{23}Fe_{10}$ pellets, showing a homogeneous spatial distribution of Al (red), Cu (green) and Fe (blue) after SPS processing.

The hardness and Young´s modulus calculated from the multiple load-displacement curves made at different peak indentation loads from 1 to 500 mN are presented in Figure 4. 27. The obtained Young´s modulus is (150 ± 20) GPa and the hardness of the $Al_{67}Cu_{23}Fe_{10}$ SPS processed pellet is (20 ± 5) GPa, about 8% of the Young´s modulus, which is relatively closed to the ratio obtained for diamond and some ceramics. As expected, these values are significantly higher compared to the HP specimen (H = (1.8 ± 0.4) GPa and E = (40 ± 10) GPa) and MW processed sample (H = (6 ±2) GPa, E = (120 ± 30) GPa).

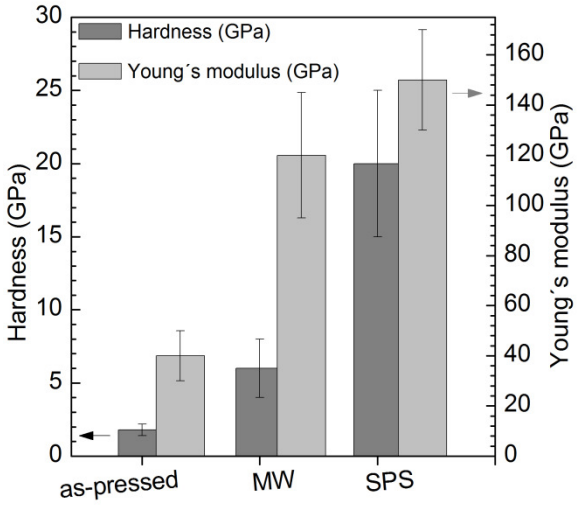

Figure 4. 27 Hardness and Young´s modulus in the as-pressed vs. MW and SPS processed $Al_{67}Cu_{23}Fe_{10}$ pellets.

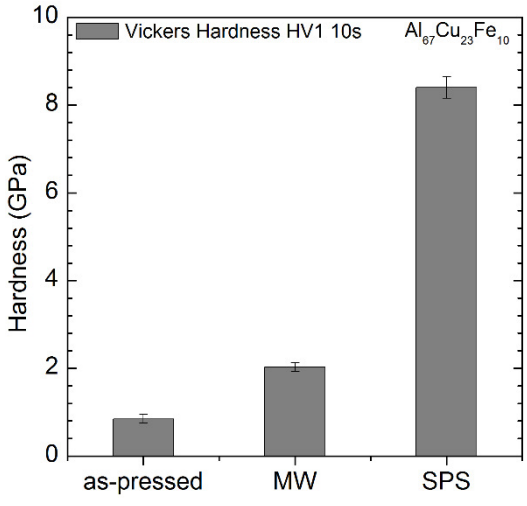

Figure 4. 28 Vickers hardness in the as-pressed vs. MW and SPS processed $Al_{67}Cu_{23}Fe_{10}$ pellets.

We found significant difference between the three samples, namely (0.82 ± 0.02) GPa for the HP sample versus (2 ± 0.05 GPa) for the MW pellet and (8.5 ± 0.2 GPa) for the SPS specimen. This can be explained by the better densification reached on the SPS processing and the special atomic arrangement in the pure quasicrystalline structure.

$Al_{67}Cu_{23}Fe_{10}$ samples have been consolidated by the MW and SPS process and subsequently investigated with respect to their microstructures and mechanical properties. For comparison, appropriate experiments have also been performed by means of conventional hot pressing (HP). Although it is very difficult to achieve elongated grain morphology in $Al_{67}Cu_{23}Fe_{10}$ alloys by means of the HP or MW process, it is possible to obtain an interlocking microstructure, consisting of elongated grains by SPS processing. The interlocking microstructure is responsible for improved mechanical properties, e.g. SPS compacts containing exhibiting remarkable increase in the hardness and elastic modulus compared to MW and HP pellets.

Fully dense $Al_{67}Cu_{23}Fe_{10}$ quasicrystalline pellets can be produced in the SPS process merely by enhanced particle rearrangement via grain boundary sliding accompanied by either diffusion- or reaction-controlled process in the liquid, without, or with very limited grain growth. The rapid densification is ascribed to the retention of a fine particle size throughout the densification cycle, and to the creation of a non-equilibrium liquid phase by rapid heating.

We can conclude that the SPS method is suitable to obtain uniform completely densified pellets containing single icosahedral phase, showing significant improvement in the mechanical properties compared to pellets consolidated by HP or MW.

Chapter 5

Composites reinforced with quasicrystalline particles

In this part of the study, quasicrystal/UHMWPE composites were synthesized using mechanical alloying (MA) followed by spark plasma sintering (SPS) technique. The single-phase quasicrystalline $Al_{67}Cu_{23}Fe_{10}$ powder used for the composites was synthesized as described in the previous chapter.

The goals of this stage of work are as follows:

(1) to perform a comparative study of the properties of UHMWPE powders and quasicrystal/UHMWPE composites formed on its basis in order to ascertain the role of the $Al_{67}Cu_{23}Fe_{10}$ quasicrystalline fillers in the formation of certain types of crystalline phases and morphologies arising during the synthesis.

(2) to investigate the efficacy of preparing composite powder materials with different contents of $Al_{67}Cu_{23}Fe_{10}$ quasicrystalline fillers, by co-milling during low-temperature mechanical alloying.

(3) to synthesize polymer composite bulk samples $Al_{67}Cu_{23}Fe_{10}$/UHMWPE (ACFUHMWPE) using spark plasma sintering and hot processing.

(4) to gain insight into the effect of the amount of quasicrystalline filler and the sintering method on the microstructure, crystallinity and mechanical properties of the composites and the polymer matrix.

5.1 Preparation of composite powders in the solid state. The effect of high-energy ball milling on the composite powders

High-energy ball milling (HEBM) has been used to improve the compatibility between the polymer and metal composite powders, by mechanical alloying. The efficiency of the high-energy ball milling is determined by the collision probability of powders and milling media (balls), the impact force, the oscillating frequency and the amplitude of the equipment.

Typical SEM micrographs of the ACFUHMWPE composites are presented in Figure 5. 1. Low magnification micrographs (a, b, e, f, I, j, m, n) reveal fairly uniform global dispersion of the quasicrystalline particles in the UHMWPE matrix that can readily be achieved by ball milling. However, ball milling could not reduce the size of UHMWPE powder because of its high toughness. High magnification micrographs (c, d, g, h, k, l, o, p) show that most of the polymer beads are spherical, discrete and ~ 30 μm in diameter. Pictures generated with both secondary (SE) as well as backscattering electron detector (BSE) were taken. Especially the pictures generated by the backscattering electron detector (BSE) clearly evidence that the polymer beads (dark) are capped with small quasicrystalline particles (light). Close observation shows that the nanoparticles are located on the surface, indicating they must have assembled at the polymer interface during co-milling. Furthermore, the size of Al-Cu-Fe particles is still fairly uniform, falling between ~100 – 200 nm. Some inhomogeneities are visible on the surface of some of the beads due to aggregated clusters of quasicrystalline nanoparticles. A general conclusion of the visual inspection indicates that, it is possible to obtain a good distribution of fillers in the polymer matrix in the solid state when fillers and polymers are co-milled. During mixing, the energy of the collisions between the relatively different particle sizes, large coagulated UHMWPE spheres and small Al-Cu-Fe particles, is sufficient to overcome the agglomerate strength. Between 10 wt% and 30 wt% $Al_{67}Cu_{23}Fe_{10}$ the particles are single, uniformly dispersed and far apart from each other. This occurs because the electrostatic forces have been completely overcome by the polymer beads. With an increase in the filling factor of $Al_{67}Cu_{23}Fe_{10}$ quasicrystalline powder inclusions to 40wt%, the interparticle distance becomes smaller and leads to an interaction between the nanoparticles, hence agglomeration. Many UHMWPE spheres are surrounded by Al-Cu-Fe

nanoparticles and these nanoparticles can be seen to be located around the surface of the original polymer beads.

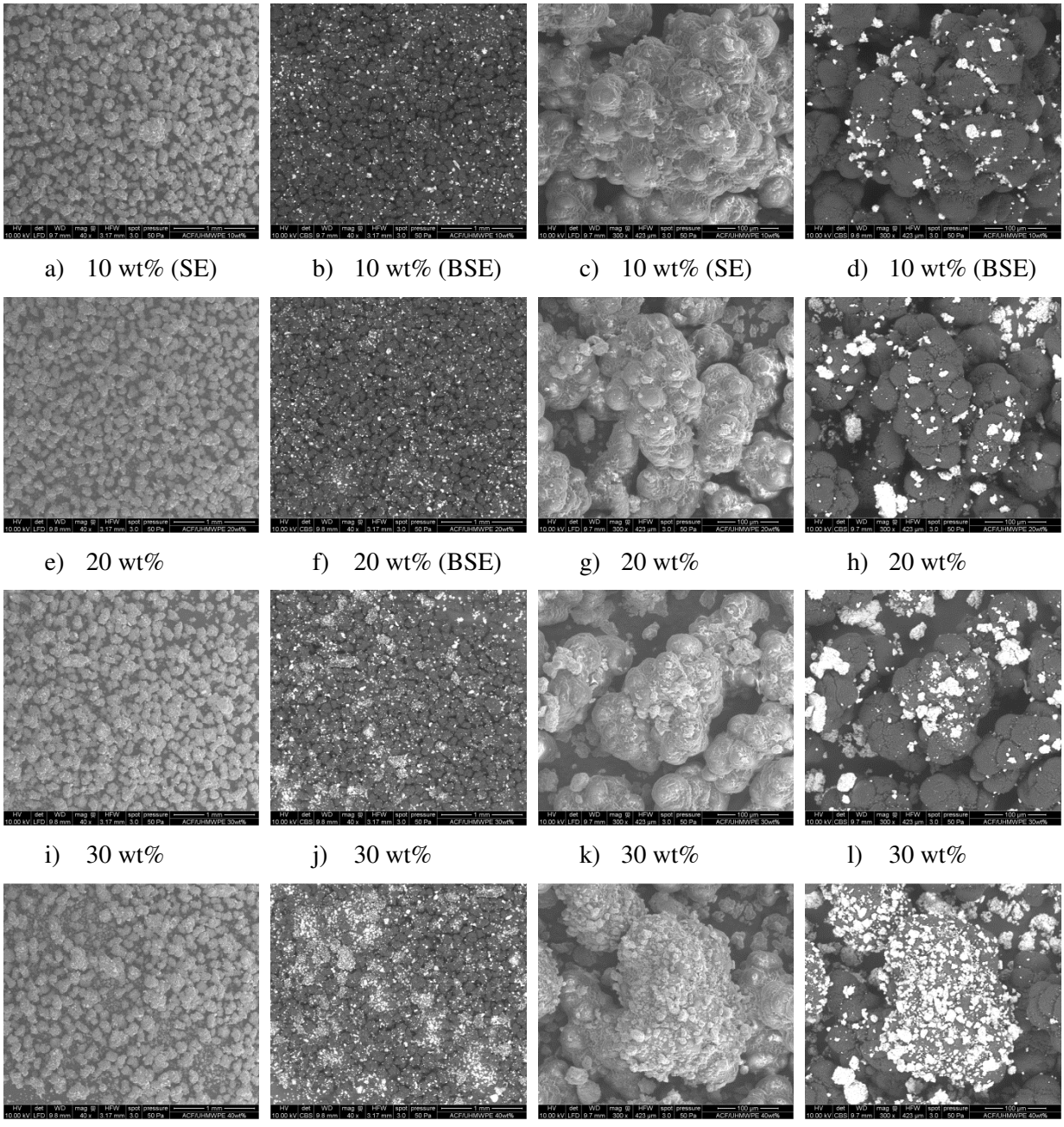

a) 10 wt% (SE) b) 10 wt% (BSE) c) 10 wt% (SE) d) 10 wt% (BSE)

e) 20 wt% f) 20 wt% (BSE) g) 20 wt% h) 20 wt%

i) 30 wt% j) 30 wt% k) 30 wt% l) 30 wt%

m) 40 wt% n) 40 wt% (BSE) o) 40 wt% p) 40 wt%

Figure 5. 1 Secondary electron and backscatter SEM images showing the distribution of the i–QC particles (light) in the UHMWPE matrix (dark): a, b, c, d) ACFUHMWPE 10wt%; e, f, g, h) ACFUHMWPE 20wt%; i, j, k, l) ACFUHMWPE 30wt% and m, n, o, p) ACFUHMWPE 40wt%.

5.2 Crystallinity studies

After the microscopic investigation of the composite powders, the structure change during heating was analyzed by in-situ X-ray diffraction. The analysis of the XRD data of the UHMWPE and the ball-milled composites demonstrates that the mechanical treatment leads to changes in the orthorhombic phase of the UHMWPE. Figure 5. 2 show the sequence of diffraction patterns collected in-situ during non-isothermal annealing. During continuous heating of the UHMWPE sample, the transformation path registers two changes: the disappearance of the (2 0 0) orthorhombic reflection at around 80°C and the appearance of an unidentified peak at 230°C. This reflection disappears at 270°C which corresponds to a slight shift and an increase in the intensity of the orthorhombic (1 1 0) peak. Definite assignment of a phase to the new reflection is not straightforward, as only one reflection is observed. The increase in the scattering intensity can be attributed to an increase of the crystalline lamellar thickness. Direct evidence arising from the microstructural changes of the crystalline domains is provided by the SEM pictures taken after hot powder compaction with 10 $K \cdot min^{-1}$ at 300°C (Figure 5. 10).

The composite sample prepared by mechanical treatment is a mixture of two phases, namely the orthorombic UHMWPE and the icosahedral quasicrystalline phase $Al_{67}Cu_{23}Fe_{10}$. The quantitative ratio between these phases is close to that in the composition of the initial batch. Upon heating the composite powders to 300°C, the orthorhombic (2 0 0) reflection disappears at around 130°C, which corresponds to melting of the polyethylene matrix, as indicated by the DSC thermogram (Figure 5. 3a). The initial scattering intensity of the orthorhombic (1 0 0) reflection is high compared to the as-received UHMWPE powder, suggesting a continuously change in the structural orientation of the polymer matrix during milling. The intensity of the orthorhombic peak gradually decreases with increasing temperature, accompanied by a widening in the FWHM (δ), showing a higher symmetry of the orthorhombic phase and the increase of lamellar periodicity of crystals. Similar phase transition behavior was reported by Seto and co. in stress-deformed polyethylene [169]. It is well known that the thermal motion of the molecules is important at elevated temperature and low heating rates. Gliding at boundaries between crystallites and some other processes involving diffusion may possibly play a more important role than the above mentioned phase transformation process.

As expected, no change in the icosahedral reflections was observed, suggesting the quasicrystalline phase remains stable and no further grain growth takes place until 300°C.

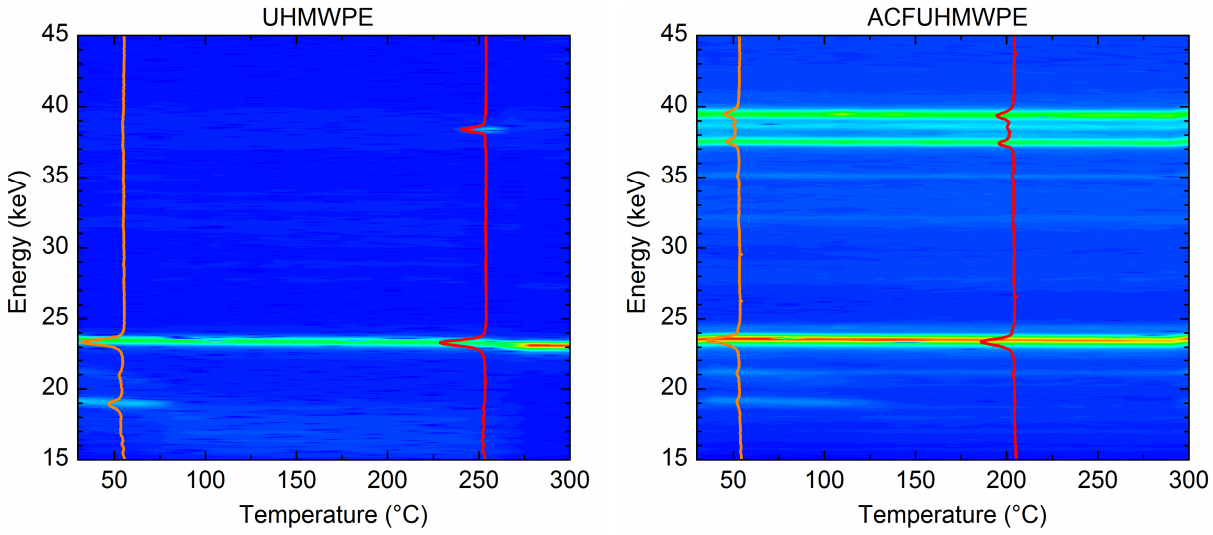

Figure 5. 2 In-situ EDXRD diffractograms (HASYLAB/F2.1) showing the phase composition change under heating with 10 K/min in UHMWPE (as received) and ACF/UHMWPE 30 wt% powders (after ball milling).

DSC was further carried out in order to give a better understanding of the phase transition observed by in-situ XRD. The influence of the milling process and the quasicrystalline amount in the composites on the overall degree of crystallinity of the UHMWPE was studied. The degree of crystallinity is one of the most important characteristic of the polymer which determines its mechanical properties such as yield stress, elastic modulus and impact resistance. The calculation of the overall degree of crystallinity (XC%) by DCS involves drawing a linear arbitrary baseline from the first onset of melting to the last trace of crystallinity and determines the enthalpy of fusion by integration of the area under this endotherm.

$$XC = \Delta H_f(T_m) / \Delta H_f^0(T_m^0) \qquad (5.\ 1)$$

Where: XC – weight fraction extent of crystallinity

$\Delta H_f(T_m)$ – Enthalpy of fusion measured at the melting point T_m

$\Delta H_f^0(T_m^0)$ – Enthalpy of fusion of the totally crystalline polymer at the equilibrium melting point (293 J/g for 100% crystalline UHMWPE).

Taking the reorganization processes into account, it is possible to correlate the melting temperature with the crystal dimension, using Gibbs-Thomson equation [170]:

$$T_m = T_m^\infty - \frac{C_1}{d_c} \qquad (5.\ 2)$$

With $C_1 = \frac{2\sigma_e T_m^\infty \Delta z}{\Delta H}$ = 132 K·nm (5. 3)

Where: σ_e – surface free energy per endgroup (5 kJ·mol^{-1})

ΔH – the molar heat of fusion per C_2H_4-group (293x28 J·mol^{-1} = 8.2 kJ·mol^{-1})

Δz – the length of a C_2H_4-unit in chain direction (0.254 nm)

T_m^∞ – the equilibrium crystallization/melting temperature of polyethylene (141.2°C)

d_c – the lamellar thickness of UHMWPE crystalized form the melt

No correction is usually made for the variation in the specific heats with temperature or the differences between the liquid and crystalline values.

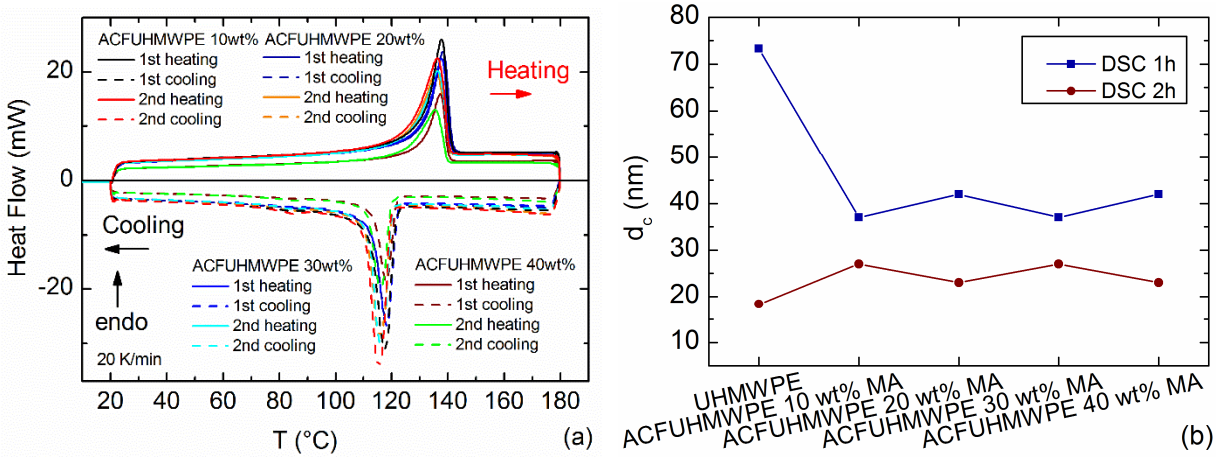

Figure 5. 3 (a) DSC curves obtained on heating the ball-milled composite powders up to 180°C. The DSC measurements were carried out with heating and cooling rates of 20 K/min and holding times of 2 min at the end of the scans. (b) Representation of the crystal thickness, plotted for the as-received UHMWPE and the mechanically alloyed ACFUHMWPE powders, calculated using Gibbs-Thomson equation for the first and the second heating cycle (1h, 2h).

A general observation of the DSC experiments on the powders show a shift on the melting peaks between the first scan and the second heating cycle. All further heating and cooling cycles resulted in curves equivalent to the second cycle. The melting temperature decreases for the once molten powder, from 143°C at first heating to 134°C during the second heating. The recrystallization peak seen on the cooling curves shows a smaller shift from 118°C to 117°C. The corresponding overall crystallinity is calculated from interpolations of the DSC curves and is listed in Table 5. 1. As it can be seen, the crystallinity of the as-received UHMWPE decreases considerably between the first and the second heating cycle from 68% to 50%, which is in good agreement with other literature values [171]. The ball-milled composite powders show from the beginning a crystallinity of 50%, which remains almost unchanged after further heating. This suggests that, although no significant morphological

change was observed on the milled powders (Figure 5. 1) there is an indication that structural deformation during mechanical alloying leads to a decrease of overall crystallinity. Moreover, a decrease in the lamellar thickness of the polymer crystals from 74 nm in the as-received UHMWPE (which corresponds to ~ 291 polyethylene units) to 35 – 40 nm (~ 137 – 157 polyethylene units) in the ball-milled samples was registered (Figure 5. 3 b).

Table 5. 1 Measured melting peak temperatures (TM), recrystallization temperatures (TC), calculated enthalpy of fusion (ΔHf) and overall degree of crystallinity (XC) for the as-received UHMWPE powder and the ball milled composite powders.

Probe	TM1 (°C)	ΔHf1 (J/g)	TC1 (°C)	TM2 (°C)	ΔHf2 (J/g)	TC2 (°C)	XC1 (%)	XC2 (%)
UHMWPE powder	143	199	118	134	146,5	117	68	50
ACFUHMWPE 10 wt% milled powder	137,6	141,74	115,12	136,33	150,5	117,38	48,4	51,3
ACFUHMWPE 20 wt% milled powder	138	125,25	116,06	135,37	126,57	118,01	42,8	43,2
ACFUHMWPE 30 wt% milled powder	137,62	158,9	116,09	136,33	166,6	118,03	54,2	56,9
ACFUHMWPE 40 wt% milled powder	138	144,7	115,76	135,48	151	118,02	49,4	51,5

5.3 Solidification behavior

The crystallization at high pressure has attracted special interest because, following early work on polyethylene [80], it appeared that this provided a means to preparing `extended-chain` material instead of the chain-folded samples produced by conventional treatments. Such an altered molecular conformation could be expected to produce changes in mechanical properties because of the inherent anisotropy of extended chains, with properties along molecular chains very different to those in transverse directions. In chain-folded crystals, by contrast, the interruption of the folds dominates mechanical behaviour by introducing weakly-bonded interfaces and is a barrier to transport processes.

The ACFUHMWPE milled powders were subsequently solidified by SPS. As already discussed in the previous chapter, the fast solidification freezes the structural state at a high temperature and the grain growth is retarded. This way, the densification can be reached fast, without further changes in the overall crystallinity.

Typical shrinkage data recorded during densification of the composites by SPS are given in Figure 5. 4. It is seen that densification occurs both during the initial heating stage as well as in the 5 minutes holding time at 170°C. The densification begins immediately at room temperature and occurs mainly between 50 and 100°C when a constant heating rate of 10 $K \cdot min^{-1}$ and a compressive stress of 7 MPa were applied. The recorded maximum shrinkage rate is 0.7 $mm \cdot min^{-1}$ after 4 minutes (1). The last displacement peak (2) recorded after 1 minute of holding at 170°C could be explained by complete melting of the polymer and extensive polymer chain rearrangement. Full density was approached after holding at 170°C for 5 min. At the end of the SPS processing (3) the final elimination of closed pores occurs.

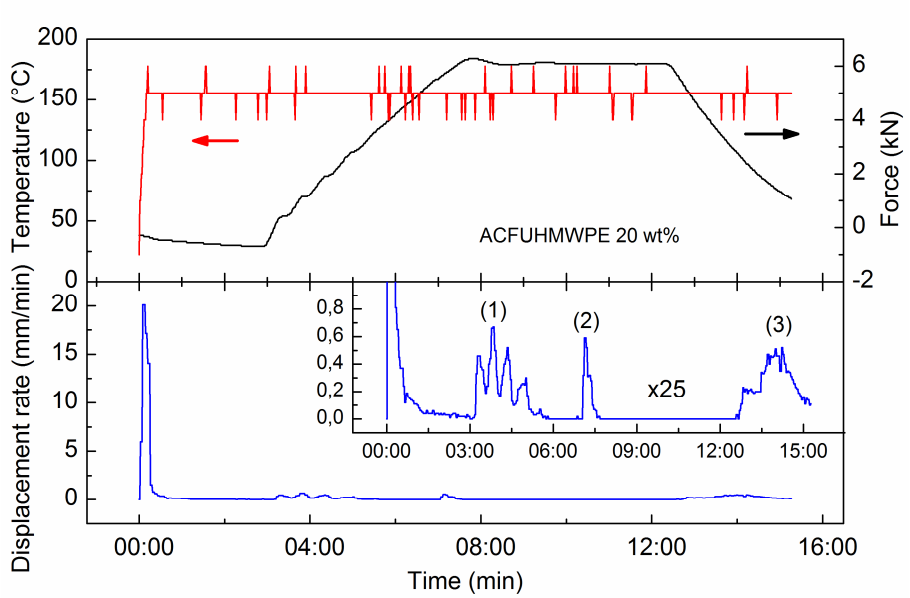

Figure 5. 4 SPS sintering diagram of the ACFUHMWPE 20wt% milled powder. During the initial stage, the powders are heated to 170°C with 10 K/min, under a load of 7 MPa. The isothermal stage is defined by a dwell time of 5 min at the sintering temperature (170°C). (SPS diagrams registered for UHMWPE, ACFUHMWPE 10, 30 and 40wt% are similar).

The microstructure of the SPS compacted composites at 170°C is presented in Figure 5. 5. The sintered pellets indicate a homogeneous microstructure, with no porosity. SEM micrographs show the polymer chains arranged in a fine lamellar microstructure, which is regularly stacked. It may be said that the lamellae grow perpendicularly to the direction of molecular orientation prior to crystallization and the growth is in the direction parallel to the b-axis, which corresponds to the radii of polyethylene spherulites. The pictures confirm the hypothesis that SPS processing is a good method for producing extended-chain materials.

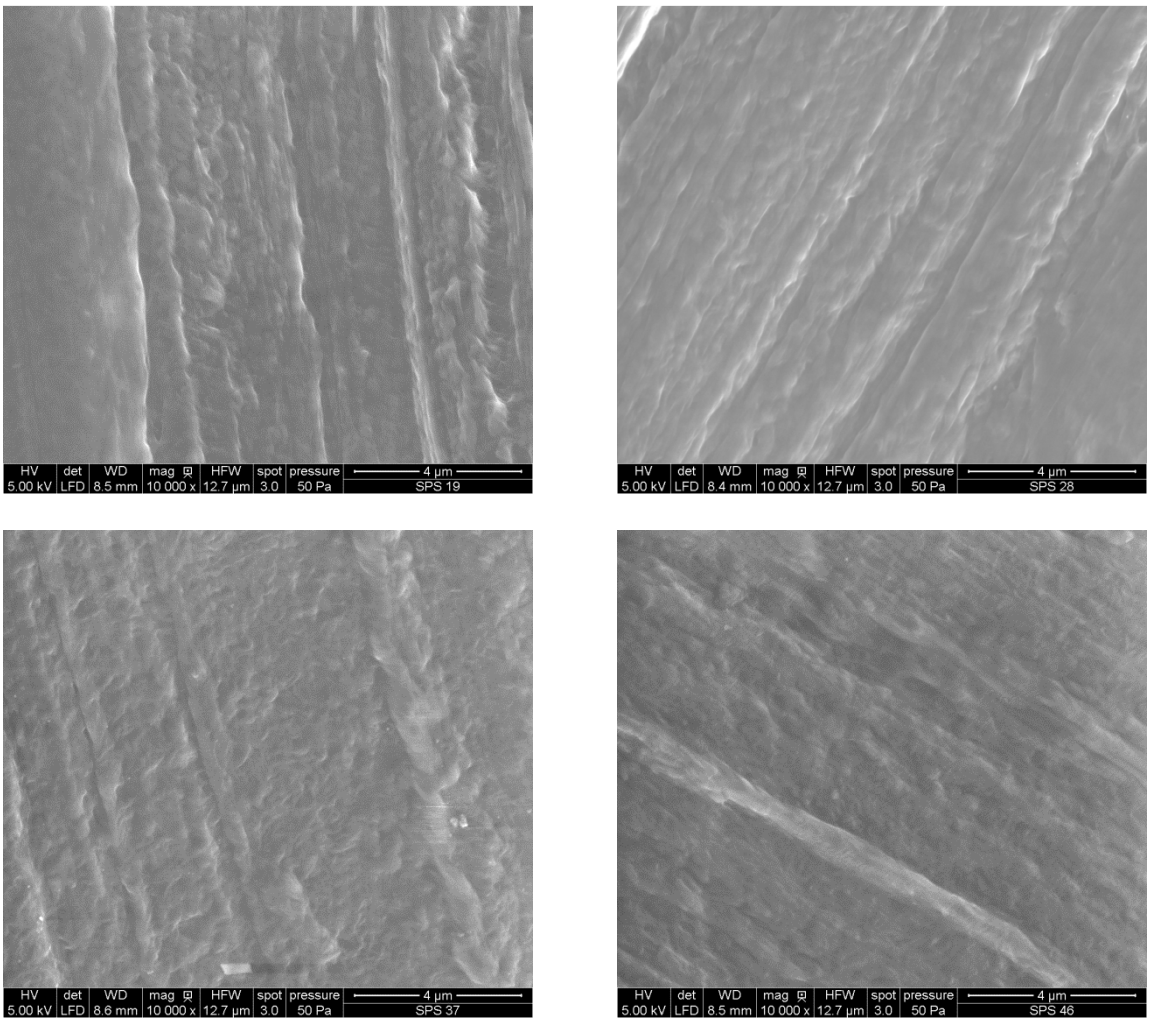

Figure 5. 5 SEM representation for the regular lamellar structure formed in ACF/UHMWPE SPS-processed pellets (a) ACFUHMWPE 10wt%, (b) ACFUHMWPE 20wt%, (c) ACFUHMWPE 30wt% and (d) ACFUHMWPE 40wt%.

The EDX mapping (Figure 5. 6) reveal that the small agglomeration of quasicrystalline fillers present in the initial mixed powders disappear, leading to a compact composite with a fine microstructure to be obtained after SPS processing. This is mainly due to the limited exposure to high temperatures. Chemical mapping by SEM/EDX confirmed the high homogeneity of the sintered pellets. It may thus be concluded that either a uniform thermal field was applied throughout the volume of the bulk sintered body during FAST processing or that thermal gradients did not affect the phase structure of the specimens. Rapid densification is achieved without alteration of the initial ultrafine microstructure of the starting powders.

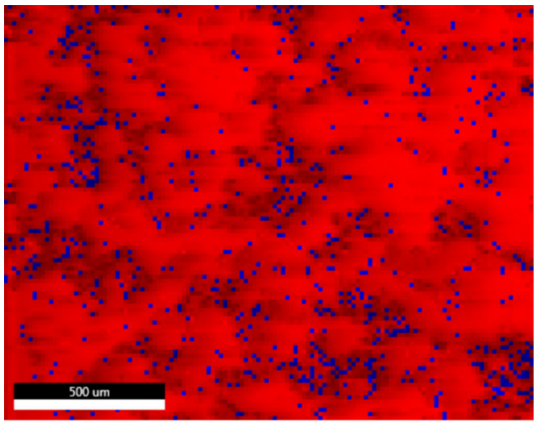

(a) Phase distribution picture (blue – quasicrystalline particles, red – polymer)

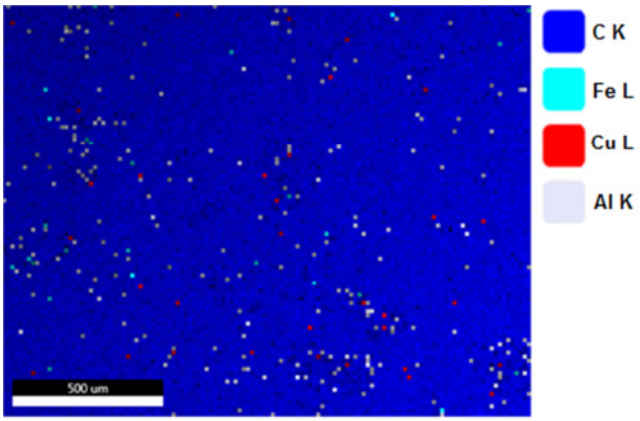

(b) Picture showing the element distribution (10 kV)

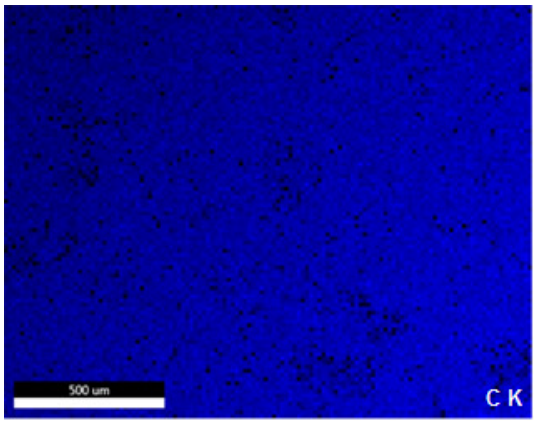

(c) C K

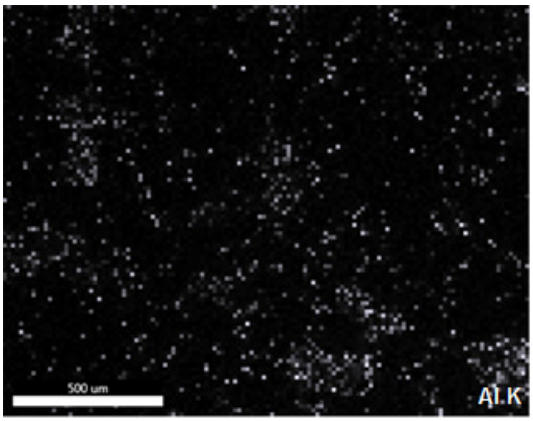

(d) Al K

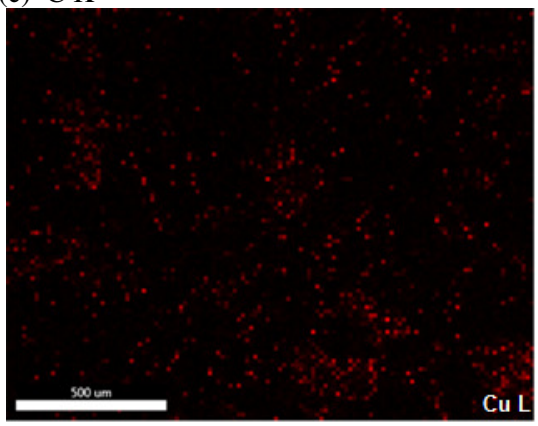

(e) Cu L

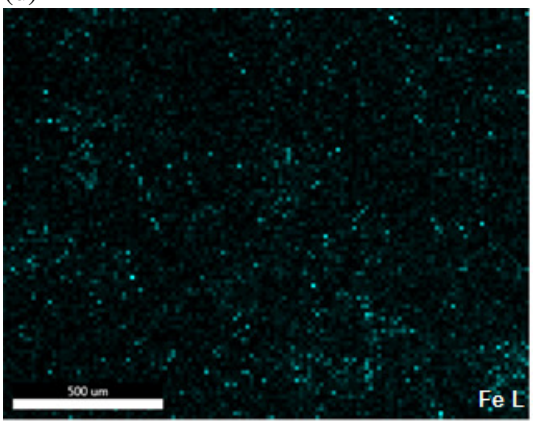

(f) Fe L

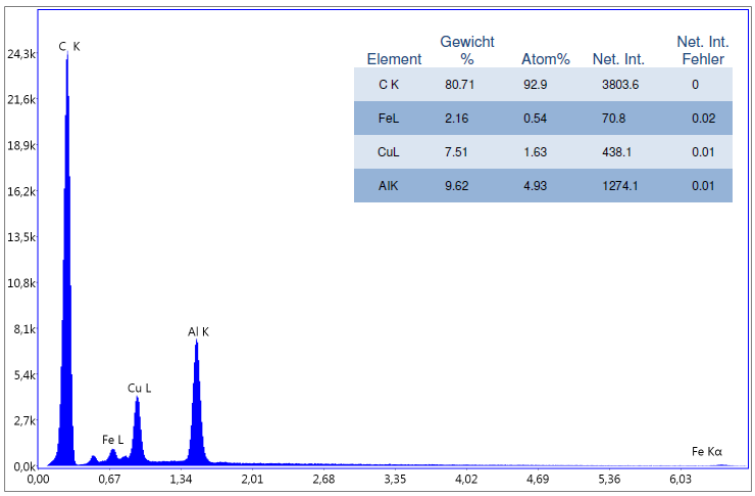

(g) EDX Sum Spectra

Figure 5. 6 (a) EDX Phase distribution picture, (b) Element distribution picture, (c-f) Element Mapping showing the distribution of C, Al, Cu and Fe in ACFUHMWPE 20wt% bulk sample (higher color intensity means a higher element concentration) and (g) EDX Spectra and element table showing the calculated element composition in wt.% and at.%

The observed morphology of the FAST sintered pellets is reminiscent of interlocked microstructures, likely to form upon (partial) melting. Interlocked microstructures are known to assist the general improvement of mechanical properties (toughness) of the FAST sintered parts [60]. The quantification results show that the initial weight distribution of 20 wt% quasicrystalline fillers and 80 wt% UHMWPE is maintained after sintering.

X-ray microdiffraction was employed to investigate the uniformity of the sintered parts. Synchrotron radiation diffraction patterns were collected from the outer surfaces of the pellets. The diffraction patterns taken from the center and specimen edge are identical. Synchrotron radiation diffraction patterns (Figure 5. 7) reveal the presence of nine peaks distinctly associated with the pure icosahedral φ-phases phase and three broad reflection lines given by the orthorhombic UHMWPE. The orthorhombic phase is indexed by (*h k l*) Miller indices.

Comparison of diffraction data for UHMWPE and different weight fractions of quasicrystalline particles in the polyethylene matrix show two events: a growth and sharpening of the icosahedral peak combined with a slight decrease and widening of the orthorhombic peak.

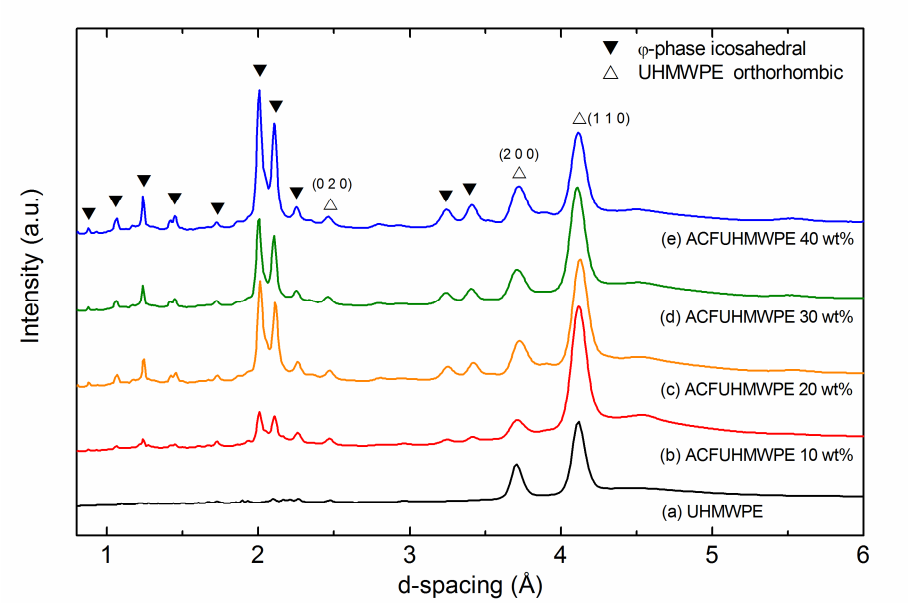

Figure 5. 7 XRD patterns of UHMWPE (a) and ACFUHMWPE composites prepared by SPS: ACFUHMWPE 10wt% (b), ACFUHMWPE 20wt% (c), ACFUHMWPE 30wt% (d) and ACFUHMWPE 40wt% (e).

The influence of the sintering process in the overall crystallinity of the polymers was further studied by DSC. Figure 5. 8 shows the crystallization and melting behaviour of the SPS consolidated UHMWPE and ACF/UHMWPE 30 wt% at 10 and 100 $K \cdot min^{-1}$. Samples heated with 10 $K \cdot min^{-1}$ melt at the same temperature and show same overall crystallinity after the first scan. A second exothermic peak can be observed during first heating at 200°C in UHMWPE and 201°C in ACFUHMWPE 30 wt% which can be related to the formation of a second phase observed in the in-situ XRD patterns (Figure 5. 2). After the second scan there is an increase of the overall polymer crystallinity from 51% to 59% in UHMWPE and from 52% to 61% in ACFUHMWPE 30wt%. No further change in crystallinity was registered after following heating and cooling cycles. The crystal thickness though, registers a decrease from 31 nm in UHMWPE, respectively 21 nm in ACFUHMWPE 30wt% to 16 nm when the samples are heated with 10 $K \cdot min^{-1}$ (Figure 5. 9) and remains constant after further DSC scans. Samples heated with 100 $K \cdot min^{-1}$ show a slightly different behavior. The overall crystallinity decreases when higher heating rates are applied and also remains constant (XC_{UHMWPE} = 49% and $XC_{ACFUHMWPE30wt\%}$ = 51%) after the second heating cycle.

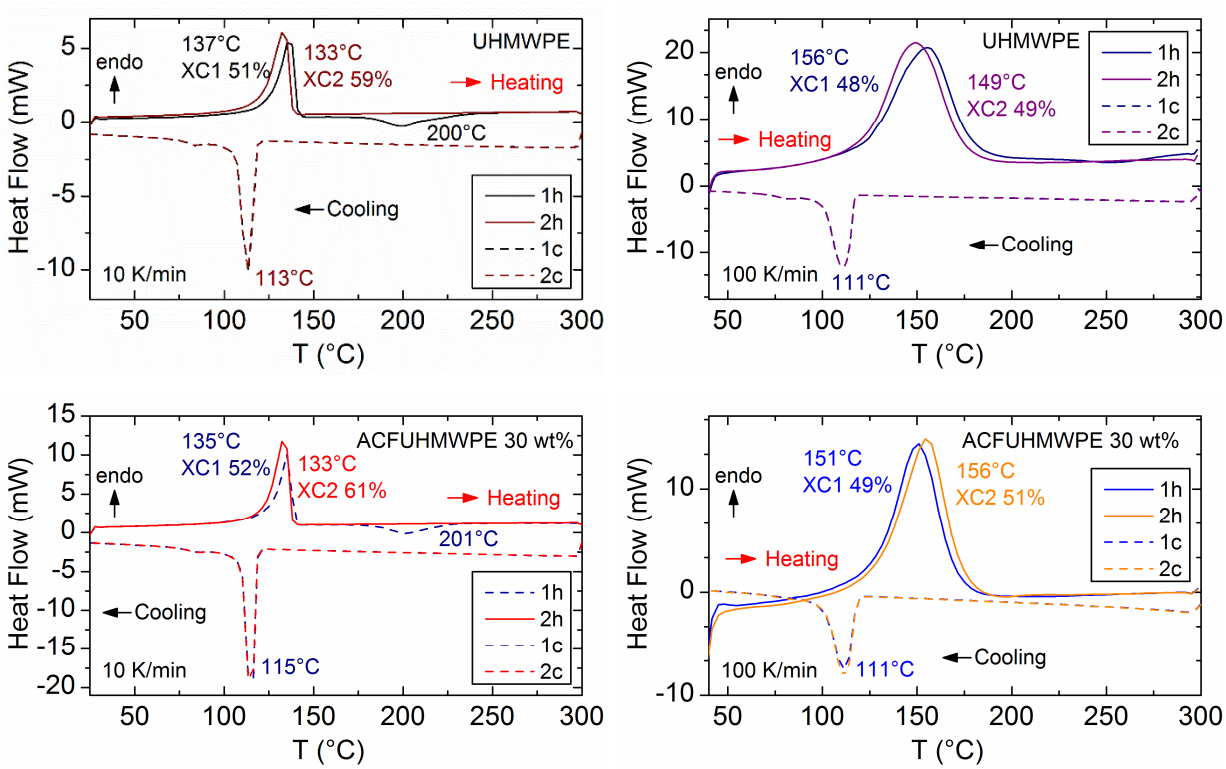

Figure 5. 8 DSC curves of the UHMWPE and ACF/UHMWPE 30 wt% bulk samples heated with 10 and 100 K/min, respectively.

Depending on the crystal morphology after consolidation, different reorganization processes of the amorphous and crystalline regions, which are connected by chains can occur, which can be observed as a shift in the melting region at different heating rates. Indeed, as seen from the Figure 5. 8, there is a significant positive shift from 137°C at a heating rate of 10 K·min^{-1}, to 156°C at a heating rate of 100 K·min^{-1}, in both samples. The increase in the melting temperature with increasing the heating rate generally occurs in extended chain crystals and it can be attributed to reorganization processes and superheating [172]. Likewise, the melting temperature on the first heating (156°C) is lost on second scan (149°C) when heated with 100 K·min^{-1} and the same is registered when the heating rate is 10 K·min^{-1}. The differences in the melting behavior, revealed during different heating rates, have consequences on the chain dynamics. The higher the heating rate is, the faster is the gain in entropy during phase transformation from crystalline state into melt, resulting into entanglement formation on melting the disentangled polymer. Higher the number of entanglements at the initial state, faster is the entanglement formation. This explains the loss of the melting temperature on the second scan when faster heating.

With the decrease in the melting temperatures, also the lamellar thicknesses of the polymer crystals decrease. Thus, in UHMWPE after the first heating cycle, the thickness decreases from 31.4 nm to 16 nm, as seen in Figure 5. 9. As expected, together with increasing the heating rate, another decrease in the crystal thickness up to 9 nm was found in UHMWPE. After the second heating though, the melting temperature surprisingly increases to 156°C, together with the lamellar thickness (17 nm). In the case of the polymer in ACFUHMWPE 30 wt% the behavior is completely opposite crystal thickness is 13 nm after the first heating and decreases to 9 nm after the second heating. So one can conclude a slight different chain dynamics and organization occurs inside the composites compared to the pure UHMWPE.

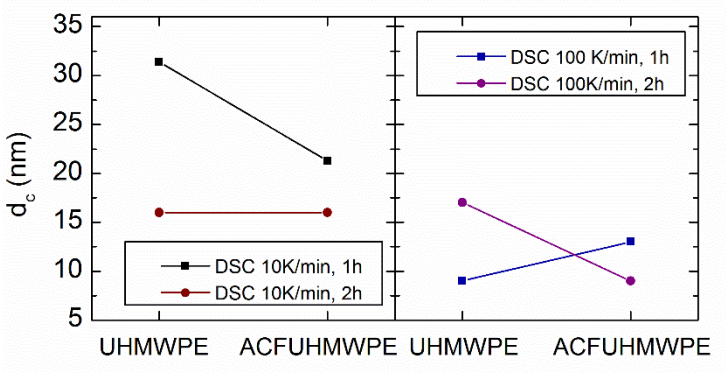

Figure 5. 9 Representation of the crystal thickness at the end of crystallization, plotted for UHMWPE and ACFUHMWPE 30wt% samples, calculated using Gibbs-Thomson equation for 10 $K \cdot min^{-1}$ and 100 $K \cdot min^{-1}$ heating rates after the first and the second heating cycle (1h, 2h).

Indeed, identification of the morphology associated with the bulk samples shows that the chain twist results in axial twisting of growing lamellae that is manifested as banded spherulites. Figure 5. 10 (a, b) shows the characteristic appearance of chain-folded crystals, produced by recrystallizing from the melt of a UHMWPE bulk sample at 113°C, with 10 $K \cdot min^{-1}$. The texture is spherulitic with characteristic growth of discrete fibers which exhibit small angle branching. The fibrils are ribbon-like lamellar crystals with about 1 μm width and a considerable length. The long chain molecules are aligned normal to the planes of these lamellar fibrils, as result of having folded back and forth on their edges during crystallization. The spherulite boundaries and the radial stripes can be clearly observed in Figure 5. 10 (a, b). As temperatures of crystallization are increased, the textures of the fibrils become finer, with a more rounded cross-section, as observed in the samples heated up with 100 $K \cdot min^{-1}$ (Figure 5. 10 c, d, g, h). Here again, the molecules are arranged more or less perpendicularly to the fiber axes and these fibrils are chain-folded lamellae of the same kind.

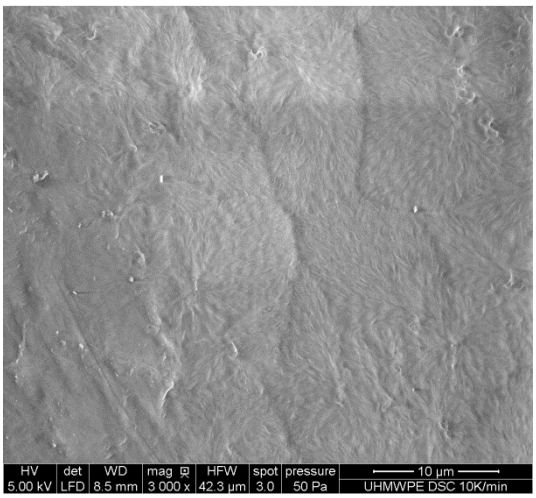

a) UHMWPE 10 K/min, 3000x

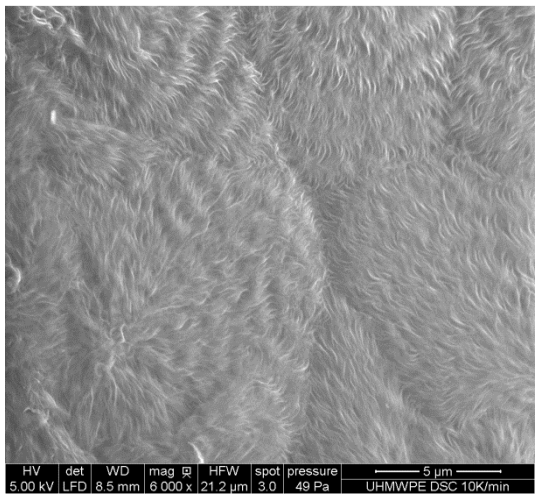

b) UHMWPE 10 K/min, 6000x

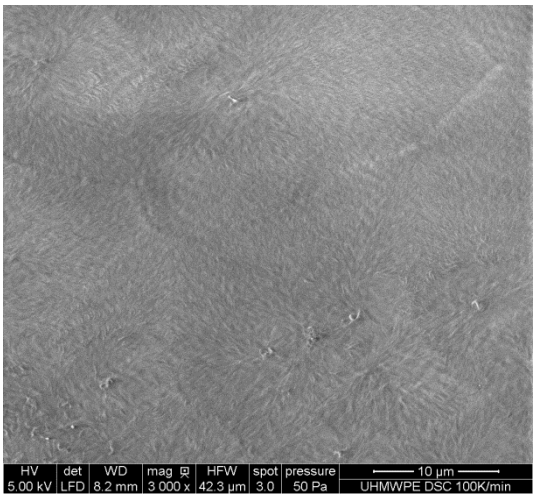

c) UHMWPE 100 K/min, 3000x

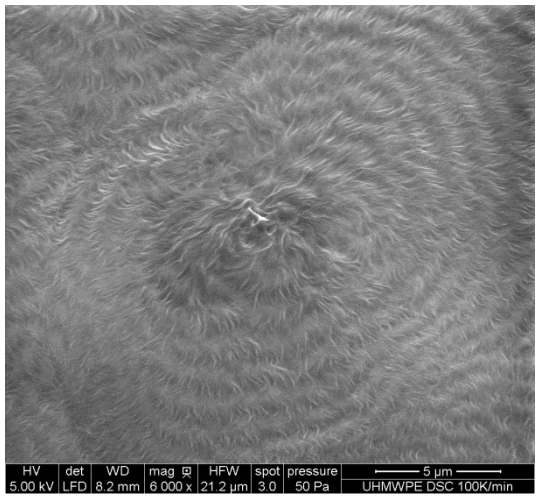

d) UHMWPE 100 K/min, 6000x

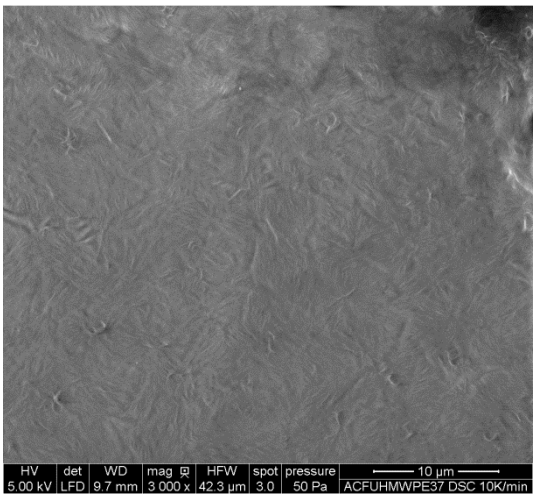

e) ACFUHMWPE 30wt%, 10 K/min, 3000x

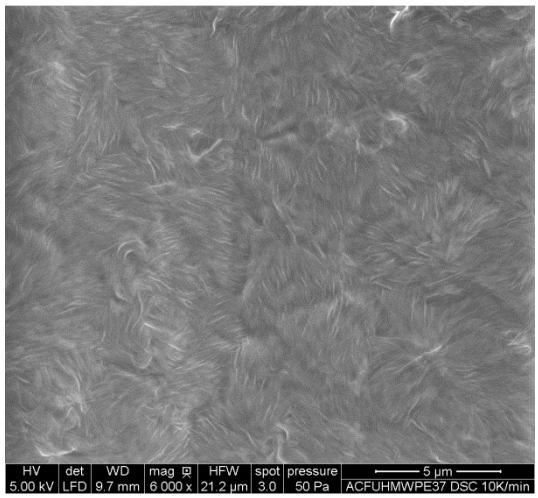

f) ACFUHMWPE 30wt%, 10 K/min, 6000x

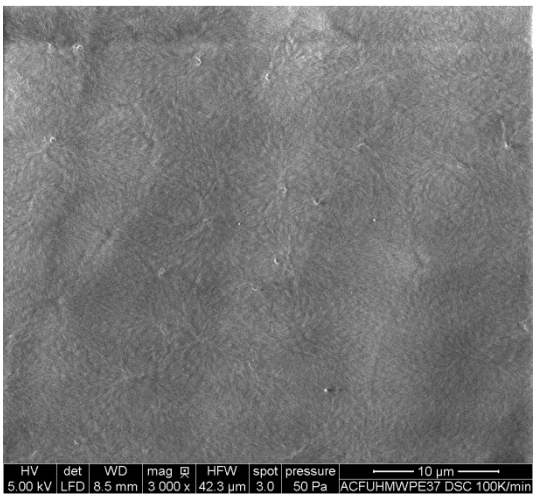

g) ACFUHMWPE 30wt%, 100 K/min, 3000x

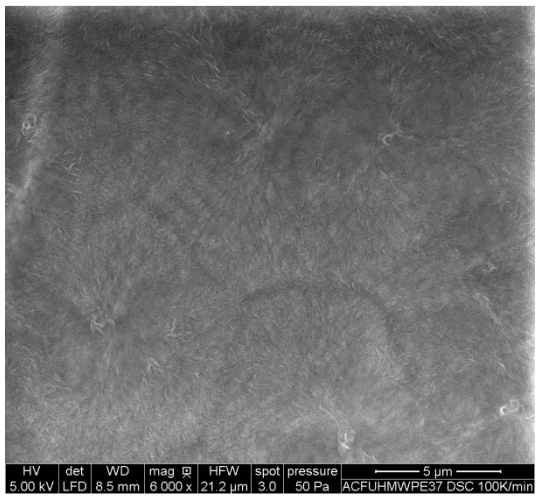

h) ACFUHMWPE 30wt%, 100 K/min, 6000x

Figure 5. 10 SEM pictures taken on the bulk samples UHMWPE and ACFUHMWPE 30 wt% after DSC treatment, using 10 and 100 $K \cdot min^{-1}$ heating rate.

The SEM micrographs taken using ACFUHMWPE 30wt% bulk sample heated up with 10 $K \cdot min^{-1}$ show a quite different penton-spherulitic structure, on a coarser scale as the previous, with shorter lamellar fibrils and an intermediate diffuse phase boundary obtained directly by SPS. In the nomenclature of Keith and Padden [173] a coarse texture is one in which the fibers or fibrils have relatively large cross-sections and are separated to a relatively greater extent by uncrystallized melt. Typical for slowly grown penton-spherulites, is the formation of so-called 'flower leaves', which can be observed in the Figure 5. 10 (e, f). So, although no significant change in the crystallinity of the polymer in ACFUHMWPE composite compared to the UHMWPE sample was recorded, the presence of the QC phase does affect the crystallization process on slow heating rates. On faster heating, the morphology of the ACHFUHMWPE composites is similar to the polymer.

In conclusion, the change of overall crystallinity brought by the application of pressure of 7 MPa in the SPS process is insignificant (see Figure 5. 11(b)). The melting temperature of the SPS bulk samples registers no big change compared to the as-milled powders (see Figure 5. 11(a)). During recrystallizing from the melt however, the temperature registered on the bulk samples is smaller compared to the powders. On the other hand, the SPS sintering results into a reduction of lamellar thickness of the polymer crystals and the formation of stacked lamellae with a regular structure.

Below the melting point, the ACFUHMWPE composites containing crystallizable UHMWPE are heterogeneous systems, as the components separate from each other during solidification.

However, miscibility within the remaining phase may still be possible and the homogeneity or heterogeneity of the quasicrystalline phase affects the crystallization process.

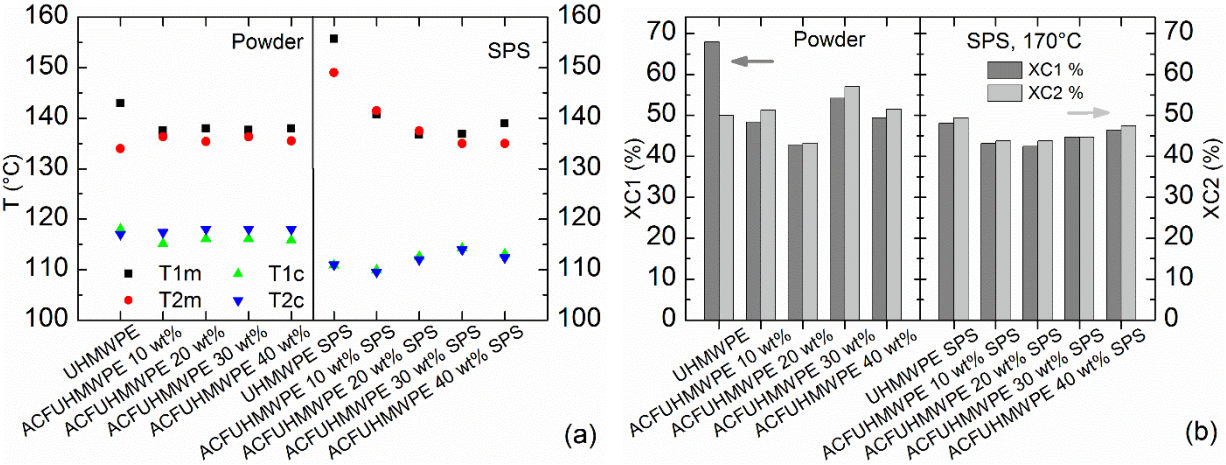

Figure 5. 11 (a) Graphical comparison of the melting temperature for the UHMWPE and ACFUHMWPE powder composites, respectively SPS processed bulk samples. (b) Graphic comparing the overall crystallinity after the first scan (XC1) and after the second scan (XC2) for the powders and SPS samples, respectively.

The results show no influence of the weight percentage of quasicrystalline filler in the overall crystallinity of the polymer (see Figure 5. 11 (b)), which leads to the conclusion that the interphase between the QC particles and the polymer plays no significant role in the overall crystallinity.

5.4 Mechanical properties

5.4.1 Nanoindentation

The multiple load-displacement curves of the indentations made at a 30mN peak indentation load and the hardness and Young´s modulus as a function of indentation contact depth are shown in Figure 5. 12 for the UHMWPE and the ACFUHMWPE sintered composites. The loading and unloading curves for UHMWPE show nearly the same shape, suggesting that deformation after the multiple loading is almost entirely elastic (Figure 5. 12 a-b).

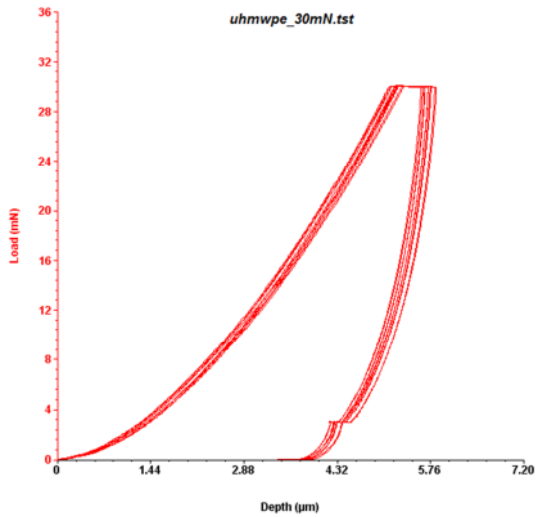

(a) The load-displacement curves for UHMWPE

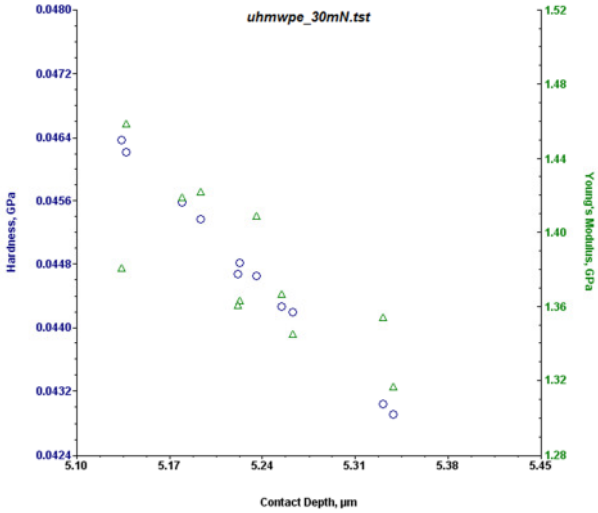

(b) The hardness and Young´s Modulus as a function of indentation contact depth for UHMWPE

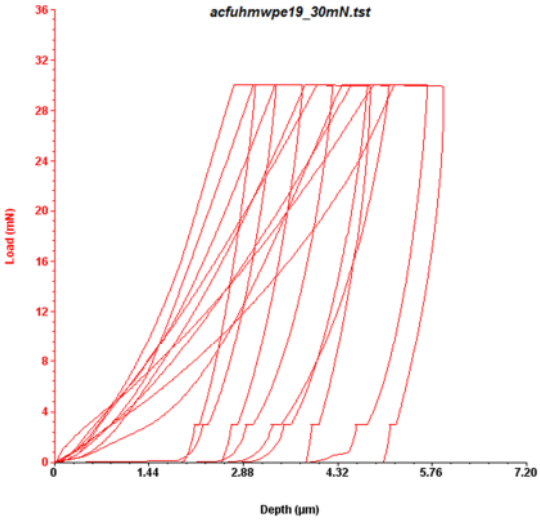

(c) ACFUHMWPE 10wt%

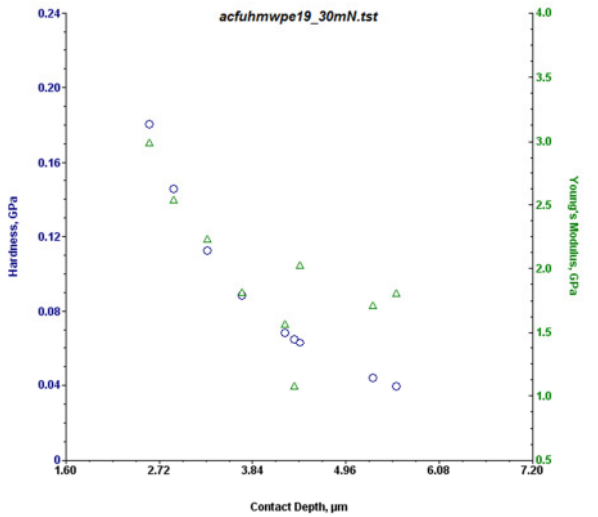

(d) ACFUHMWPE 10wt%

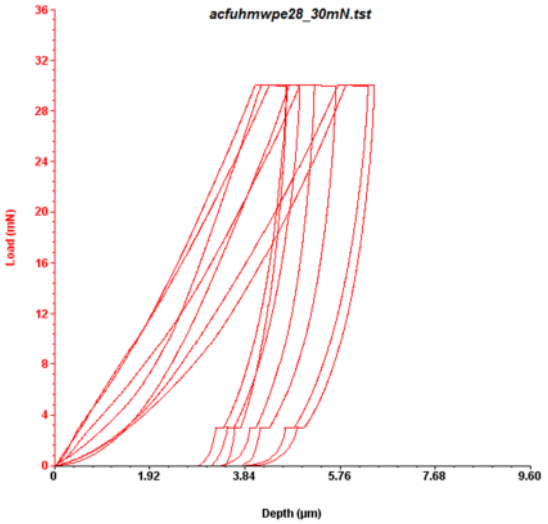

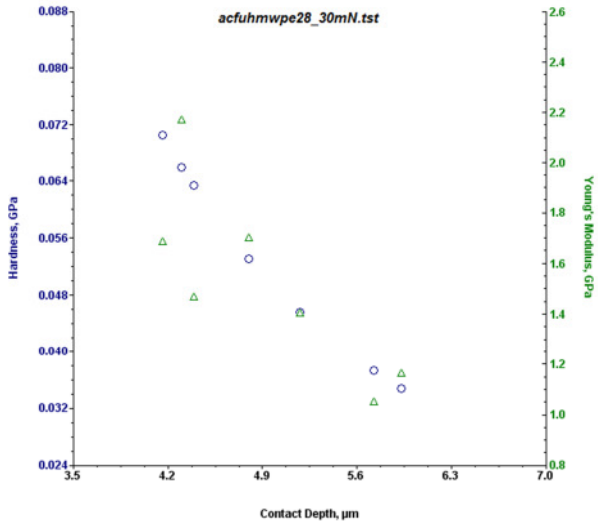

(e) ACFUHMWPE 20wt%

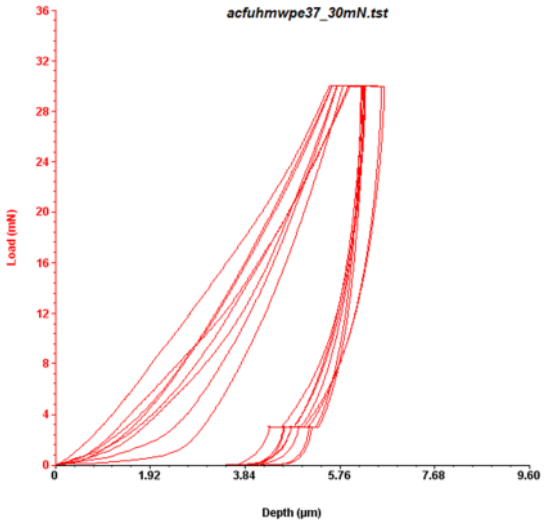

(f) ACFUHMWPE 20wt%

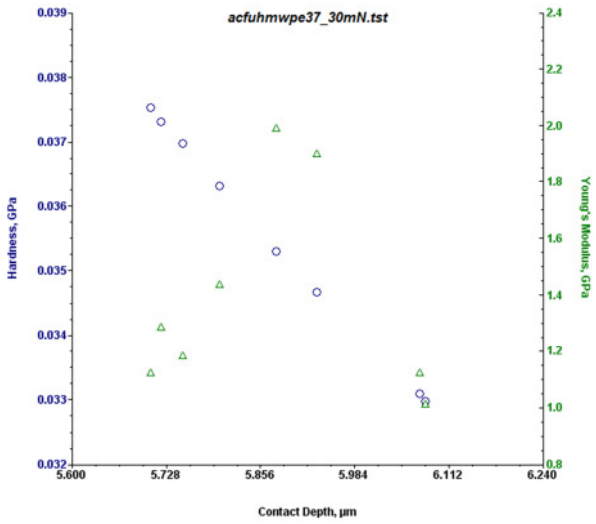

(g) ACFUHMWPE 30wt%

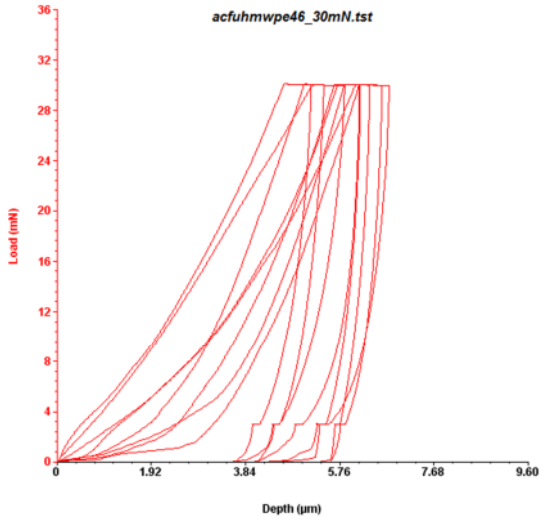

(h) ACFUHMWPE 30wt%

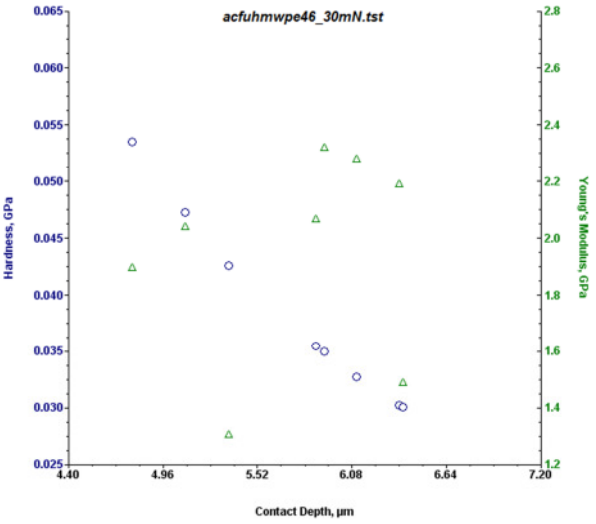

(i) ACFUHMWPE 40wt%

(j) ACFUHMWPE 40wt%

Figure 5. 12 shows on the left side the load-displacement curves of indentations made to peak loads of 30mN for: (a) UHMWPE, c) ACFUHMWPE 10wt%, (e) ACFUHMWPE 20wt%, (g) ACFUHMWPE 30wt%, (i) ACFUHMWPE 40wt% and on the right side the hardness H and Young´s modulus E as a function of indentation contact depth for: (b) UHMWPE, (d) ACFUHMWPE 10wt%, (f) ACFUHMWPE 20wt%, (h) ACFUHMWPE 30wt%, (j) ACFUHMWPE 40wt%, respectively.

In case of the ACFUHMWPE composites, the unloading and reloading curves are smooth, however peak load displacements shift to higher values in successive cycles. In addition, there is a thermal drift present in all curves, pictured by a variation of depth at the end of the unloading curve. The relatively large displacement registered just prior to final unloading is due to creep during the 30 s hold period at peak load. ACFUHMWPE 10 wt% and

ACFUHMWPE 40 wt% show larger displacements from 2.7 to 5.7 μm and 3.8 to 6.3 μm, respectively. ACFUHMWPE 20 wt% suffers a smaller displacement from 4.2 to 5.8 μm, whereas ACFUHMWPE 30 wt% registers the smallest displacement of only 0.3 μm, from 5.7 to 6 μm. Thus, it is apparent that at least some plastic deformation occurs in the composites after the initial loading, and some of it is time dependent. Although we included 30 s peak load hold period to allow time dependent plastic effects to diminish and we used the unloading curves obtained after several cycles of loading to minimize effects of reverse plasticity, some nonelastic effects are still present.

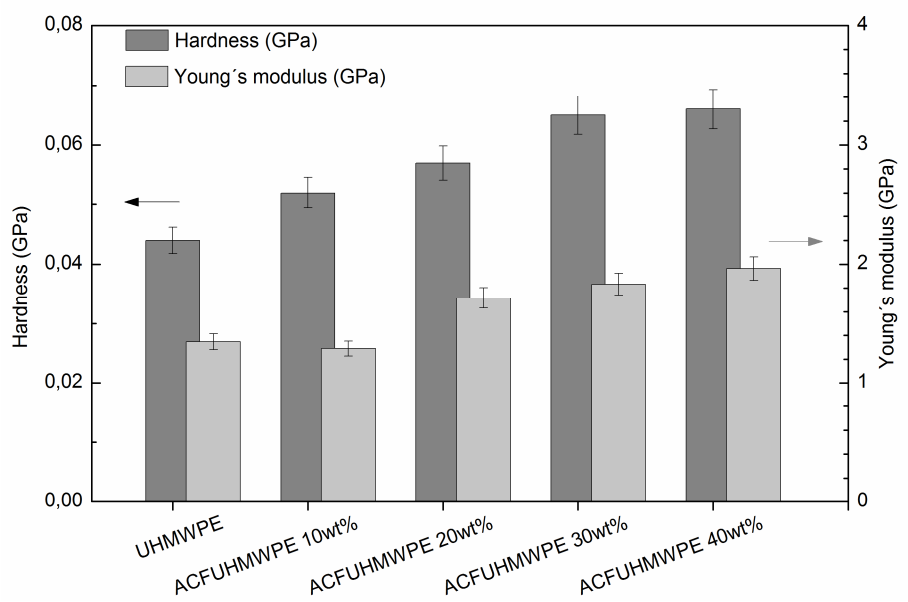

Figure 5. 13 Hardness and Young´s modulus calculated for peak loads of 30mN.

Nanoindentation hardness is defined as the indentation load divided by the projected contact area of the indentation. It is the mean pressure that a material will support under load. From the load-displacement curve, the hardness can be obtained at the peak load as:

$$H = \frac{P_{max}}{A} \tag{5. 4}$$

where A is the projected contact area.

The nanoindentation elastic modulus was calculated using the Oliver-Pharr data analysis procedure [174], beginning with fitting the unloading curve to a power-law relation. The unloading stiffness can be obtained from the slope of the upper portion of the unloading curve, $S = dP/dh$. Measurement of the elastic modulus follows from its relationship to contact area and the measured unloading stiffness through the relation:

$$S = 2\beta\sqrt{\frac{A}{\pi}E_{eff}} \tag{5. 5}$$

Where E_{eff} is the effective elastic modulus defined by:

$$\frac{1}{E_{eff}} = \frac{1-\vartheta^2}{E} + \frac{1-\vartheta_i^2}{E_i} \qquad (5.\ 6)$$

The effective elastic modulus takes into account the fact that elastic displacements occur in both the specimen, with Young´s modulus E and Poisson´s ratio ϑ and the indenter, with elastic constants E_i and ϑ_i.

The calculated hardness and Young´s modulus of the composites for a peak load of 30mN was found to be higher than the initial UHMWPE (H = (44 ± 4) MPa and E = (1,35 ± 0,07) GPa). Hardness gradually increases with the increase of the weight percentage on quasicrystalline filler from H = (52 ± 4,6) MPa for a 10 wt% quasicrystal to (1,35 ± 0,07) GPa for a 40 wt%. The results are shown in the Figure 5. 13. The Young´s modulus E shows a similar tendency, however the value obtained for the ACFUHMWPE 10 wt% (E = 1.29 ± 0,06 GPa) is slightly smaller than UHMWPE (see Figure 5. 13). This increases for the next composites up to (1.97 ± 0,1) GPa.

All the samples exhibit a general decrease in hardness and elastic modulus with increasing indentation depth. A similar behavior has been reported by other research groups [175].

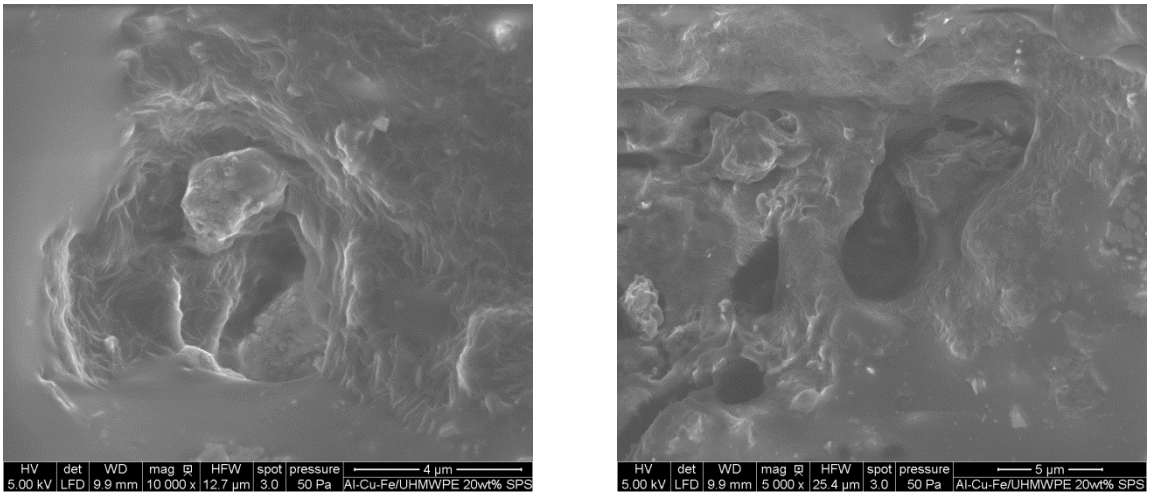

Figure 5. 14 REM image of the indentation induced fragmentation in the vicinity of 36 Berkovich indents on the ACFUHMWPE 20 wt% sintered sample.

When performing nanoindentation tests, the material around the indent breaks into segments which are shifted in height by mutual shearing. This shearing occurs along radial cracks which preferentially propagate in definite crystallographic directions. The increased amount of microcracking may result in fragmentation into individual grains separated by macroscopic defects as depicted in Figure 5. 14. In accordance with the findings of Trebin and Wolf

[37,175] we observe a fragmentation into polygrained material followed by subsequent grain boundary sliding.

It is worth mentioning that these are only preliminary results and their reliability is questionable. It appears that, the classical Oliver-Pharr model used in these measurements does not quite account for our composites which proved to be time-dependent materials, showing viscoelastic and creep behavior. Further measurements should be conducted applying smaller loads (< 30mN) and peak load hold periods higher than 30 s, in order to avoid creep. Also, the thermal drift compensation was not possible due to limitations of the nanoindentation software. The only possibility to minimize the effect of thermal drift would be to make the test very fast (a couple of seconds). However, in this case the E and H results would probably be strongly influenced by creep.

5.4.2 Compression strength tests

Figure 5. 15 shows the true stress as a function of true strain for samples compressed at room temperature. During the deformation we observed an elastic region followed by a large work-hardening region defined by an offset yield point, during which the stress continuously increases with increasing strain. Young´s modulus *E* was calculated from these curves (Figure 5. 16).

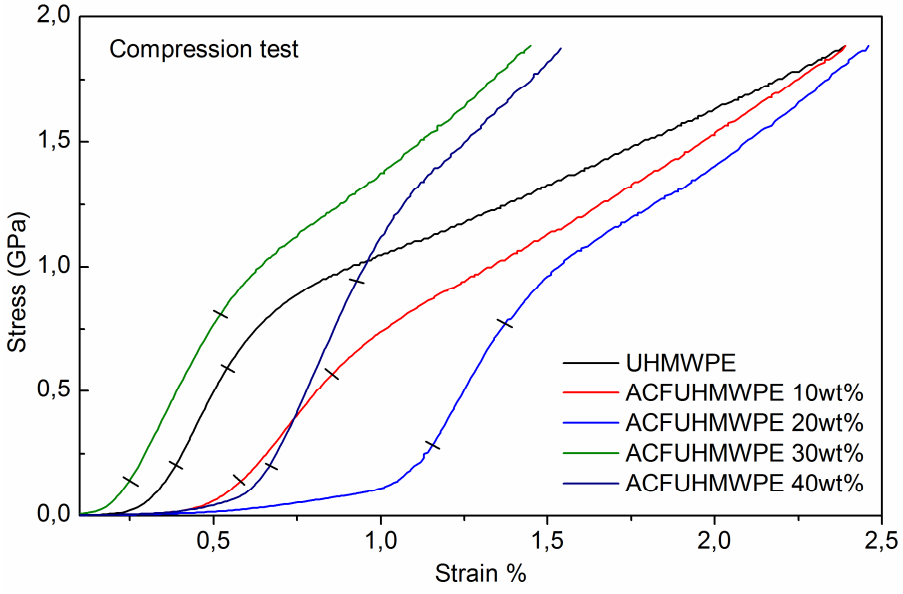

Figure 5. 15 Stress–strain curve showing typical yield behavior for (a) UHMWPE resp (b) ACFUHMWPE composites in uniaxial compression. Stress (σ) is shown as a function of strain (ε). Testing was conducted in air, at room temperature.

The elastic modulus calculated from the stress-strain curves increases with the increase in weight percent filler and is bigger for the composites compared to the pure UHMWPE. The values obtain from the compression tests are slightly smaller as from the nanoindentation measurements. Figure 5. 16 compares the Young´s modulus values obtained from the both methods.

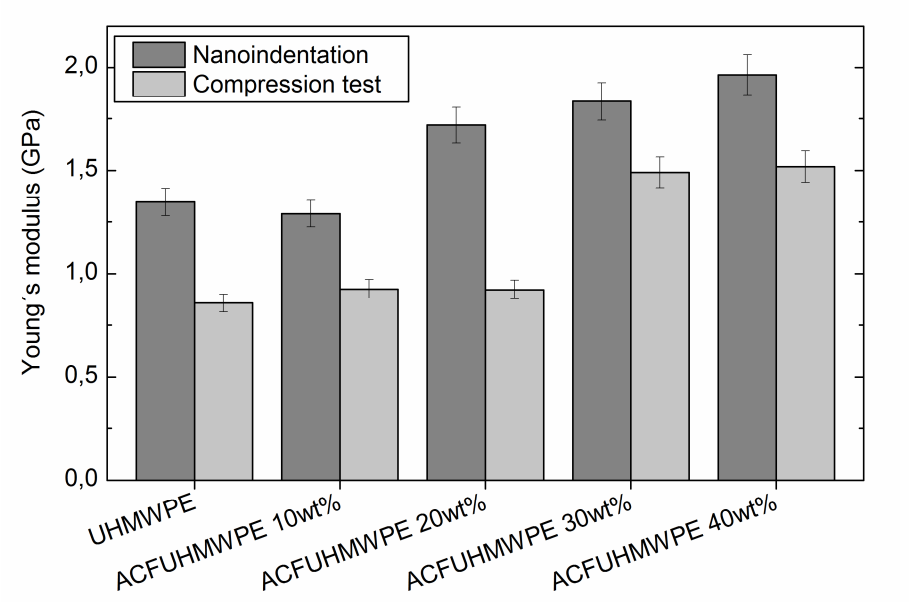

Figure 5. 16 Young´s modulus values for UHMWPE and ACFUHMWPE composites calculated from the compression stress-strain curves and obtained by nanoindentation.

The main aim of this part was to demonstrate that quasicrystalline fillers could significally improve the properties of the UHMWPE used for hip implants. For this purpose, MA followed by SPS processing were employed to synthesis polymer – quasicrystal composites. This aim has been successfully achieved. The MA method proved to be ideally suited for the production of homogeneously dispersed ACF particles in the polymer matrix. Further, the possibility of using SPS technique to process the powders into bulk form suitable for applications testing was discussed. The crystallization behavior of the polymer was studied by DSC and XRD to explain the phase transformation and the crystal growth during heating and therefore, to establish the optimal conditions for the sintering. For this purpose, different heating rates were applied and the changes in the morphological structure as well as the influence of the interphase between the QC particles and the polymer chains were discussed.
The preliminary nanoindentation and compression strength tests proved that the composites are good enhancement materials with improved hardness and elastic modulus.

Chapter 6

Summary and Outlook

Quasicrystals are intermetallic alloys long-range atomic ordered who exhibit intriguing structural characteristics and unusual physical properties contrary to those of their metallic constituents. Since their discovery, many scientists were focused on studying the mechanical alloying process for preparation of high quality quasicrystalline samples suitable for further applications. It was reported that pure quasicrystals can only be synthesized by subsequent annealing. However, the mechanisms of the solid-state reactions involved in this process and the conditions promoting the formation of single-phase QC powders are not clearly described. One great challenge was to resolve the question whether the QC phase forms from disordered metastable phases that can be ordered by the effect of heating of the milled powder or from equilibrium phases through a peritectic reaction. Another aspect was to establish whether a direct route of manufacturing pure quasicrystals by mechanical alloying was possible, in order to eliminate the costly process of melting and rapid solidification.

In order to provide a basis to address these questions, the main part of the thesis focuses on two topics: At first, the evolution of mechanically activated Al-Cu-Fe alloys towards ideal quasicrystals was studied. Different Al-Cu-Fe alloy compositions were analyzed to determine the ideal stoichiometric composition where i-phase remains stable and has sharp diffraction peaks down to room temperature. Secondly, after finding the most suitable composition stoichiometry in the $Al_{67}Cu_{23}Fe_{10}$ alloy we studied the influence of the milling time on the formation of pure icosahedral (i) phase. We have obtained a stable single phase quasicrystal directly by mechanical alloying. Possible mechanisms which could explain the growth of the single icosahedral phase during milling were discussed.

The solid-state transformations were investigated by in-situ high temperature X-ray diffraction (HTXRD) and DSC. Different phase transitions were identified and discussed. The transition temperatures are close to those expected for structural bulk phase transitions. Mechanical properties of sintered pellets by hot pressure (HP), microwave heating (MW) and spark plasma sintering (SPS) were compared and discussed.

The results obtained by DSC and XRD confirmed that the icosahedral phase (i-phase) is formed by a peritectic reaction. A single i-phase can be obtained during heating in all studied compositions except for $Al_{64}Cu_{24}Fe_{12}$. In this composition range, although the i-phase appears between 620 – 700°C, it never develops into a single phase during continuous heating. The longest time pure icosahedral phase remains stable (from 650 – 750°C) is in the $Al_{67}Cu_{23}Fe_{10}$ alloy composition. This is the reason why we have chosen this composition for hot pressing processing and further applications. $Al_{67}Cu_{23}Fe_{10}$ samples have been consolidated by the MW and SPS process and subsequently investigated with respect to their microstructures and mechanical properties. For comparison, appropriate experiments have also been performed by conventional hot pressing (HP). Although it was very difficult to achieve elongated grain morphology in $Al_{67}Cu_{23}Fe_{10}$ alloys by means of the HP or MW process, it was possible to rapidly obtain a complete densificated interlocking microstructure, consisting of elongated grains by SPS processing. The interlocking microstructure is responsible for improved mechanical properties, e.g. SPS compacts exhibiting remarkable increase in the hardness and elastic modulus compared to MW and HP pellets.

The final part of the thesis was focused on the preparation and characterization of quasicrystalline-polymer composites which could be used in biomedical applications. The main aim of this part was to demonstrate that quasicrystalline fillers could significally improve the properties of the UHMWPE used for hip implants. For this purpose, MA was employed to study the possibility of using this novel technique for the formation of good quality ACFUHMWPE composites. This aim has been successfully achieved. The MA method proved to be ideally suited for the production of homogeneously dispersed ACF particles in the polymer matrix, necessary for tailoring the final mechanical properties of these composites. Further, a series of investigations were dedicated to the synthesis and crystallinity behaviour of ACFUHMWPE composites. The crystallization behavior of the polymer was studied by DSC and XRD to explain the phase transformation and the crystal growth during heating and therefore, to establish the optimal conditions for the compacting. Whether the interphase between the QC particles and the polymer plays a role in the overall crystallinity

was discussed. Finally, the possibility of using SPS technique to process the powders into bulk form suitable for applications testing was investigated.

The composites have been demonstrated as excellent enhancement materials, which could find application for example in hip prostheses. Preliminary in vitro tests (presented in the Appendix) showed a good biocompatibility. No metal release was registered after 3 months holding of the samples in body simulating fluid at 37°C.

These field is still in very early stages and it can be noted that the synthesis of polymer-quasicrystalline composites by MA and further SPS processing represent the first of their type. For this reason this work only represents very preliminary studies, which lay the foundation for much possible future research which should involve the following points:

- Clarification of the mechanism variables, such as detailed studies on the effect of the time, ball to powder ratio and rpm in the mechanical alloying process.
- More detail study of the stabilization mechanism in terms of the reduction in interfacial energy. This should combine theoretical calculations, models and predictions with experimental data.
- Investigation of a wider range of quasicrystalline particles, both to show versatility of the synthesis technique and to determine if the nature of the quasicrystalline material forming the filler influences the properties of the end product.
- Further mechanical tests for a complete characterization of the final bulk composites.
- Further in vivo tests for a complete biocompatibility characterization of the ACFUHMWPE composites.

References

[1] D. Shechtman, I. Blech, D. Gratias, and J. W. Cahn, Phys. Rev. Lett. **53**, 1951 (1984).

[2] International Union of Crystallography, Acta Crystallogr. 922 (1992).

[3] A. P. Tsai, *Physical Properties of Quasicrystals* (Springer, Berlin, 1999).

[4] P. Gille, P. Dreier, M. Gräber, and J. Scholpp, J. Crystal. Growth **207**, 95 (1999).

[5] P. Gille, R.-U. Barz, and L. M. Zhang, *Quasicrystals* (John Wiley & Sons, 2003).

[6] M. Feuerbacher, C. Thomas, K. Urban, R. Lück, L. Zhang, R. Sterzel, E. Uhrig, E. Dahlmann, A. Langsdorf, W. Assmus, U. Köster, D. Zander, L. Lyubenova, L. Jastrow, P. Gille, R.-U. Barz, and L. M. Zhang, in edited by D. rer nat H.-R. Trebin (Wiley-VCH Verlag GmbH & Co. KGaA, 2006), pp. 1–87.

[7] P. A. Thiel, A. I. Goldman, and C. J. Jenks, *Physikal Properties of Quasicrystals (Z. M. Stadnik, Ed.)* (Springer, 1999).

[8] K. Urban, M. Feuerbacher, and M. Wollgarten, MRS Bull. **22**, 65 (1997).

[9] A. P. Tsai, H. Suenaga, M. Ohmori, Y. Yokoyama, A. Inoue, and T. Masumoto, Jpn. J. Appl. Phys. **31**, 2530 (1992).

[10] C. J. Jenks and P. A. Thiel, MRS Bull. **22**, 55 (1997).

[11] S. D. Kaloshkin, V. V. Tcherdyntsev, and V. D. Danilov, Crystallogr. Rep. **52**, 953 (2007).

[12] N. S. Cohen, Q. A. Pankhurst, and L. F. Barquín, J. Phys. Condens. Matter **11**, 8839 (1999).

[13] T. F. Grigorieva, S. V. Tsybulya, S. V. Cherepanova, G. N. Kryukova, A. P. Barinova, V. D. Belykh, and V. V. Boldyrev, Inorg. Mater. **36**, 143 (2000).

[14] E. Y. Ivanov, I. G. Konstanchuk, B. D. Bokhonov, and V. V. Boldyrev, React. Solids **7**, 167 (1989).

[15] N. Asahi, T. Maki, T. Kishida, and K. Tatsugawa, J. Non-Cryst. Solids **156–158, Part 2**, 927 (1993).

[16] J. Eckert, L. Schultz, and K. Urban, Mater. Sci. Eng. A **134**, 1389 (1991).

[17] F. Schurack, J. Eckert, and L. Schultz, Nanostructured Mater. **12**, 107 (1999).

[18] J. Eckert, L. Schultz, and K. Urban, Acta Metall. Mater. **39**, 1497 (1991).

[19] V. Srinivas, P. Barua, and B. . Murty, Mater. Sci. Eng. A **294–296**, 65 (2000).

[20] A.-P. Tsai, A. Inoue, and T. Masumoto, J. Mater. Sci. Lett. **7**, 322 (1988).

[21] I. G. Konstanchuk, E. Y. Ivanov, B. B. Bokhonov, and V. V. Boldyrev, J. Alloys Compd. **319**, 290 (2001).

[22] A. Inoue and H. Kimura, Nanostructured Mater. **11**, 221 (1999).

[23] Y.-W. Mai and Y. Y. Yu, *Polymer Nanocomposites* (Woodhead Publishing Limited, Cambridge, England, 2006).

[24] B. C. Anderson, P. D. Bloom, K. G. Baikerikar, V. V. Sheares, and S. K. Mallapragada, Biomaterials **23**, 1761 (2002).

[25] P. D. Bloom, K. . Baikerikar, J. U. Otaigbe, and V. V. Sheares, Mater. Sci. Eng. A **294–296**, 156 (2000).

[26] P. D. Bloom, J. U. Otaigbe, and V. V. Sheares, Proc. Am. Chem. Soc. Div. Polym. Mater. Sci. Eng. **80**, 406 (1999).

[27] **C. Mihoc**, K.-P. Schmitz, and E. Burkel, Biomed. Tech. (Berl) **59**, 59 (2014).

[28] E. Huttunen-Saarivirta, J. Alloys Compd. **363**, 154 (2004).

[29] M. Quiquandon, A. Quivy, J. Devaud, F. Faudot, S. Lefebvre, M. Bessière, and Y. Calvayrac, J. Phys. Condens. Matter **8**, 2487 (1996).

[30] L. M. Zhang, R. Lück, and P. Gille, J. Cryst. Growth **275**, e2077 (2005).

[31] A.-P. Tsai, A. Inoue, and T. Masumoto, Jpn. J. Appl. Phys. **26**, L1505 (1987).

[32] Y. Calvayrac, A. Quivy, M. Bessière, S. Lefebvre, M. Cornier-Quiquandon, and D. Gratias, J. Phys. **51**, 417 (1990).

[33] M. Audier and P. Guyot, in *Proc. Anniv. Adriat. Res. Conf. Quasicrystals*, edited by M. Jaric and S. Lundqvist (World Scientific, Singapore, 1990), pp. 74–91.

[34] A. J. Bradley and H. J. Goldschmidt, J. Inst. Met. **65**, 389 (1939).

[35] P. A. Bancel, in *Quasicrystals* (World Scientific, 1991), pp. 17–55.

[36] N. Bonasso and P. Pigeat, J. Non-Cryst. Solids **334–335**, 509 (2004).

[37] H.-R. Trebin, *Quasicrystals* (Wiley. com, 2006).

[38] **C. Mihoc**, M. Lütgens, E. Burkel, and C. Lathe, An. Rep. HASYLAB DESY (2008).

[39] L. Zhang, J. Schneider, and R. Lück, Intermetallics **13**, 1195 (2005).

[40] D. Gratias, Y. Calvayrac, J. Devaud-Rzepski, F. Faudot, M. Harmelin, A. Quivy, and P. A. Bancel, J. Non-Cryst. Solids **153–154**, 482 (1993).

[41] G. Trambly de Laissardière, D. N. Manh, L. Magaud, J. P. Julien, F. Cyrot-Lackmann, and D. Mayou, Phys. Rev. B **52**, 7920 (1995).

[42] J. W. Cahn, D. Shechtman, and D. Gratias, J. Mater. Res. **1**, 13 (1986).

[43] N. Sâadi, F. Faudot, D. Gratias, and B. Legendre, in *Proc. 5th Int. Conf. Quasicrystals*, edited by C. Janot and R. Mosseri (World Scientific, Singapore, 1995).

[44] F. Dénoyer, G. Heger, M. Lambert, M. Audier, and P. Guyot, J. Phys. **51**, 651 (1990).

[45] P. A. Bancel, Philos. Mag. Lett. **67**, 43 (1993).

[46] N. Menguy, M. Audier, P. Guyot, and M. Vacher, Philos. Mag. Part B **68**, 595 (1993).

[47] J. L. W. Noell, G. L. Wilkes, D. K. Mohanty, and J. E. McGrath, J. Appl. Polym. Sci. **40**, 1177 (1990).

[48] P. C. LeBaron, Z. Wang, and T. J. Pinnavaia, Appl. Clay Sci. **15**, 11 (1999).

[49] R. A. Vaia, K. D. Jandt, E. J. Kramer, and E. P. Giannelis, Macromolecules **28**, 8080 (1995).

[50] A. R. K. Vishal Singh, J. Appl. Polym. Sci. **90**, 3602 (2003).

[51] W. Chen and X. Tao, Appl. Surf. Sci. **252**, 3547 (2006).

[52] F. Loffredo, L. Quercia, E. Massera, and G. Di Francia, Macromol. Symp. **228**, 139 (2005).

[53] B. K. Kuila and A. K. Nandi, Macromolecules **37**, 8577 (2004).

[54] V. Favier, H. Chanzy, and J. Y. Cavaille, Macromolecules **28**, 6365 (1995).

[55] Z. Zhang, J.-L. Yang, and K. Friedrich, Polymer **45**, 3481 (2004).

[56] Z.-Z. Yu, M. Yang, Q. Zhang, C. Zhao, and Y.-W. Mai, J. Polym. Sci. Part B Polym. Phys. **41**, 1234 (2003).

[57] G.-M. Kim, D.-H. Lee, B. Hoffmann, J. Kressler, and G. Stöppelmann, Polymer **42**, 1095 (2001).

[58] A. K. Kulshreshtha, A. K. Maiti, M. S. Choudhary, and K. V. Rao, J. Appl. Polym. Sci. **99**, 1004 (2006).

[59] P. Dubois and M. Alexandre, Adv. Eng. Mater. **8**, 147 (2006).

[60] D. Homminga, B. Goderis, S. Hoffman, H. Reynaers, and G. Groeninckx, Polymer **46**, 9941 (2005).

[61] J. W. Gilman, S. Bourbigot, J. R. Shields, M. R. Nyden, T. Kashiwagi, R. D. Davis, D. L. Vanderhart, W. Demory, C. A. Wilkie, A. B. Morgan, J. Harris, and R. E. Lyon, J. Mater. Sci. **38**, 4451 (2003).

[62] A. J. Bur, S. C. Roth, and M. McBrearty, Rev. Sci. Instrum. **73**, 2097 (2002).

[63] W. J. D. Shaw, Mater. Sci. Forum **269-272**, 19 (1998).

[64] M. Stranz and U. Köster, Colloid Polym. Sci. **282**, 381 (2004).

[65] A. P. Smith, R. J. Spontak, H. Ade, S. D. Smith, and C. C. Koch, Adv. Mater. **11**, 1277 (1999).

[66] A. Sorrentino, G. Gorrasi, M. Tortora, V. Vittoria, U. Costantino, F. Marmottini, and F. Padella, Polymer **46**, 1601 (2005).

[67] F. Cavalieri, F. Padella, and S. Bourbonneux, Polymer **43**, 1155 (2002).

[68] U. Rauscher, H. Bässler, D. D. C. Bradley, and M. Hennecke, Phys. Rev. B **42**, 9830 (1990).

[69] H. Bässler, M. Gailberger, R. F. Mahrt, J. M. Oberski, and G. Weiser, Synth. Met. **49**, 341 (1992).

[70] B. Azhdar, B. Stenberg, and L. Kari, Polym. Test. **25**, 114 (2006).

[71] V. Y. Petrovsky and Z. S. Rak, J. Eur. Ceram. Soc. **21**, 219 (2001).

[72] Y. Du, S. Li, K. Zhang, and K. Lu, Scr. Mater. **36**, 7 (1997).

[73] G. Huard, R. Angers, M. R. Krishnadev, R. Tremblay, and D. Dubé, Can. Metall. Q. **38**, 193 (1999).

[74] L. Li, M. O. Lai, M. Gupta, B. W. Chua, and A. Osman, J. Mater. Sci. **35**, 5553 (2000).

[75] V. L. JM Torralba, J. Mater. Sci. Lett. **19**, 1509 (2000).

[76] Z. G. Wei, C. Y. Tang, W. B. Lee, L. S. Cui, and D. Z. Yang, Mater. Lett. **32**, 313 (1997).

[77] F. Zhang, W. . Kaczmarek, L. Lu, and M. . Lai, Scr. Mater. **43**, 1097 (2000).

[78] T. M. Wright, S. B. Goodman, H. C. Amstutz, and National Institutes of Health (U.S.), editors, *Implant Wear: The Future of Total Joint Replacement* (American Academy of Orthopaedic Surgeons, Rosemont, Ill., 1996).

[79] H. C. Amstutz, P. Campbell, N. Kossovsky, and I. C. Clarke, Clin. Orthop. 7 (1992).

[80] S. Rastogi, D. R. Lippits, A. E. Terry, and P. J. Lemstra, in *Prog. Underst. Polym. Cryst.*, edited by G. Reiter and G. R. Strobl (Springer Berlin Heidelberg, 2007), pp. 285–327.

[81] C. Kittel, *Introduction to Solid State Physics* (Wiley, 1971).

[82] L. X. He, X. Z. Li, Z. Zhang, and K. H. Kuo, Phys. Rev. Lett. **61**, 1116 (1988).

[83] K. Chattopadhyay, S. Lele, N. Thangaraj, and S. Ranganathan, Acta Metall. **35**, 727 (1987).

[84] C. Janot, *Quasicrystals: A Primer* (Oxford University Press, 2012).

[85] P. Bak, Phys. Rev. Lett. **54**, 1517 (1985).

[86] T. Janssen, Acta Crystallogr. A **42**, 261 (1986).

[87] A. Yamamoto, Acta Crystallogr. A **52**, 509 (1996).

[88] K. J. Franke, Quasicrystal Surfaces: Morphology, Phase Transitions, and Epitaxy, Freie Universität Berlin, n.d.

[89] R. Penrose, Bull. Inst. Math. Appl. **10**, 266 (1974).

[90] N. G. de Brujin, Math. Proc. **A84**, 39 (1981).

[91] C. Y. KK Fung, Phys. Rev. Lett. **56**, 2060 (1986).

[92] A.-P. Tsai, A. Inoue, and T. Masumoto, Mater. Trans. JIM **30**, 150 (1989).

[93] H. Zhang and K. H. Kuo, Scr. Metall. **23**, 355 (1989).

[94] A. L. Mackay, Kristallografiya **26**, 910 (1981).

[95] A. L. Mackay, Physica **114A**, 609 (1982).

[96] K. Chattopadhyay, N. Ravishankar, and R. Goswami, Prog. Cryst. Growth Charact. Mater. **34**, 237 (1997).

[97] W. Steurer, Z. Krist. **190**, 179 (1990).

[98] Z. H. Mai, B. S. Zhang, M. J. Hui, Z. R. Huang, and X. X. Chen, Mater. Sci. Forum **22-24**, 591 (1987).

[99] D. Gratias, J. W. Cahn, and B. Mozer, Phys. Rev. B **38**, 1643 (1988).

[100] A.-P. Tsai, Y. Yokoyama, A. Inoue, and T. Masumoto, Jpn. J. Appl. Phys. **29**, L1161 (1990).

[101] C. Dong, Z. K. Hei, L. B. Wang, Q. H. Song, Y. K. Wu, and K. H. Kuo, Scr. Metall. **20**, 1155 (1986).

[102] K. F. Kelton, P. C. Gibbons, and P. N. Sabes, Phys. Rev. B **38**, 7810 (1988).

[103] Z. Zhang, H. Q. Ye, and K. H. Kuo, Philos. Mag. A **52**, L49 (1985).

[104] K. H. Kuo, Mater. Sci. Forum **22-24**, 131 (1987).

[105] K. H. Kuo, D. S. Zhou, and D. X. Li, Philos. Mag. Lett. **55**, 33 (1987).

[106] S. J. Poon, A. J. Drehman, and K. R. Lawless, Phys. Rev. Lett. **55**, 2324 (1985).

[107] S. Ritsch, H.-U. Nissen, and C. Beeli, Phys. Rev. Lett. **76**, 2507 (1996).

[108] C. L. Henley, V. Elser, and M. Mihalkovič, Z. Für Krist. **216**, 1 (2001).

[109] E. Abe, S. J. Pennycook, and A. P. Tsai, Nature **421**, 347 (2003).

[110] T. C. Lubensky, J. E. S. Socolar, P. J. Steinhardt, P. A. Bancel, and P. A. Heiney, Phys. Rev. Lett. **57**, 1440 (1986).

[111] K. Edagawa, K. Suzuki, and S. Takeuchi, Phys. Rev. Lett. **85**, 1674 (2000).

[112] A. Goldman and R. Kelton, Rev. Mod. Phys. **65**, 213 (1993).

[113] M. Windisch, J. Hafner, M. Krajčí, and M. Mihalkovič, Phys. Rev. B **49**, 8701 (1994).

[114] M. Krajčí, M. Windisch, J. Hafner, G. Kresse, and M. Mihalkovič, Phys. Rev. B **51**, 17355 (1995).

[115] J. Hafner and M. Krajčí, *Physical Properties of Quasicrystals* (Springer, 1999).

[116] M. Cornier-Quiquandon, A. Quivy, S. Lefebvre, E. Elkaim, G. Heger, A. Katz, and D. Gratias, Phys. Rev. B **44**, 2071 (1991).

[117] F. Semadeni, N. Baluc, and J. Bonneville, Mater. Sci. Eng. A **234–236**, 291 (1997).

[118] E. Giacometti, N. Baluc, and J. Bonneville, Philos. Mag. Lett. **79**, 1 (1999).

[119] E. Giacometti, N. Baluc, and J. Bonneville, Mater. Sci. Eng. A **294–296**, 777 (2000).

[120] E. Giacometti, P. Guyot, N. Baluc, and J. Bonneville, Mater. Sci. Eng. A **319–321**, 429 (2001).

[121] P. Guyot and G. Canova, Philos. Mag. A **79**, 2815 (1999).

[122] X. Zhang, R. M. Stroud, J. L. Libbert, and K. F. Kelton, Philos. Mag. Part B **70**, 927 (1994).

[123] K. F. Kelton and P. C. Gibbons, Mater. Res. Soc. Bull. **22**, 69 (1997).

[124] M. F. Besser and T. Eisenhammer, MRS Bull. **22**, 59 (1997).

[125] J. Kong, C. Zhou, S. Gong, and H. Xu, Surf. Coat. Technol. **165**, 281 (2003).

[126] A. P. Tsai, K. Aoki, A. Inoue, and T. Masumoto, J. Mater. Res. **8**, 5 (1993).

[127] S. Lee, J. Jung, E. Fleury, W. Kim, and D. Kim, Mater. Sci. Eng. A **294–296**, 99 (2000).

[128] E. Fleury, S. M. Lee, G. Choi, W. T. Kim, and D. H. Kim, J. Mater. Sci. **36**, 963 (2001).

[129] B. Montanari and R. O. Jones, Chem. Phys. Lett. **272**, 347 (1997).

[130] K. Seki, N. Ueno, U. O. Karlsson, R. Engelhardt, and E.-E. Koch, Chem. Phys. **105**, 247 (1986).

[131] M. Iguchi, H. Tonami, and P. D. T. Kawai, Kolloid-Z. Z. Für Polym. **221**, 28 (1967).

[132] H. W. M., William G; Wulff, John Hayden, *The Structure & Properties of Materials: Volume III, Mechanical Behavior* (Wiley, 1965).

[133] D. D. Dean, D. C. Lohmann, D. V. Sylvia, D. G. Köster, D. Y. Liu, D. Z. Schwartz, and D. B. Boyan, J. Orthop. Res. **19**, 179 (2001).

[134] J. S. Benjamin and T. E. Volin, Metall. Trans. **5**, 1929 (1974).

[135] J. S. Benjamin, Sci. Am. **234**, 40 (1976).

[136] C. Suryanarayana, Prog. Mater. Sci. **46**, 1 (2001).

[137] Z. Shen, Z. Zhao, H. Peng, and M. Nygren, Nature **417**, 266 (2002).

[138] M. Nygren and Z. Shen, Solid State Sci. **5**, 125 (2003).

[139] R. S. Mishra, S. H. Risbud, and A. K. Mukherjee, J. Mater. Res. **13**, 86 (1998).

[140] M. Tokita, in *Pulse Electr. Curr. Synth. Process. Mater.*, edited by Z. A. Munir, nshi Ohyanagi, sao Tokita, M. Khor, T. Hirai, and U. Anselmi-Tamburini (John Wiley & Sons, Inc., 2006), pp. 51–59.

[141] M. Nygren and Z. Shen, Key Eng. Mater. Euro Ceramics VIII, 719 (2004).

[142] W. H. Sutton, Am. Ceram. Soc. Bull. **68**, 376 (1989).

[143] Y. V. Bykov, K. I. Rybakov, and V. E. Semenov, J. Phys. Appl. Phys. **34**, R55 (2001).

[144] S. Vaucher, R. Nicula, J.-M. Català-Civera, B. Schmitt, and B. Patterson, J. Mater. Res. **23**, 170 (2008).

[145] **C. Mihoc**, D. Schick, M. Lütgens, C. Lathe, and E. Burkel, Int. J. Mat. Res. **103,** 1341 (2013).

[146] D. Schick, *Processing of Polymer-Metal Composites with Microwaves* (2009).

[147] H. Krischner, *Einführung in Die Röntgenfeinstrukturanalyse* (Vieweg, 1980).

[148] R. Bouchard, D. Hupfeld, T. Lippmann, J. Neuefeind, H. B. Neumann, H. F. Poulsen, U. Rütt, T. Schmidt, J. R. Schneider, J. Süssenbach, and M. von Zimmermann, J. Synchrotron Radiat. **5**, 90 (1998).

[149] U. Hahn, Hasylab Annu. Rep. 143 (1993).

[150] J. I. Langford and D. Louër, Rep. Prog. Phys. **59**, 131 (1996).

[151] R. A. Young, International Union of Crystallography, Commission on Powder Diffraction, and Netherlands Energy Research Foundation, editors, *The Rietveld Method: International Workshop: Papers* (Oxf. U. P., 1993).

[152] M. Knapp, *Weiterentwicklung Und Anwendung Difraktometrischer Methoden Zur Materialcharakterisierung Mit Synchrotronstrahlung*, TU-Darmstadt, 2002.

[153] M. Knapp, C. Baehtz, H. Ehrenberg, and H. Fuess, J. Synchrotron Radiat. **11**, 328 (2004).

[154] G. Caglioti, A. Paoletti, and F. P. Ricci, Nucl. Instrum. **3**, 223 (1958).

[155] P. Scherrer, Gött. Nachrichten **2**, 98 (1918).

[156] *PeakFit for Windows User's Manual* (SPSS Science Inc., n.d.).

[157] G. L. Chiarotti, R. J. Hemley, M. Bernasconi, and L. Ulivi, *High Pressure Phenomena* (IOS Press, Amsterdam, 2002).

[158] M. E. Stir, Structure and Dynamics of Amorphous and Nanostructured Materials, 2004.

[159] J. S. Olsen, B. Buras, L. Gerward, and S. Steenstrup, J. Phys. E **14**, 1154 (1981).

[160] E. F. Skelton, S. B. Qadri, A. W. Webb, C. W. Lee, and J. P. Kirkland, Rev. Sci. Instrum. **54**, 403 (1983).

[161] B. Buras and L. Gerward, Prog. Cryst. Growth Charact. **18**, 93 (1989).

[162] A. I. Salimon, A. M. Korsunsky, E. V. Shelekhov, T. A. Sviridova, S. D. Kaloshkin, V. S. Tcherdyntsev, and Y. V. Baldokhin, Acta Mater. **49**, 1821 (2001).

[163] V. V. Tcherdyntsev, S. D. Kaloshkin, A. I. Salimon, I. A. Tomilin, and A. M. Korsunsky, J. Non-Cryst. Solids **312-314**, 522 (2002).

[164] L. Kaufman, MRS Online Proc. Libr. **19**, null (1982).

[165] S. D. Kaloshkin, I. A. Tomilin, G. A. Andrianov, U. V. Baldokhin, and E. V. Shelekhov, *Phase Transformations and Hyperfine Interactions in Mechanically Alloyed Fe-Cu Solid Solutions* (1997).

[166] V. V. Tcherdyntsev, S. D. Kaloshkin, E. V. Shelekhov, G. Principi, and A. O. Rodin, in *J. Phys. Conf. Ser.* (2008).

[167] F. F. Lange, J. Am. Ceram. Soc. **56**, 518 (1973).

[168] **C. Mihoc**, E. Burkel, and J. Bednarcik, An. Rep. HASYLAB DESY (2010).

[169] T. Seto, T. Hara, and K. Tanaka, Jpn. J. Appl. Phys. **7**, 31 (1968).

[170] T. Y. Cho, B. Heck, and G. Strobl, Colloid Polym. Sci. **282**, 825 (2004).

[171] D. Barron and C. Birkinshaw, Polymer **49**, 3111 (2008).

[172] A. Toda, M. Hikosaka, and K. Yamada, Polymer **43**, 1667 (2002).

[173] H. D. Keith and F. J. P. Jr, J. Appl. Phys. **34**, 2409 (1963).

[174] W. C. Oliver and G. M. Pharr, J. Mat. Res. **7**, 1564 (1992).

[175] B. Wolf, M. Swain, M. Kempf, and P. Paufler, J. Mater. Sci. **35**, 723 (2000).

Appendix A

A.1 Biocompatibility test procedure

There are two general methods to performs biocompatibility tests: *in vitro* (in laboratory glassware), and *in vivo* (in a live animal or human). The usual procedure starts with *in vitro* tests which can weed out the clearly dangerous, but may not expose all problems that may occur in the complex living system. Then some animal tests are required before the implant moves to a human test stage. In this work, only the in vitro tests were covered. The biocompatibility was tested at the Biology Faculty of the University of Rostock (Dr. Margareta Lantow). The procedure used is described below:

Test media (chemicals)

RPMI 1640 + 2 mM L-glutamine culture medium, Fura Red and the *Live/death* Kit were obtained from Invitrogen GmbH (Karlsruhe, Germany); fetal calf serum (FCS) was acquired from Biochrome KG (Berlin, Germany). Nonessential amino acids, penicillin and streptomycin, phosphate buffer saline (PBS) were supplied from PAA Laboratories (Coelbe, Germany). Hepes, Tris, calcium chloride, magnesium chloride, potassium chloride, ethylene diamine tetra-acetic acid (EDTA), sodium chloride, sodium sulfate, sodium hydrogen carbonate, dipotassium phosphate, acetic acide, potassium dodecylsulfat (SDS), 3-(4,5-dimethylthiazol-2-yl)-2,5-diphenyltetrazolium bromide (MTT) were acquired from Carl Roth (Karlsruhe, Germany). Phorbol 12 myristate-13 acetate (PMA), dimethylsulfoxid (DMSO), Hoechst 33258 and trypan blue were supplied from Sigma-Aldrich (Munich, Germany). Caffeine was purchased from Calbiochem (USA). Prolong gold antifade reagent was purchased from Invitrogen (Karlsruhe, Germany). StemTAG™ Alkaline Phosphatase Staining Kit was acquired from BioCat GmbH (Heidelberg, Germany).

Culture of human MG63 osteoblastic like cells

Cells (kindly provided by Dr. Ralf Kriehuber, Germany) were cultured at 37°C and in humidified atmosphere of 5% CO_2 in air in RPMI 1640+2 mM L-glutamine culture medium supplemented with 10% heat-inactivated FCS, 2% nonessential amino acids and 1% penicillin and streptomycin. Cells were maintained in 75 cm^2 flasks (TPP, Germany) at a density of 1,5 X 10^6 cells/ml. All experiments were carried out with cells (5 X 10^5/ml) that were seeded in 24, 96-well plates (TPP, Germany) or in Lab-Tek chambered cover glasses (8 wells; Nunc, Germany) 24 h before starting experiments.

Cellular growth and viability

Cellular growth was monitored during one week by cell counting and cellular viability was determined using the Trypan Blue exclusion assay. Cellular growth an viability were determined after 24, 48, 72 and 96 h exposure of cells (5 x 10^5/ml density) in 24-well plates (TPP, Germany) to different nanostructured quasicrystalline Al-Cu-Fe particles and UHMWPE polymers or chemicals (1 µM PMA, 10 mM caffeine). Results were expressed as mean of number of cell or percent of viability ± SD from 4 independent experiments performed in duplicates.

Mitochondrial dehydrogenases activity

Mitochondrial dehydrogenases activity was evaluated using the colorimetric MTT assay (modified after Mosmann et al., 1983), (Mosmann, 1983) after 24 h exposure of cells (5 x 10^5/ml density) in 96-well plates (TPP, Germany) to different nanostructured quasicrystalline Al-Cu-Fe particles and UHMWPE polymers or chemicals (1 µM PMA, 10 mM caffeine). After 24 h exposure 20 µl sterile MTT solution (5 mg/ml, filtered through a 0.22 µm filter) was added to each sample (0.5 mg/mL final concentration) for 2 h. After centrifugation the supernatant was removed and 100 µL of DMSO supplemented with 10% SDS and 0.6% acetic acid was added to each sample to solubilize resulted formazan crystals. Optical density was measured at 550 nm using the EL808 Ultra Microplate Reader (BioTek Instruments, Winooski, USA). Results were expressed as percentage of mitochondrial dehydrogenases activity compared to control from 6 independent experiments with six parallels.

LIVE/DEAD Viability/Cytotoxicity Assay

Calcein AM (4 µM) and ethidium homodimer-1 (8 µM) labelling of cells (30 min in the dark) was performed after exposure of cells to different ratios of nanostructured quasicrystalline Al-

Cu-Fe particles and UHMWPE polymers in 24-well plates (TPP, Germany). Calcein AM (CAM) is a fluorogenic esterase substrate that is hydrolyzed to a green-fluorescent product thus; green fluorescence is an indicator of cells that have esterase activity as well as an intact membrane to retain the esterase products. Ethidium homodimer-1 (EthD-1) is a high-affinity, red-fluorescent nucleic acid stain that is only able to pass through the compromised membranes of dead cells. After labelling the cell suspension was analyzed by flow cytometry (Epics Altra, EXPO32 vs. 1.2 analysis software; Beckman Coulter), gated at 10000 cells, at an excitation wavelength of 488 nm. The CAM green fluorescent dye, taken up by living cells, emitted at 530 nm, while the EthD-1 red fluorescent dye, taken up by the dead cells, emitted at 610 nm. Results were expressed as mean of CAM positive (living cells) and EthD-1 positive (death cells) cells (in percent) ± SD from 4 independent experiments.

Cytosolic calcium detection

Cytosolic Ca^{2+} released from intracellular stores was evaluated through confocal laser scanning microcopy (TCS SP2 AOBS, Leica, Germany). After 24 h treatment of cells with different polymer composites (10 µg/cm^2) or caffeine (10 mM) in Lab-Tek chambered cover glasses (8 wells; Nunc, Germany) cells (5×10^5) were stained with the high-affinity fluorescent Ca^{2+} indicator Fura Red (20 µM) and Hoechst 33258 (1.9 µM) for 30 min. A UV laser allowed excitation of Hoechst-stained nuclei at a wavelength of λ=351 nm.

Signal/noise ratio of the images was increased using line and frame averaging (4 and 4, respectively). Hoechst 33258 staining helped for cell and nuclei identification within microscopic fields using a 351 nm UV laser (emission at 410-590 nm wavelengths). Fura Red was detected using an 488 nm Argon-Krypton laser and photomultiplier detection ranges for emission wavelengths were set at 650-800 nm. First for qualitative comparison of calcium changes, 3D XYZ-scans were achieved. The confocal laser scanning parameters were kept constant for all experiments, as following for Fura Red and Hoechst 33258 respectively: zoom factor = 1; gains = 660 and 640 V; pinhole sizes = 1 and 0.3 airy units; laser intensities = 29 and 68%; confocal sections = 20 stacks. Region of interest (ROIs, i.e. cell contours) were set for each cell based on Fura Red fluorescence intensities (mFI) using Leica Confocal Software (Leica, Mannheim, Germany). ROIs permitted to measure changes of mean fluoresce intensities. For each image (512x512 pixels) the background fluorescence was measured (i.e. ROIs without cells) and subtracted from the mFI which were normalized afterwards. For Fura Red, an increase of Ca^{2+} level results in a decrease of fluorescence emission due to binding of

Ca^{2+} (i.e. reduction of Ca^{2+}–free form amount) (Liu and Persson, 2005). After background fluorescence subtraction and normalization data were expressed as mean ± SD from 3 independent experiments.

Alkaline phosphatase staining

Alkaline phosphatase (AP) activity was determined using the StemTAG™ Alkaline Phosphatase Staining Kit according to the manufacturer's protocol. Shortly, to determine AP activity cells were growth on cover glasses and in 24 well plates (TPP, Germany) and exposed to different nanostructured quasicrystalline Al-Cu-Fe particles and UHMWPE polymers or vitamin C (120 μM) for 24, 48, 72 and 96 h. After exposure, the medium was gently aspired and cells were washed with PBS. Following, the wash solution was removed and fixing solution was added to the cells and incubated at room temperature for 2 minutes. Fixed cells were twice washed with PBS and incubated with freshly prepared StemTAG™ AP Staining Solution for 15-30 minutes, protected from light at room temperature. After removing the AP staining solution cells were washed twice with PBS and for long-term storage were mounted overnight on glass slides (Menzel, Germany) using Prolong gold antifade reagent. Red stained (undifferentiated cells) and colorless cells (differentiated cells) were visualized and analyzed using a confocal laser scanning microscope (TCS SP2 AOBS, Leica, Germany) and Leica Confocal Software (Leica, Mannheim, Germany) from 4 independent experiments.

Biocompatibility test

To evaluate composite polymers biocompatibility and stability they were incubated in simulating body fluid (SBF, according to (Kokubo and Takadama, 2006) which has ion concentrations nearly equal to those of human blood plasma. Therefore polymers were incubated in 50 ml tissue culture tubes (TPP, Germany) in SBF at 37°C, 5% CO_2, 120 rpm for 1 and 3 months in an incubator shaker (Controlled Environment Incubator Shaker, New Brunswick Scientific Co. Inc., Germany). Following, polymers were dried at room temperature and their weight was determined. The SBF was analyzed for each polymer and the tracks of Al, Cu and Fe were determined using the IRIS INTREPID II spectrophotometer (Thermo Fisher, Schwerte, Germany) from 3 independent experiments.

Statistical analysis

All experiments were carried out with cells (5 x 10^5/ml density) that were seeded in incubator 24 h before starting experiments at 37 °C, 5% CO_2 in air. The obtained data were expressed as

mean value ± standard deviation (SD) from at least 3-6 independent experiments with 2-6 parallels. Statistical differences between the means were determined using a two-tailed paired Student's t-test and analysis of variance (ANOVA) followed by the Dunnett´s multiple comparison post hoc tests. Values of $P < 0.05$ were considered as significantly different from the respective control.

Metal analysis

For studying the release of the metals into solution, their concentrations were measured in the extracts by inductively coupled plasma-optical emission spectroscopy (ICP-OES) using an Iris Intrepid II spectrometer equipped with a CID detector. The operating parameters and analytical line wavelengths chosen for the measurements were typical. To ensure high-quality trace metal detection, a blank sample of body simulation fluid was used for correction of analytical signals measured by ICP-OES. The detection limit was 0.01 mg/L. Since the copper an iron concentrations of the samples was generally below the detection limit, these contributions were not taken into account.

A.2 Biocompatibility test results

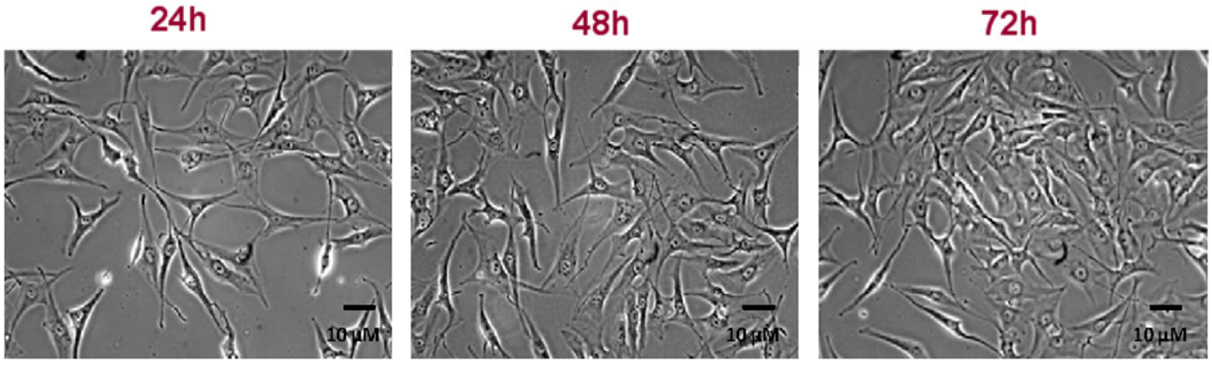

Figure 1 Human MG63 osteoblast-like cell line: present the phenotypic characteristic of osteoblastic cells cultured at 37°C in a humidified atmosphere of 5% CO_2.

Mitochondrial dehydrogenases activity was measured using the MTT assay with 3-(4,5-dimethylthiazol-2-yl)-2,5-diphenyltetrazolium bromide by photometry (ELISA reader, EL808, Ultra Microplate Reader, Bio-Tech Instruments, INC) at 550 nm. The results were expressed as percentage viability compared to control.

Cytosolic calcium released from intracellular stores was evaluated through confocal laser scanning microcopy (TCS SP2 AOBS, Leica, Germany).

After 24 h treatment of cells with different polymer composites, the cells were stained with the high-affinity fluorescent Ca^{2+} indicator Fura Red (20 µM) and Hoechst 33258 (1.9 µM).

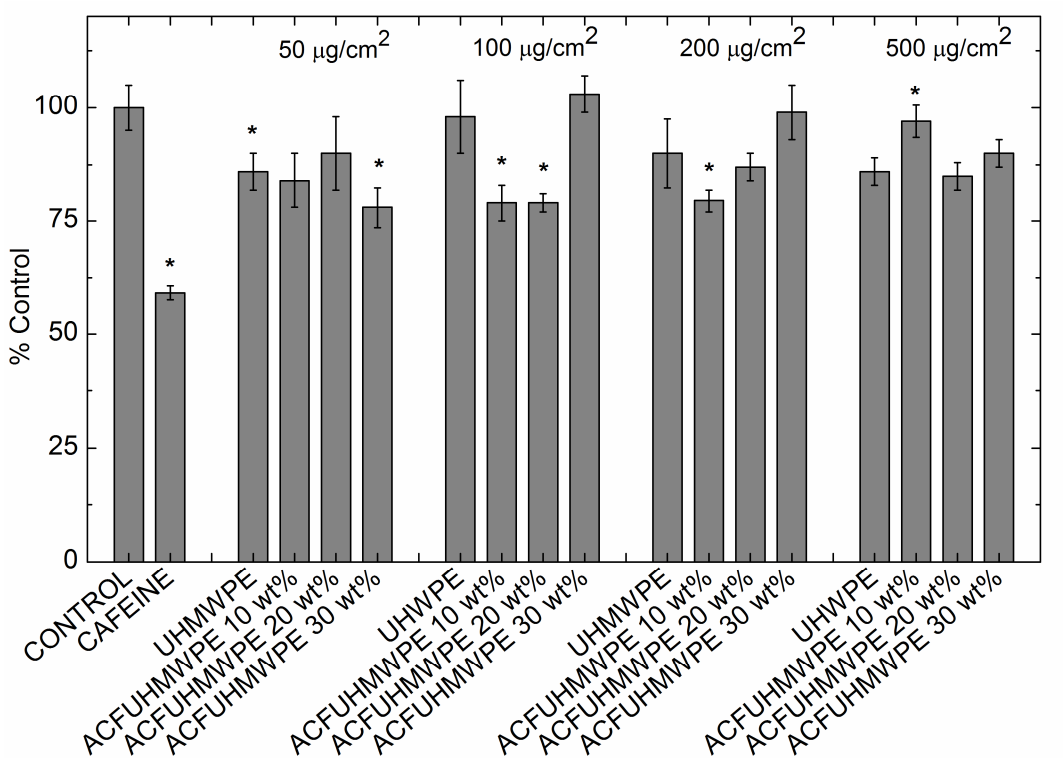

Figure 2 Mitochondrial dehydrogenase activity after 24 h treatment of cells with different weight ratio combinations and concentrations (50, 100, 200 and 500 µg/cm^2) of Al-Cu-Fe nanostructured quasicrystalline particles and UHMWPE (10:90, 20:80 and 30:70) in comparison with UHMWPE or caffeine (10 mM) treatments. Diagram shows the mean data of 6 independent experiments with six parallels ± SD. *statistically significant differences compared to control using a two-tailed paired Student's t-test, *P<0.05.

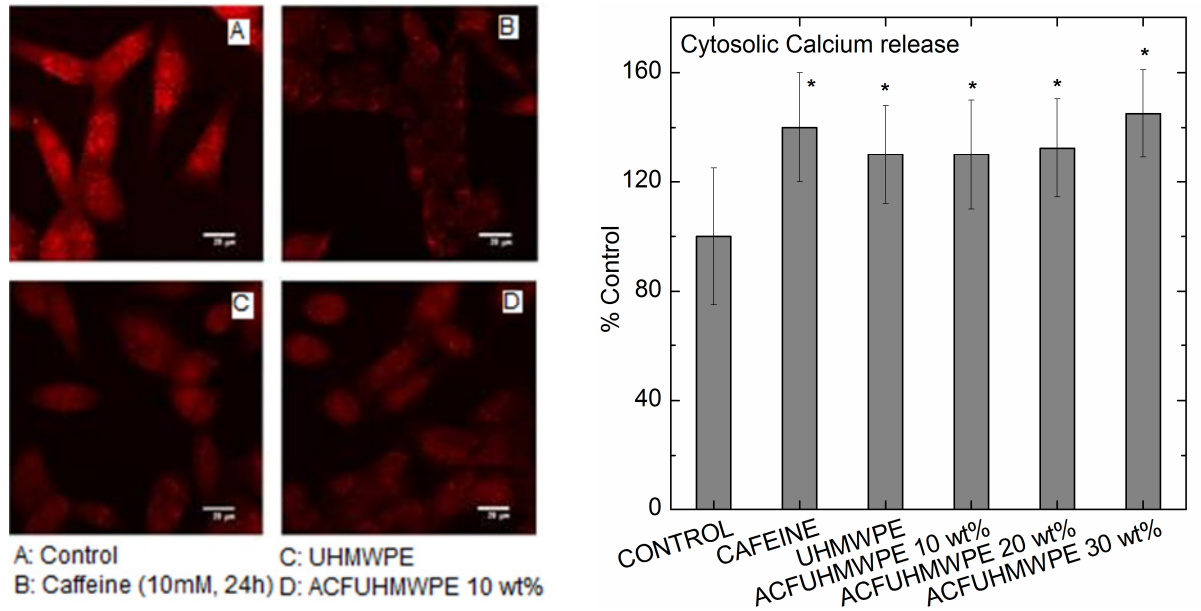

Figure 3 Cytosolic calcium release detected by confocal laser scanning microcopy after 24 h treatment of cells with different weight ratio combinations of Al-Cu-Fe nanostructured quasicrystalline particles and UHMWPE (10:90, 20:80 and 30:70, 100 µg/cm^2) in comparison with UHMWPE or caffeine (10 mM) treatments. Cells were stained with the high-affinity fluorescent Ca2+ indicator Fura Red (red), Hoechst 33258 (blue) (XA). Histograms show the mean data of 3 independent experiments ± SD. *statistically significant differences compared to control using a two-tailed paired Student's t-test and ANOVA, *P<0.05, **P<0.01, ***P<0.001 (XB).

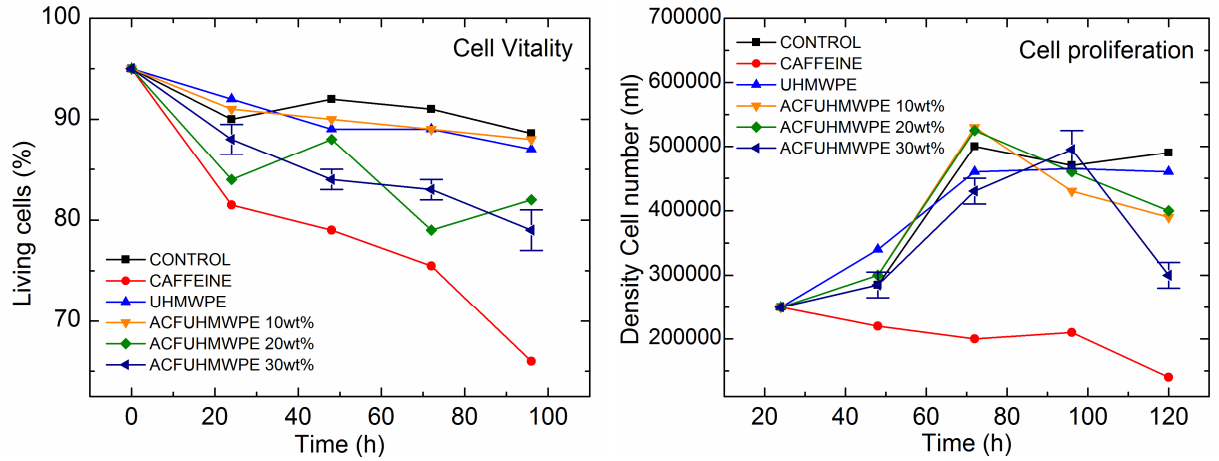

Figure 4 Cellular vitality and growth and after 24 h treatment of cells with different weight ratio combinations of Al-Cu-Fe nanostructured quasicrystalline particles and UHMWPE (10:90, 20:80 and 30:70, 100 µg/cm2) in comparison with UHMWPE or caffeine (10 mM) treatments. Curves show the mean data of 4 independent experiments ± SD.

Metal release results

The fundamental requirements for implant materials with metallic content are high chemical and physical resistance to biodegradation in the human body over a long time. Our biotests were carried out for 3 months. The precision of the measurements was investigated via analysis of six sub-samples in each run; relative standard deviations varied from 1% to 15%.
Metal releases from the Al-Cu-Fe alloy encapsulated in the UHMWPE matrix into the solution simulating human body conditions were investigated and the concentration of the Al, Cu and Fe was measured.
A comparison of the metal extraction efficiencies for 1 month and 3 months was conducted. Figure 5 shows a compilation of the Al elemental concentration determinations in different samples. The results were comparable and reproducible for all the samples and showed no metal release in solution. The corresponding total Cu an Fe concentrations registered for all the samples were found to be smaller than the detection limit (<0,01 mg/l).

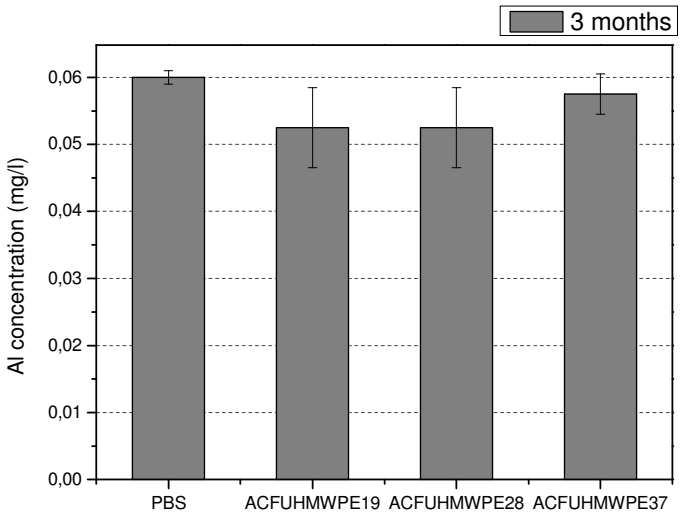

Figure 5 Comparison of the Al concentration from different composites after 3 months immersion in PBS solution.

The used composite materials presented no changes (weight loss) during the incubation period in the simulating body fluid, showing at least their short term biocompatibility. Cellular growth and viability were not affected by the composite materials. Mitochondrial activity was not affected after 24h exposure of cells to the polymer composites (50-500 µg/cm^2). Caffeine treatment of cells induced a significant decrease of mitochondrial activity after 24h exposure. On the other hand, cellular growth, cytosolic calcium level and cellular viability were significantly increased after short term caffeine treatment of cells. All tested composite

materials induced a significant increase of cytosolic calcium level. The Al-Cu-Fe quasicrystals/UHMWPE composites showed a higher induction of the calcium release compared to their respective polyethylene polymers. In conclusion, our data indicate a good biocompatibility of the tested composite materials after short term exposure with a stimulating effect on intracellular calcium release in human MG63 osteoblast-like cells.

Liste der Veröffentlichungen

Publikationen

1. **C. Mihoc**, K.-P. Schmitz, E. Burkel, „Ultrahigh molecular weight polyethylene reinforced with quasicrystalline particles for biomedical applications“, Biomed. Tech. **59,** 42 (2014).
2. **C. Mihoc**, D. Schick, M. Lütgens, C. Lathe, and E. Burkel, „Formation of $Al_{67}Cu_{23}Fe_{10}$ quasicrystals by microwave heating“, Int. J. Mat. Res. **103,** 1341 (2013).
3. **C. Mihoc**, E. Burkel and J.Bednarcik, „Hard X-ray diffraction studies on the quasicrystal phase formation in Al-Cu-Fe alloys by field activated sintering“, An. Rep. HASYLAB DESY (2010).
4. **C. Mihoc**, M. Lütgens, E. Burkel and C. Lathe, „In Situ Energy Dispersive X-Ray Diffraction Analysis of the Temperature-Pressure Stability of Al-Cu-Fe alloys“, An. Rep. HASYLAB DESY (2008).
5. F. Zhang, **C. Mihoc**, F. Ahmed, C. Lathe, E. Burkel, „Thermal stability of carbon nanotubes, fullerene and graphite under spark plasma sintering“, Chem. Phys. Lett. 510 (2011) 109.

Konferenzbeiträge

1. **C. Mihoc**, D. Schick, E. Burkel „Crystallization studies on Quasicrystal/Polymer nanocomposites“ Poster, 11th Lähnwitzseminar on Calorimetry, 6-11 June 2010, Rostock, Deutschland.
2. M. Lantow, T. Rharass, J. Markhoff, **C. Mihoc**, D. Weiss, E. Burkel, „Biocompatibility Tests on Quasicrystal-Ultrahigh Molecular Weight Polyethylene (UHMWPE) Composites in Human MG63 Osteoblast-Like Cell Cultures“ Poster, 6th International Congress and Exhibition on Nanotechnology, 15-17 June 2010, Münster, Deutschland.
3. **C. Mihoc**, D. Schick, E. Burkel, „Synthesis, microstructure and properties of Al-Cu-Fe/UHMWPE composites“ Poster, 13th Symposium on Layered Nanostructures: Polymers with Improved Properties, 12-13 May 2009, Wittenberg, Deutschland.

4. **C. Mihoc**, „Formation and characterization of quasicrystalline aluminium alloys“ Lecture, IPP and Advatec Seminar, Universität Rostock, 12 December 2008, Rostock, Deutschland.
5. **C. Mihoc**, R. Nicula, M. Stir, E. Burkel „Synthesis and thermal analysis of Al-based nanopowders“ Poster, 10th Lähnwitzseminar on Calorimetry, 8-13 June 2008, Rostock, Deutschland.
6. **C. Mihoc**, R. Nicula, M. Stir, E. Otterstein, E. Burkel, „Synthesis and characterization of QC/UHMWPE nanocomposites“ Poster, First International Conference on Functional Nanocoatings, 30th March – 2nd April 2008, Budapest, Ungarn.
7. **C. Mihoc**, R. Nicula, M. Stir, E. Otterstein, E. Burkel, „Synthesis of Al-Cu-Fe/polymer composites“ Poster, WE-Heraeus-Seminar, „Matter in Coherent Light“, Physikzentrum Bad Honnef, , 17-20 March 2008, Bad Honnef, Deutschland.
8. **C. Mihoc**, R. Nicula, M. Stir, E. Otterstein, E. Burkel, „Synthesis of AlCuFe/polymer composites“ Poster - awarded with 1st place Advanced Processing for Novel Functional Materials (APNF2008) International Conference, 23-25 January 2008, Dresden, Deutschland.
9. **C. Mihoc**, R. Nicula, M. Stir, E. Otterstein, E. Burkel, „Synthesis and characterization of Al-based quasicrystals“ Poster, Trends in Nanotechnology (TNT2007) International Conference, 03-07 September 2007, San Sebastian, Spanien.
10. **C. Mihoc**, R. Nicula, M. Stir, E. Otterstein, E. Burkel, „Synthesis of quasicrystal/polymer composites“ Poster, Marie Curie Summer School, „Knowledge Based Materials“, Partially molten and amorphous materials, 19-29 August 2007, Estremoz, Portugal.

Curriculum Vitae

Carmen Gabriela Mihoc

Personal Information

Date and place of birth	1st November, 1977, Suceava, Romania
Postal address	Augustenstr. 73, 18055 Rostock, Germany
Affiliation, title	Institute of Biomedical Engineering, University of Rostock, MSc.

Education

10/2001– 07/2003	Master of Science, University Al. I. Cuza, Iasi, Romania.
10/1997– 07/2001	Bachelor of Chemistry and Physics, University Al. I. Cuza, Iasi, Romania.
09/1992– 07/1996	High-School Certificate, Gymnasium Stefan cel Mare, Suceava, Romania, Class of Mathematics and Physics.

Work experience

07/2012 – present	Research Associate, Institute for Biomedical Engineering, Medicine Faculty, University of Rostock, Rostock, Germany.
01/2011 – 02/2012	Maternal leave, Rostock, Germany.
12/2006 – 01/2011	Research Associate, Physics of New Materials Department, Physics Institute, University of Rostock, Rostock, Germany. Topic: Low friction thermal barrier coatings based on quasicrystalline Al alloys
02/2006 – 12/2006	Research Associate, Institute of Materials Science of Barcelona (ICMAB), Autonomous University of Barcelona (UAB), Barcelona, Spain. Topic: Synthesis by laser radiation of fine layers of multifunctional nanostructured materials
02/2005 – 01/2006	Research Associate, Institute of Polymer Materials, University of the Basque Country, San Sebastian, Spain. Topic: High Performance Dispersed Polymers
10/2003 – 02/2005	Research Assistent, University Stefan cel Mare, Suceava, Romania. Teaching activities in physical chemistry, inorganically and analytical chemistry.

Fellowships

12/2006 – 10/2010	Marie Curie Fellow, Physics of New Materials Department, Physics Institute, University of Rostock, Rostock, Germany.
02/2006 – 12/2010	Spanish National Research Council (CSIC) Fellow, Institute of Materials Science of Barcelona (ICMAB-CSIC), Autonomous University of Barcelona, (UAB), Barcelona, Spain.
02/2005 – 01/2006	Marie Curie Fellow, Institute of Polymer Materials (POLYMAT), University of the Basque Country, Barcelona, Spain.

Other activities

10/2009 – 01/2010	Lectured students practicum on Thin films.
10/2010 – 01/2011	Lectured weekly seminars on Nanotechnologies in the Material Synthesis.

Acknowledgments

First of all, I would like to express my gratitude to Prof. Eberhard Burkel for giving me the opportunity to work in his group. He gave me both freedom and support and I thank him for teaching me what is worthwhile. I am grateful that he always had time when urgent problems had to be solved.

I thank Prof. Christoph Schick for all the discussions on calorimetry and his interest in my research. Moreover, I thank him for the opportunity to collaborate with him on calorimetric studies on the composites, for providing the polyethylene samples used in this work and for his comments and wisdom during the preparation of this Dissertation.

I thank Dr. Radu Nicula for guiding me at the beginning of my research as a graduate student. Radu introduced me to the world of quasicrystals, explained me a lot about synchrotron radiation and provided me with the direction a needed at the beginning and the advice I sought at the end of this project.

I am very thankful for the unconditional friendship and invaluable help of Dr. Manuela Stir. She had the patience to help me with all administrative stuff when I first arrived to Rostock and stood beside me for many experiments. She helped me with the Peakfit calculations and was always quick to respond to emails with helpful advice.

Experiments on beamline F2.1, BW5 and B2 would have not been possible without the dedication of talented staff scientists. I thank Dr. Christian Lathe, Dr. Jozef Bednarcik, Dr. Martin von Zimmermann and Dr. Christian Knapp for sharing their time and resources with me.

Very special thanks to Karina Porath with whom I shared not only the office but also anxieties and happy moments and whom I miss. She was such a great support on carrying out the last synchrotron experiments on the time of my pregnancy and I feel blessed to have her as a friend.

I thank Daniel Schick for quickly becoming an expert on microwave heating after joining our group. His passion for physics is contagious and many of the ideas in this Dissertation originated during the time when Daniel wrote his diploma thesis in Rostock. I also thank Matthias Lütgens for his dedication to science and for being such a reliable source of inspiration in the short time we shared an office.

I am genuinely thankful to all my former colleagues in the group of Physics of new materials for creating a pleasant working atmosphere. I would like to thank: Dr. Faming Zhang, Gunnar Rott, Eileen Otterstein, Sebastian Helm, Peter Sänger, Kerstin Witte, Dr. Wiktor Bodnar, Qingqing Xu, Yujie Quan, Wenwei Gu. I thank Ulrike Schröder for her help with the administrative work, Bärbel Przybill and Stephan Flor for technical support. I would also like to thank Rico Schnierer for performing the last nano- and microindentation tests and Silvia Berndt for conducting the ICP-OES measurements. I acknowledge Dr. Margo Lantow who carried out the biocompatibility tests and I thank her for being an active collaborator.

I am grateful to Prof. Klaus-Peter Schmitz for his encouragement to finish my thesis after I started working in his group. I would specially like to thank Dr. Wolfram Schmidt and Dr. Volkmar Senz for all their help along the way. Volkmar has relentlessness for problem solving that I appreciate, and I thank him for so many helpful advices and ideas. I thank Ulli Bayer for good talks and for sharing his wisdom so graciously.

I would like to take the opportunity to thank all my current colleagues for being such great individuals and work companions. Thank you Daniela, for being so patient with my questions and problems. I particularly want to thank Ingo, Janine, Katharina, Caro, Sebastian, Lena, Jörn, Kerstin, Anja, Christoph, Stefan, Dalibor, for sharing daily lunches and cheering me up.

Thank mom and dad for your support and love. Thank Letitia and Gabi for your help on the time I was finalizing this thesis. My family, David and Dan, you are the best, thank you for putting up with me. This work would have not been possible without your patience and understanding.

I acknowledge the European Union funded Marie Curie EST fellowship for allowing me to carry out this research.

Erklärung

Ich versichere hiermit an Eides statt, dass ich die vorliegende Arbeit selbstständig angefertigt und ohne fremde Hilfe verfasst habe, keine außer den von mir angegebenen Hilfsmitteln und Quellen dazu verwendet habe und die den benutzten Werken inhaltlich und wörtlich entnommenen Stellen als solche kenntlich gemacht habe.

Rostock,

Carmen Mihoc